Developing an Aerosol Layer Height Retrieval Algorithm for Passive Space-Based Sensors

Nanda, S.

DOI
10.4233/uuid:5b842771-afc6-4ccb-91d3-bf0c3afac06b

Publication date
2022

Document Version
Final published version

Citation (APA)
Nanda, S. (2022). *Developing an Aerosol Layer Height Retrieval Algorithm for Passive Space-Based Sensors*. [Dissertation (TU Delft), Delft University of Technology]. https://doi.org/10.4233/uuid:5b842771-afc6-4ccb-91d3-bf0c3afac06b

Developing an Aerosol Layer Height Retrieval Algorithm for Passive Space-Based Sensors

Dissertation

for the purpose of obtaining the degree of doctor
at Delft University of Technology,
by the authority of the Rector Magnificus prof.dr.ir. T.H.J.J. van der Hagen,
Chair of the Board of Doctorates,
to be defended publicly on Tuesday, 6 September, 2022 at 15:00 o'clock

by

Swadhin Nanda

Master of Science Applied Earth Science,
Delft University of Technology, The Netherlands,
born in Doranda, Ranchi, India.

This dissertation has been approved by the promotors

Composition of the doctoral committee:

Rector Magnificus	chairperson
Prof. dr. Pieternel Levelt	NCAR/Delft University of Technology, promotor
Dr. Pepijn Veefkind	KNMI/Delft University of Technology, co-promotor
Dr. Martin de Graaf	KNMI, co-promotor

Composition of the independent committee:

Prof. dr.ir. Ramon Hanssen	Delft University of Technology
Prof. dr. Pier Siebesma	Delft University of Technology
Prof. dr. Gerrit de Leeuw	KNMI
Dr. Daphne Stam	Delft University of Technology

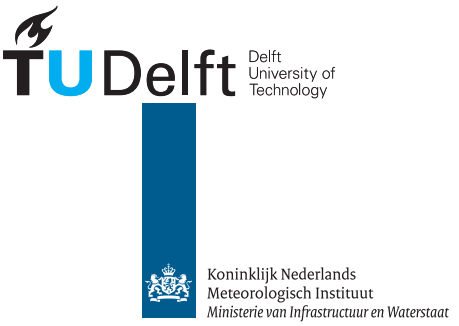

Keywords: aerosol, Earth observation, retrieval, neural networks

Printed by: Ipskamp Printing

Front & Back: Artist: Benjamin Buitenhuis. Commissioned by: Swadhin Nanda

Look at the resplendent colours on the soap bubbles!
Why is the sea blue?
What makes diamond glitter!
What makes Hubli So Special?
Ask the right questions, and nature will open the doors to her secrets.

CV Raman.

Contents

List of Figures

Summary

Aerosols are the source of the largest uncertainties in our climate models, blurring our outlook of the future. This has been attributed to the complexity of measuring their properties, which vary over time and space. Atmospheric circulation spreads aerosols across the globe from a point source, which makes satellite-based observations lucrative. At present, there are several aerosol observing missions that deliver aerosol data products in a consistent and operational manner; these missions report several aerosol properties that are important for reducing the contribution of uncertainties to our climate models. What is missing, however, is an operational data product that measures the height of these aerosols at a global scale.

Earlier attempts at this use data derived from lidar instruments in space; an example being the Cloud-Aerosol Lidar with Orthogonal Polarisation (CALIOP) instrument, which uses lasers to measure atmospheric composition. In the case of aerosols, the amount of backscattered electromagnetic radiation at each atmospheric layer gives an idea of the amount and height of aerosols. The mobility afforded by space-based instruments gives space lidars a leg up over ground-based lidars. However, the coverage of such lidar instruments is merely near-global. This has to do with the fact that while lidars in space can circle the entire globe, their footprint on the ground is very narrow, in the order of several hundred meters to a few kilometers: this is an inherent limitation of the measurement principle. Consequently, a specific patch on Earth is revisited in periods that can range several days.

An alternative to space based atmospheric lidars are space based spectral imagers. These are essentially cameras that take snapshots of the Earth, capturing the light and splitting its different electromagnetic frequencies into the scale of nanometers using very precise prisms and detection techniques. The advantage of these instruments over lidars is that they have a very large footprint, covering several thousand kilometers of area in a single fly-by. This allows for daily to even sub-daily coverage of the Earth, as each snapshot covers larger and sometimes overlapping areas. The challenge is to estimate aerosol height using spectral signatures of the Earth's atmosphere in an operational environment that can handle data coming in from the satellite at a rate of several million pixels every few minutes. This dissertation focuses on delivering the aerosol height data product operationally using computer algorithms.

The logic of aerosol height estimation using these so-called spectral snapshots of the atmosphere differ from that using lidars; the instrument does not provide data for different atmospheric layers. This has to be inferred using the chemistry of the oxygen molecule. O_2, the second most abundant gas in our atmosphere, has a unique spectral signature in the near-infrared region, comprising of electromagnetic radiation around 765 nm. The chemical structure of the oxygen molecule allows it to absorb some of these radiations, creating a structure of absorption bands. This spectral signature deepens as more light is absorbed by the oxygen: this happens as photons penetrate deeper and deeper into the

earth's atmosphere, unless they hit a barrier. If the photons bounce back from an aerosol layer at a very high altitude, the amount of absorption by oxygen would be low. This 'depth' of absorption gives clues on how high an aerosol layer might be present.

Computer models can reconstruct this oxygen absorption structure onto a simulated spectrum. One of the control parameters within the model is the height of an aerosol layer. The generated spectral signature of a simulated atmosphere resembling the atmosphere of a pixel in the snapshot from space-based hyperspectral imagers is then compared to the measured spectral signature. This usually results in a non-zero difference, which is caused by errors in the model. These errors can be minimised by using computer algorithms and mathematical information retrieval techniques, resulting in a modeled atmosphere closer to the measurement by changing the height of the aerosol layer, resulting in an aerosol height estimate. In this dissertation, computer algorithms inspired from mathematical models of brain neural networks as well as information retrieval techniques such as least squares are used.

Before the start of this dissertation, this algorithm had proven to successfully retrieve aerosol heights from older satellite instruments and was eventually adopted to a newer, more advanced satellite instrument such as the Tropospheric Monitoring Instrument (TROPOMI) on board the Sentinel-5 Precursor mission by the Dutch Space Office (NSO) and the European Space Agency (ESA). There were a few key learnings from this, 1. retrieving aerosol height over bright surfaces was challenging as the surface signature was eclipsing any aerosol signature in the spectral snapshots of the Earth's atmosphere, and 2. the algorithm was too slow and could only cover a few single-digit percentages of the total snapshots made by the space-based imager. Consequently, there were no reliable estimates over bright surfaces, and a loss of data due to a computationally demanding aerosol height retrieval algorithm.

The first paper published in the progress of this dissertation (Chapter 2), tries to theorise the reasons behind why retrieving aerosol heights from spectral snapshots in the oxygen A-band resulted in large estimation errors by the algorithm, resulting in estimates of the height of the aerosol layer that are biased closer to the surface than to the physical aerosol layer itself. To that extent, the chapter analyses the influence of photons scattered back by the surface on the spectral signature of the oxygen A-band itself. Two contributors to the spectral signature were defined, namely the atmospheric path contribution (no surface) and the surface contribution (difference between the total spectrum and the atmospheric path contribution), which both contain clues to the height of the aerosol layer. The study reveals that as the surface contribution increases, the amount of aerosol information available in the measured reflectance decreases at different parts of the spectrum. The information retrieval technique used in this algorithm uses the instrument signal to noise ratio (SNR) as a weighting function to the measured spectral signature of the atmosphere. The parts of the spectrum that were given a higher weight coincided with parts of the spectrum with less information on aerosol height.

An alternative weighting approach, called dynamic scaling, has been proposed in Chapter 3. This method non-linearly scales the instrument signal to noise ratio such that parts of the spectral signature with lower aerosol information content were given a lower weight in the aerosol height retrieval. This method was demonstrated with satellite data from hyperspectral snapshots over the 2010 Moscow wildfires over Siberia and the

2017 Iberian Peninsula wildfires over Central and Western Europe, using the GOME-2A satellite instrument. The retrieved aerosol layer heights using this so-called dynamic scaling approach resulted in slightly better aerosol layer height estimates over the formal non-scaling approach. The retrieved aerosol optical thicknesses were also systematically lower in comparison to the formal approach, although the retrieved values were still too high for the spectral regime. The method works, but will need to provide vastly more convincing performance improvements for it to be adopted beyond the test environment.

The algorithm's slow nature is a product of the complexity of the model used to synthesize these spectral signatures of the atmosphere. The model requires several thousand calculations for these simulated spectra, which required the aerosol height algorithm several minutes (in the order of 6-10 minutes) for a single pixel. There are several million pixels in a single snapshot, which meant that the algorithm required a speed boost of several orders of magnitude. To achieve this, machine learning algorithms were used to model these complex computations into a mathematical model of artificial neural networks. These efforts are documented in Chapter 4. The new neural network model boosted the aerosol height algorithm by several orders of magnitude: the older method required 184 seconds on average per pixel to compute aerosol layer heights, whereas the neural network method only took 0.167 seconds on average per pixel. Such a boost in computational speed now makes the near-realtime retrieval of aerosol layer heights feasible, i.e. the aerosol layer height products can be provided within three hours of the satellite measuring the atmosphere's spectral signature. The neural network approach was applied to real data of the December 2017 Californian wildfires as measured by TROPOMI. The retrieved aerosol layer height estimates from the neural network approach generally differed from the slower line-by-line approach by 100 m or less, with outliers to approximately 500 m. This was deemed acceptable as a first iteration to improve the operational feasibility of the aerosol layer height retrieval algorithm.

A larger validation effort was undertaken in Chapter 5. The trained neural network models were uploaded onto the TROPOMI operational data processor for the Sentinel-5 Precursor mission and has been live since 2018, delivering near-realtime estimates of aerosol layer height on a global scale. The operationally retrieved aerosol layer height product was compared with aerosol heights computed from co-located CALIOP lidar profiles across the globe. Two sets of analyses were conducted: one looking at the entire globe as a whole and the other looking at individually selected cases around the Saharan desert. This is because cloud screening can be an issue and a visual inspection can help understand the influence of un-screened clouds in the retrieval dataset. We report that TROPOMI's neural network aerosol layer height retrieval algorithm retrieves values that compare well with CALIOP weighted extinction heights. For more than 1 million co-locations between CALIOP and TROPOMI over the ocean, the TROPOMI ALH differs from CALIOP aerosol extinction heights by approximately 1km on average and 0.76km median, with the TROPOMI ALH values being lower than the CALIOP aerosol extinction heights. Over land, the same values are 2.41km on average and 1.75km as the median — it is unclear how much improvement the above mentioned dynamic scaling method could bring to these numbers over land. For the selected cases lying largely over the ocean, the averaged retrieved ALH from TROPOMI differed from CALIOP derived aerosol heights by 0.53km.

The efforts from this dissertation have led to the first ever operational aerosol height

data product that provides a global near-realtime data stream. This is the first milestone for this product. It is now up to the next generation of the aerosol height retrieval working group to improve upon this processor and deliver better and consistently more accurate aerosol height estimates.

Samenvatting

Aërosolen vormen de grootste onzekerheid in onze klimaatmodellen en daardoor uiteindelijk ook voor onze toekomst. Verder spelen ze een belangrijke rol in de luchtvervuiling. Aërosolen, ook wel fijn stof genoemd, zijn kleine deeltjes in de aardatmosfeer ter grootte van 0.01μm tot 100 μm. Aërosolen zijn zeer divers van karakter. Enkele voorbeelden van aërosolen zijn roetdeeltjes, rookdeeltjes ten gevolge van verbrandingsprocessen zoals bosbranden, vulkaanas, aërosolen die vrijkomen bij industriële processen en verkeer, en bijvoorbeeld kleine deeltjes die zich in de lucht boven zee bevinden, ook wel maritiem aërosol genoemd. Aërosolen veranderen vaak van samenstelling en grootte. Aërosolen vormen een grote onzekerheid in klimaatmodellen omdat ze erg lastig is te meten zijn, en omdat ze van heel diverse en ook altijd veranderde aard zijn. Door de wind verspreiden aërosolen zich over de wereld, dit maakt het doen van satelliet-observaties lucratief. Op dit moment zijn er verschillende satellietmissie 's die aërosolen kunnen waarnemen, hierbij wordt wel de hoeveelheid aërosol consequent gemeten, maar niet de hoogte van de aërosolen . Het laatste is belangrijk om de impact van aërosolen op het klimaat beter te kunnen bepalen, daar de hoogte van de aërosolen onder andere bepaalt hoe groot het effect van de aërosolen is op de opwarming van de aarde.

De eerste satellietinstrumenten die werden gebouwd om de hoogte van aërosolen te kunnen meten maakte gebruik van lasers. met deze instrumenten kan heel nauwkeurig de hoogte van aërosolen worden gemeten, maar door de smalle laserbundel beslaan ze niet het totale oppervlakte van de aarde. Hierdoor wordt een bepaald gedeelte van de aarde maar eens in de zo veel dagen gemeten. Een alternatief voor de bovengenoemde laser is een hyperspectrale camera, ook wel een spectrometer genoemd. Met een spectrometer wordt licht van verschillende kleuren uiteen gerafeld en apart gemeten. De satelliet spectrometers maken zo kleurenfoto's (snapshots) van de aarde. Zonlicht dat wordt gereflecteerd en verstrooid aan het aardoppervlak, wolken en aërosolen, en geabsorbeerd door bepaalde gassen in de atmosfeer, wordt door de spectrometer per kleur licht gemeten. Het voordeel van het gebruik van de spectrometer is dat je een groot deel van het aardoppervlak in een keer kan bekijken. Dit betekent dat ieder gedeelte van de aarde dagelijks, of zelfs meerdere malen per dag bekeken kan worden. **De uitdaging hierbij is om de hoogte van de aërosolen goed in te schatten met minimaal de snelheid waarmee de informatie binnenkomt**. Het hoofd thema van deze thesis is dan ook het ontwikkelen op het gebruik van algoritmes, die snel en nauwkeurig de hoogte van **aërosolen** kunnen bepalen.

Het gebruik van spectrometers voor het bepalen van de hoogte van aërosolen zijn gebaseerd op hele andere natuurkundige principes dan die gelden voor het gebruik van lasers. Een spectrometer meet het zonlicht dat door de atmosfeer wordt verstrooid en geabsorbeerd en geeft daarmee een duidelijk beeld van de samenstelling van de atmosfeer, bestaande uit wolken, aërosolen, zuurstof, stikstof en andere gassen. In dit onderzoek wordt gebruik gemaakt van zuurstof. Zuurstof heeft unieke eigenschappen, zuurstof absorbeert namelijk licht van een bepaalde specifieke kleur. Hoe dieper het zonlicht in de atmosfeer

doordringt, hoe meer licht er wordt geabsorbeerd. Tenzij het een reflecterend oppervlak tegenkomt, zoalseen laag aërosolen of wolken. De mate van absorptie van het licht wordt bepaald door hoeveel lucht het zonlicht heengaat en geeft daarmee informatie omtrent de hoogte van de aërosolen. Hoe minder licht er wordt geabsorbeerd totdat er een reflecterend oppervlak , zoals een aërosol laag, wordt gemeten, des te hoger de aërosolen zich in de atmosfeer bevinden en vice-versa.

Door computermodellen kan de lichtabsorptie door zuurstof worden nagebootst. In dit proefschrift werken we met een dergelijk computermodel. Eén van de speerpunten binnen dit model is de hoogte van de aërosolen. Het doel hierbij is om de hoogte van de aërsolen te bepalen en indien nodig te veranderen, zodat de simulatie uiteindelijk zo goed mogelijk overeenkomt met de meting van de satelliet spectrometer. Hoe dichter de simulatie bij de werkelijke meting komt, hoe beter onze veronderstelling van de hoogte van de aërosolen.

Bovengenoemde methode is eerder succesvol getest. Dit gebeurde met oudere satelliet spectrometers. Uiteindelijk werd deze methode ook gehanteerd in de nieuwere satelliet-spectrometers, genaamd OMI en TROPOMI, die gebruikt zijn in dit proefschrift. **Deze satellietinstrumenten zijn ontwikkeld in opdracht van het Nederlandse Ruimtevaart Agentschap (NSO) en respectievelijk in 2004 en 2017 gelanceerd** . Door het gebruik van deze nieuwe reken methode gebruikmakend van de nieuwe instrumenten, zijn er diverse ontdekkingen gedaan. Een belangrijke ontdekking is dat de verwachte hoogte van de aërosolen boven land niet klopte. De verwachtingen met betrekking tot de aërosolen boven zee was daarentegen beter. Daarnaast kon worden geconcludeerd dat de huidige methode niet snel genoeg was voor de nieuwe satellieten, omdat deze satellieten significant meer data produceren.

Het eerste gedeelte van dit proefschrift legt uit waarom bovengenoemde methode over land minder effectief is. Er werd ontdekt dat land in de eerdergenoemde methode te 'licht' was. Dit betekende dat de beelden weinig contrast opleverden. Hierdoor konden aërosolen en land niet gescheiden worden gezien. Om het onderscheid tussen aërosolen en land beter te kunnen maken, is er een nieuwe methode ontwikkeld. Hoewel deze nieuwe methode succesvol is gebleken, moet de methode vanuit statistisch oogpunt nog wel veel vaker worden toegepast, om zo te leiden tot onbetwiste en overtuigende resultaten. Deze resultaten kunnen enkel worden behaald als de nieuwe methode wordt blootgesteld aan een grotere hoeveelheid data.

In het tweede gedeelte draait het om het ontwikkelen van een snellere methode. Dit om de nieuwe, snellere en grote hoeveelheid satellietdata te ondersteunen. Dit werd behaald door een ander soort computeralgoritmes te ontwikkelen, gebaseerd op neurale netwerken, oftewel zelflerende systemen. **Deze algoritmes zijn speciaal gericht op het informatie halen uit een grote hoeveelheid data, vergelijkbaar met hoe een brein data opslaat en interpreteert**. De resultaten hiervan waren verbluffend; ten eerste is de nieuwe methode duizend(!) keer sneller dan de oude methode. Daarnaast behoudt de nieuwe methode, ondanks het feit dat dit vele malen sneller gaat, de precisie van de oude methode.

Het proefschrift heeft het volgende opgeleverd; het is het eerste dataproduct omtrent de hoogte van aërosolen dat het hele aardoppervlak omvat waarbij er gebruik wordt gemaakt van een verbeterde, geadvanceerde methode gebaseerd op zelflerende algoritmes. Het is aan de nieuwe generatie wetenschappers om deze methode nog verder te verbeteren.

1

Introduction

This thesis focuses on atmospheric aerosol particles. To understand the role of aerosols for air quality and climate, let's discuss the atmosphere in general. With each passing epoch, developed and developing countries are more aware of their role in our changing Earth. The development and growth of technology has afforded many of us an incomparable standard of living but at costs to all of us; we are collectively affecting the air we breathe, the temperature of the Earth's atmosphere and oceans, the amount of DNA-damaging solar radiation reaching us, the oceans creeping up the sea shores, the frequency of tropical thunderstorms, the hail raining down on a hot summer evening, droughts, floods, and a host more of phenomena that affect our quality of life. Slowly but surely, every policy maker's decision is being weighted by its impact on our Earth's climate and air quality — which of our actions is unsustainable for our home planet? How much time do we have before it is too late? Answering these questions begins with observing our planet and understanding the influence of a changing Earth on our future.

To understand the impact of mankind on planet Earth, we start with the atmosphere. The atmosphere is a layer of gases extending from the Earth's surface to approximately a 100 kilometers into space, trapped by the gravitational pull of the Earth. Of the atmosphere, all of life on Earth lives either below the Earth's surface (including oceans) or within 0-10 km in the first layer of the atmosphere - the troposphere; our 'living quarters' is merely 0.15% of the Earth's radius. What is even more awe-inspiring is the composition of the Earth's atmosphere - the air we breathe is mostly Nitrogen and Oxygen, with only 1% being other gases, which include greenhouse gases essential for our survival. A part of this 1% of the aforementioned 0.15% is responsible for trapping heat and warming our Earth. The study of our future, hence, involves precise measurements and study of our influence on a tiny part of the whole of the planet.

The study of the physics and chemistry of the Earth's atmosphere involves the Sun and the Earth. On the macroscopic scale, incoming solar radiation gets absorbed by the atmosphere, which emits longwave radiation to heat up the atmosphere; these components are integral to the Earth's radiation budget. On the microscopic scale, incoming solar radiation interacts with several reactive molecules in the atmosphere, leading to a cresendo of physical and chemical phenomena that shape our Earth's atmosphere. One such example

of reactive molecular species are greenhouse gases (of which, CO_2 is the most famous), which are efficient at capturing heat from the Sun and warm the atmosphere. Without greenhouse gases, the Earth would be inhospitable for life to evolve. The warming of Earth's surface and oceans results in convective motion of air and atmospheric turbulence, leading to the formation of clouds, which are probably the most important driver of the Earth's fertility. The presence of clouds results in a redistribution of solar energy in many different ways. In order to understand the atmosphere, one must understand clouds as well.

Generally speaking, depending on the height and geometrical thickness, clouds have the ability to warm (in the case of high clouds), cool (in the case of low clouds) the atmosphere, or have absolutely no affect to the radiation budget of the Earth's atmosphere. With increasing human contribution to global warming, the future of clouds is uncertain: we are unsure whether clouds will evolve to either accelerate the global warming process or slow it down. Understanding clouds will require an understanding of their genesis and evolution, without which we are ill-equipped to accurately predict the future of our place on Earth.

Clouds are a product of very complex atmospheric physics and chemistry. Essentially, clouds on Earth comprise of water vapor condensed around so-called cloud condensation nuclei (CCN). These condensation nuclei are non-gaseous, hydrophilic and very small particles floating in the atmosphere. These CCN particles are typically atmospheric aerosols, which either originate from the Earth's surface as primary aerosols, or are produced in the atmosphere from chemical reactions (called secondary aerosols). These aerosols are either naturally produced through naturally occurring forest fires (Figure 1.1), volcanic eruptions (Figure 1.2), dust from desert storms (Figure 1.4), marine sea salt sprayed by the ocean and so on, or through anthropogenic activities such as smoke from factories, crop burning (Figure 1.3), emissions from vehicles, and so on. Provided that humidity is constant, an atmosphere containing an abundance of tiny aerosol particles will result in more but smaller cloud droplets, as there are more aerosols acting as cloud condensation nuclei. This will change the Earth's radiation budget from the perspective of clouds interacting with solar radiation. A simple example of this phenomenon is the formation of clouds with smaller droplet sizes along shipping lines over the ocean (see Figure 1.5). While (through clouds) aerosols have an indirect impact on the Earth's radiation budget, they also have their own direct effects as well. Aerosols scatter and absorb shortwave radiation, thus affecting the amount of solar radiation reaching the Earth's surface. Local heating by absorption by aerosols can also have an affect on the atmospheric stability. Also, the interaction between aerosols and cloud layers will depend on whether the aerosols are above, below or within clouds. The combined direct and indirect effects of aerosols on the climate are considered among the largest sources of uncertainty in our knowledge of the Earth's radiation balance.

Figure 1.1: Australian wildfires on November 15th, 2019, as captured by NASA's MODIS Aqua satellite instrument. Image derived from Euronews.

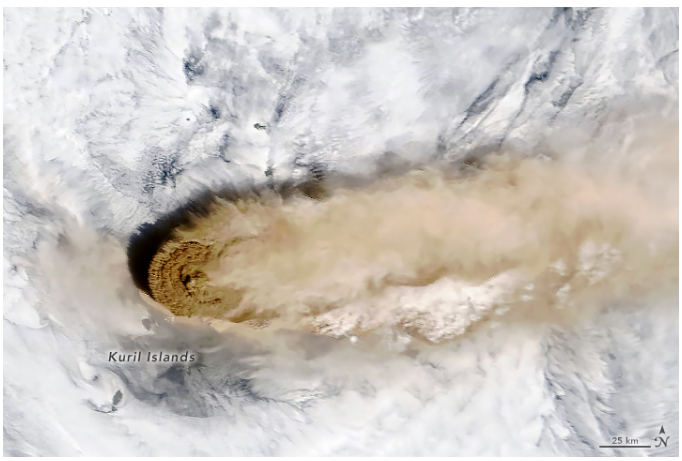

Figure 1.2: Eruption of the Raikoke Volcano on 22nd June, 2019, as captured by NASA's Terra satellite. Image derived from NASA.

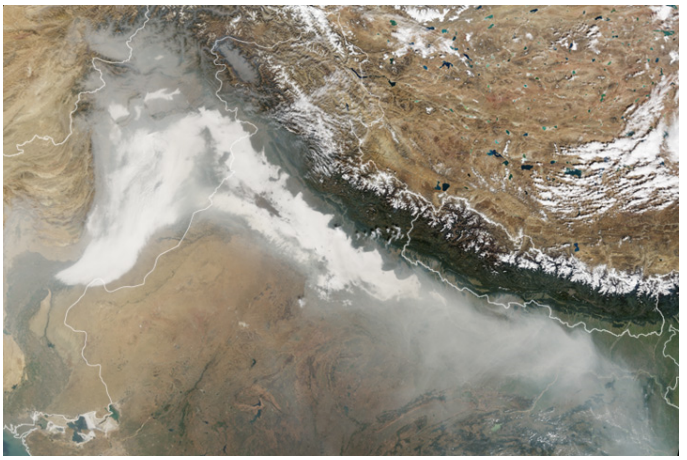

Figure 1.3: Crop burning aerosols blanketing India on a winter day on November 7th, 2017, as captured by NASA's MODIS Terra and Aqua instruments. Image derived from NASA.

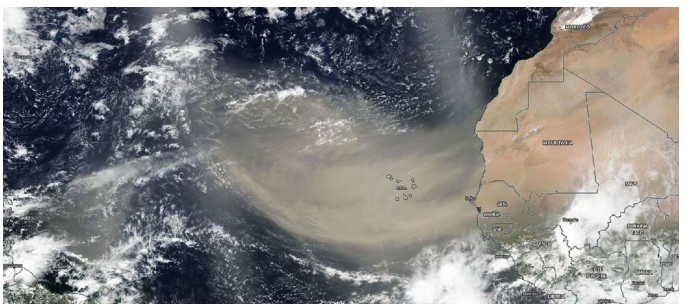

Figure 1.4: Desert dust aerosols from the Sahara transported over the Atlantic Ocean on 18th June, 2020, as captured by NASA-NOAA's Suomi NPP satellite. Image derived from NASA.

In the context of understanding their impact on the radiation budget, various properties of aerosol particles are studied in order to characterize them into different categories, such as their shape, size, origin and their ability to interact with radiation. By studying these particles, aerosols can be modeled into describable mathematical representations. These are aerosol models, which are a part of a more comprehensive model used to describe the Earth's atmosphere and its interaction with solar radiation. Once the interaction of aerosol and other species with radiation in the atmosphere has been modeled, the atmospheric radiation is modeled using radiative transfer models (RTM). Depending on the objective of the RTM, it provides the net radiation after all interactions at a specific atmospheric level — for instance, computing the net radiation from the Sun on the surface after accounting for different components of the atmosphere, or the same at the top of atmosphere after accounting for all radiative interactions that the incoming solar radiation participates in as it traverses through various atmospheric layers of Earth and back to outer space. Aerosols are studied on a macroscopic level using observations of incoming and outgoing solar radiation from the Earth using space-based instruments, using RTMs to derive aerosol properties from the measurements. Such techniques are a part of a bigger scientific field known as remote sensing.

1.1 Aerosols

Research into aerosols began as early as the 19^{th} century, following the interest in the scientific communities into cloud formation. So far, aerosols are defined as a colloidal suspension of particles, solid (ash, smoke, dust) or liquid (mist and fog), in the atmosphere. Aerosols are either produced by emissions from the Earth's surface carried up higher into the atmosphere by winds, or through gas-solid transition of reactive chemical species in optimal conditions (moisture, energy and so on). The various physical and chemical processes responsible for their creation result in diversity of aerosol properties. Several classifications are used to characterise aerosols, for example based on composition (organic or inorganic), size, origin, and their intensive and extensive properties (discussed further in this section). Aerosol particles have a diameter typically between 0.01 μm - 100 μm, and are classified into fine or coarse aerosols (depending on their size). Fine aerosols are primarily produced in the atmosphere through reactive gaseous species, whereas coarse aerosol are directly emitted as particles.

Based on their origin, aerosols are classified into two categories — primary and secondary. Primary aerosols are a result of direct emission of aerosol particles from the Earth. These emissions can be natural or anthropogenic. For instance, black carbon aerosols emitted from forest fires, ash clouds from volcanic eruption, desert dust aerosols, marine sea spray aerosols are some examples of natural emissions of aerosols. Some of these natural emissions are essential for the fertility of the Earth — for instance, the Bodele depression in the Southern Saharan desert is the origin of approximately 40 million tonnes of mineral matter to South America in a year, which fertilizes the Amazon rainforest [10]. Anthropogenic aerosols, on the other hand, are emitted from human activities. Examples of such are unburnt hydrocarbons from transport vehicles, coal-fired power plants and shipping (as shown in Figure 1.5).

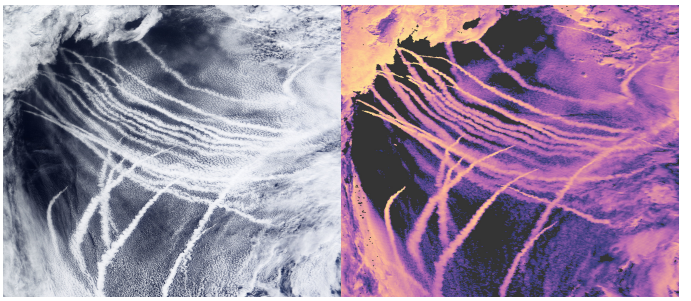

Figure 1.5: **Left**: NASA MODIS image over Northeast Pacific Ocean on March 4, 2009. The streaks in the image represent clouds formed by shipping emissions. **Right**: Cloud droplet size colored from brightest to darkest representing smaller droplets to larger droplets. Image derived from NASA.

In contrast to primary aerosols, secondary aerosols are produced in the atmosphere through chemical processes between reactive gaseous species, leading to gas-solid transitions. Consider volcanic eruptions that produce volcanic ash clouds and eject aerosols and SO_2 vertically in the atmosphere. The SO_2 in the volcanic ash plume reacts with water vapor to produce sulphate aerosol particles. A similar but anthropogenic example is the emission of unburnt hydrocarbons (black carbon aerosols), NOx and SO_2 from incomplete combustion of sulphur and nitrogen containing fossil fuels, which are converted to sulphate and nitrate aerosols via chemical reactions with water vapor, oxygen and ammonia.

Aerosol scatter and absorb shortwave radiation, leading to either warming or cooling of the planet. Before discussing the ability of aerosols to alter the radiation budget of the Earth, let's look at the ability of aerosols to scattering or absorb light in the context of modeling the transfer of radiation between several layers in the atmosphere.

Scattering and absorption of light by aerosols

Scattering of incident light by aerosols is determined by the size of the aerosol particle relative to the wavelength of the radiation. Before delving into the relationship between size and scattering type, we have to first understand the many different categories of scattering.

Depending on the type of interaction of light between incident electromagnetic radiation and the scattering component, there can be different forms of scattering. If the incident electromagnetic wave does not undergo a change in its frequency after scattering, it is considered to be elastic scattering. If the wavelength of the radiation changes, it is a form of inelastic scattering. In the context of modeling scattering in a terrestrial atmosphere, it is common practice to assume that most of scattering is elastic with a few exceptions. This is because elastic scattering dominates over inelastic scattering, and the inclusion of inelastic scattering in a model significantly increases the complexity, requiring more computations that slow down data processors relying on the RTM. Algorithm developers generally look at the downsides of excluding inelastic scattering in the RTM, by comparing the RTM's output including or excluding inelastic scattering. If the model output without inelastic scattering is sufficiently close to the same that includes it, inelastic scattering can be generally ignored.

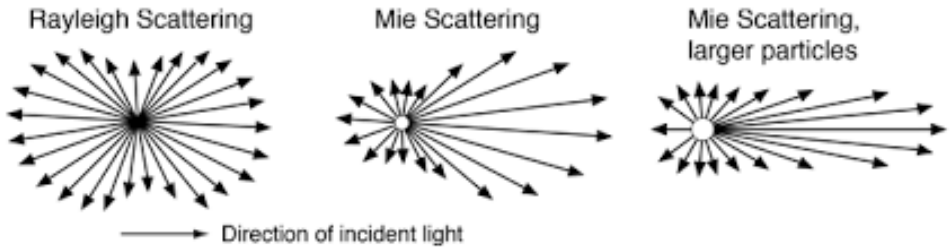

Figure 1.6: A graphical representation of scattering for Rayleigh and Mie scattering types. Rayleigh scattering is generally isotropic, whereas Mie scattering is more directional. Image derived from the http://hyperphysics.phy-astr.gsu.edu/hbase/atmos/blusky.htmlGeorgia State University website.

If the particle size is much smaller than the incident wavelength, the predominant scattering is Rayleigh scattering. Rayleigh scattering dictates that the intensity of light scattered by particles is inversely proportional to the fourth power of the incident wavelength, i.e. the lower the wavelength the higher the intensity of Rayleigh-scattered light. This is the reason why the sky during the day appears blue instead of red, as blue light has a shorter wavelength than red and is hence more scattered than the red component of light. As the particle size increases and becomes more comparable to or larger than the incident wavelength, scattering becomes more directional and dependent on the angle of incident light (Figure 1.6). In such cases, there are a few models that are better equipped to describe the directionality of scattering. One commonly used model is Mie scattering, which applies for spherical particels. To compute the scattering properties using the Mie scattering model, detailed knowledge on the particle size distribution and refractive index is required. In the context of atmospheric remote sensing, however, this information is usually the unknown. As an alternative to Mie scattering, simpler models, that do not require as much information on aerosol properties, can be used to approximate the scattering properties of aerosols. One such model is the Henyey-Greenstein model [9], which has a single parameter that determines the directionality of scattering. The governing model parameter in the Henyey-Greenstein function is called the anisotropy factor g, and is used to compute $p(\theta)$ as follows,

$$p(\theta) = \frac{1}{4\pi} \frac{1 - g^2}{(1 + g^2 - 2g\cos(\theta))^{3/2}}. \tag{1.1}$$

An additional advantage of the Henyey-Greenstein model is that it is computationally more efficient than Mie scattering in RTMs.

The ability of aerosols to scatter or absorb radiation is described by the single scattering albedo. The aerosol single scattering albedo (ω) is a wavelength-dependent unitless parameter calculated as the ratio of aerosol light scattering to extinction of light by aerosols. If the extinction of incident electromagnetic radiation on a particle is purely due to scattering, that particle will have a single scattering albedo of 1. Likewise, if the same extinction is due to absorption only, the particle will have a single scattering albedo of 0. Aerosol single scattering albedo is largely dependent on the aerosol chemical composition and microphysical properties. Within the atmosphere, the single scattering albedo of aerosols varies in the range between 0.6 and 1.0. The strongest absorbing aerosols are produced by

biomass burning, although the single scattering albedo can vary strongly depending on the material that is burned as well as on the burning process. The single scattering albedo also varies with wavelength. For example Saharan dust particles will absorb much stronger in the UV as compared to the visible and near-infrared [4]. The light that is absorbed by aerosol particles will be released as longwave radiation. This raises the temperature of the atmospheric layer these absorbing aerosol species occupy, thus changing atmospheric stability. Due to these scattering and absorption properties, aerosols are important for the radiation budget of the Earth. This mechanism is discussed in the following.

Interaction with radiation

Incoming solar shortwave radiation travels through the atmosphere and reaches the surface. Some of this incoming radiation is reflected back to space by bright reflectors such as clouds, ice sheets and deserts. Some of the shortwave light, however, interacts with atmospheric species and dark surfaces, warming up the Earth's land, ocean and the atmosphere. Once warmed up, these various parts of our Earth's atmosphere and surface reflect back longwave radiation outwards, which may be re-absorbed in the atmosphere by several reactive species of which aerosols are a part. The role of aerosols in altering the radiation budget has a significant impact on the Earth's climate.

Solar radiation entering the Earth's atmosphere is either reflected back to space, or absorbed. Reflection back to space is a result of scattering by clouds, aerosol particles and molecules, and reflection by the surface. Gas molecules, aerosol particles and the surface can also absorb wave radiation. The absorbed shortwave radiation is emitted as longwave radiation. Some of the longwave radiation is trapped in the atmosphere, for example by greenhouse gases, clouds and aerosol particles. However, the total energy of the incoming shortwave radiation is (almost) equal to the sum of the outgoing shortwave and longwave radiation, which is referred to as the Earth's radiation balance. Aerosols have significant contributions to scattering and absorption of especially shortwave radiation, and they therefore impact the Earth's climate.

A commonly discussed example to demonstrate the impact of aerosols on the Earth's climate is the eruption of Mt. Pinatubo in June 15, 1991, Philippines. Considered as the largest eruption in 100 years, the Mt. Pinatubo incident resulted in the injection of sulphur dioxide gas and ash clouds https://pubs.usgs.gov/fs/1997/fs113-97/up to 35 km, well into the stratosphere. Unlike the troposphere, the stratosphere does not have a precipitation mechanism to bring aerosols back to the surface. Consequently, the sulfate aerosols that formed from the emitted sulphur dioxide stayed in the stratosphere for up to 15 months. The sulfate aerosols in the stratosphere scatter part of the incoming solar shortwave radiation back to space, which in the case of Mt. Pinatubo resulted a tropospheric cooling, reducing the average global temperature by about 0.5 degree Celsius between 1991 to 1993. Absorbing aerosols such as black carbon have the opposite effect when compared to volcanic sulfate clouds. Absorbing aerosols emit longwave radiation that warms up the atmospheric layers they populate. If present above clouds, black carbon aerosols reduce the efficiency at which clouds reflect back solar radiation. The effect of black carbon aerosols is not limited to within the atmosphere — if deposited over ice sheets, black carbon aerosols reduce snow albedo, increase absorption on incoming shortwave radiation and directly contribute to global warming and ice sheet surface melting [5].

In the Pinatubo eruption example, aerosols caused a net cooling of the surface due to the aerosol direct radiative effect, which involves blocking shortwave solar radiation from the Earth's surface. Depending on their ability to absorb or scatter radiation, aerosols directly affect the radiation budget by absorbing solar radiation (causing warming of the atmospheric layer they occupy) or scattering back incoming solar radiation (cooling the Earth's surface and the atmosphere). All of these effects result in a net cooling of the Earth's surface and warming of the atmospheric layers. This warming of the atmospheric layers has a direct impact on the convective available potential energy, potentially causing in a reduction in atmospheric dynamics [12].

Indirectly, aerosols alter the radiation budget via clouds. As previously mentioned, aerosols directly affect the formation of clouds and precipitation on Earth. Depending on the type of aerosol particle acting as the CCN and its amount, aerosols alter the radiative properties of clouds. For a given amount of water vapor present in the atmosphere, cloud droplet size reduces with an increase in aerosol concentration. Clouds with a smaller droplet size, due to a large CCN concentration, have a larger cloud optical depth due to increase in the number concentration of cloud droplets. This increase in cloud optical depth increases multiple scattering within the cloud layer, thereby increasing the cloud albedo. An increase of cloud albedo reflects back more of the incoming shortwave radiation being, resulting in a cooling effect. Such a phenomena is called the Twomey effect, named after Sean Twomey who first theorised it in 1974 [19].

The presence of aerosols can alter cloud lifetimes due to an increase in CCN and subsequent decrease in cloud droplet size; smaller cloud droplets will take longer to coalesce into larger ones, thereby delaying precipitation and increasing cloud lifetime. If embedded into the cloud layer, absorbing aerosols can contribute to the evaporation of the cloud by heating up the layer they are present at, and at the same time cause an increase in the radiative forcing, resulting in warming [8, 11] (see Figure 1.7).

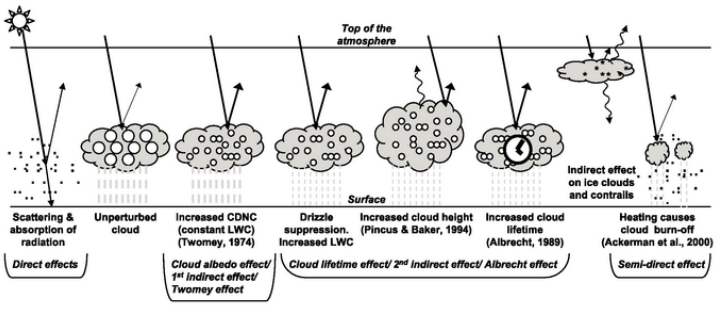

Figure 1.7: The effect of aerosols and clouds on incoming solar radiation. The figure has been derived from IPCC 2007, modified from Haywood and Boucher [6].

1.2 Vertical distribution of aerosols in the Earth's atmosphere

A key factor in the effects that aerosols have in the atmosphere, is the vertical distribution of absorbing or scattering aerosols; understanding various processes such as aerosol radiative effects, cloud dynamics and so on depend on the atmospheric layers where aerosols are present. These are briefly discussed in this section.

1.2.1 The role of aerosol vertical distribution on atmospheric processes

Depending on the single scattering albedo of aerosols, the aerosol direct radiative effect can be strongly dependent on the vertical distribution of the aerosols; as aerosols become more absorbing (such as black carbon aerosols), their direct radiative effects increase [7, 13]. Assuming a cloudless atmosphere, the knowledge of the vertical distribution of aerosols is a key input parameter for climate models.

An aerosol layer sitatuated either above or below a cloud layer can also alter the radiative forcing of the cloud. Podgorny and Ramanathan [14] used a radiation model based on microphysical, chemical, optical and lidar data collected over the Indian ocean to model the effect on cloud radiative forcing where aerosols were present directly above or below clouds. They observed an aerosol-free cloudy atmospheric forcing is approximately 7.0 Wm^{-2}, which changed to 7.5 Wm^{-2} when aerosols with optical thickness at 500 nm of 0.4 and aerosol single scattering albedo at 500 nm of 0.9 were introduced below the clouds. When aerosols were introduced above the clouds, this number changed to almost 10.0 Wm^{-2}. Studies by Choi and Chung [2], Samset et al. [15] report similar observations.

In the context of cloud-aerosol semi-direct effects, Allen et al. [1] have observed that models that simulate a uniform aerosol vertical profile, i.e. aerosols are uniformly distributed throughout the entire atmospheric column, lead to negatively biased estimates of semi-direct effects. Studying the effect of aerosols on atmospheric radiative forcing will benefit from knowledge on aerosol vertical distribution.

Observing the long-range transport of aerosols goes beyond the study of aerosol radiative forcing. Volcanic eruptions can result in large sulphate aerosols and ash clouds, which are hazardous to air transport. A good reference for this is the eruption of the Icelandic volcano Eyjafjallajökull in 2010, which resulted in the mass closure of airports, resulting in stranded passengers in all of Europe. Biomass burning aerosols are similarly hazardous when it comes to aviation safety as well. For these reasons, observing the vertical distribution of aerosols is key.

Finally, remote sensing observations benefit from redundancy. Aerosol vertical distribution observed from multiple remote sensing methods and missions will result in a much better knowledge of the parameter. In this context, scientific products do not necessarily compete: they add value to each other. This is why more operational products from different missions and methods will result in a better understanding of the impact of aerosols on Earth.

1.2.2 Observing aerosol vertical distribution

In the context of aerosol remote sensing, instruments can generally be classified into ground-based observations, airborne and space-based observations. All three strategies have their own merits and shortcomings, which is why observations from all three sources are relevant for weather and climate studies. For instance, ground-based measurement units can take observations of aerosols at very short intervals of time, but they are fixed at one location. A mitigation of their limited spatial coverage can be a network of ground stations, such as the AERONET (Aerosol Robotic Network) which is a Sun and sky radiometer specific for aerosol observations. However, such networks have limitations on their own; because these networks have several 'moving parts' (physically and organisationally), their management becomes a challenge on its own. The radiosonde, an instrument fixed to a weather balloon, takes precise measurements at various points in the atmospheric column. However, radiosondes do not have a large spatial coverage and require re-deployment for more temporal coverage. Aircraft-borne instruments improve upon the spatial coverage limitations of radiosondes and ground-based instruments significantly, and provide information on intrinsic properties of aerosols for remote sensing applications. If the goal is to monitor aerosols globally, spaceborne instruments on board a satellite mission are unparalleled. Satellite instruments have been growing in their popularity, which has led to unprecedented improvements in their spatial resolution and temporal coverage. Satellite instruments, combined with ground based monitoring networks and airborne instrument observations, are the best step forward to observe aerosols.

Satellite and ground based remote sensing instruments exploit the property of aerosols to interact with incident radiation in order to derive aerosol parameters. Depending on the source of incident radiation, remote sensing can be of two kinds — active and passive. Active instruments have their own source of electromagnetic radiation which is directed at the aerosols. The interactions between the emitted radiation and aerosol particles result in some of the signal returning back (also known as backscatter), which is then received by a receiver typically present on the instrument itself. An example is the lidar (Light Detection And Ranging), which measures the distance of the aerosol particles by using the time delay of the return signal. This time delay, along with detailed information about the instruments positioning in space or on the ground relative to the Earth, provide sufficient information to calculate the vertical height of the aerosol particles in a layer relative to the ground. An example of a satellite lidar is the CALIOP (Cloud Aerosol Lidar with Orthogonal Polarisation) instrument [20], which emits a very focused laser beam aimed directly downwards (nadir). This beam penetrates the atmosphere, resulting in a backscatter signal in the presence of interacting atmospheric species such as aerosols and clouds, and (if not fully attenuated) reaches the Earth's surface before reflecting back. Lidars can be ground-based as well; an example of a network of lidars is the EARLINET (European Aerosol Research Lidar Network), which consists of several powerful lidars pointed towards the sky spread out all over Europe. An alternative to ground-based lidars are ceilometers, which are essentially low-power lidars capable of penetrating only a short distance into the atmosphere. An example of an operational ceilometer network is maintained by the EUMETNET (European Meteorological Network), whose data has been used in this dissertation as well.

Lidars are an excellent tool for looking at the entire atmospheric column, as they have

the potential to measure multiple atmospheric layers with the same lidar beam. There is one caveat, however; while satellite lidars are space-based, their narrow beam limits their spatial coverage severely. Satellite lidars have to do several passes before they can revisit a previously sensed location; considering that aerosols vary significantly over time due to atmospheric circulation and other physical and chemical processes, satellite lidars give a detailed snapshot at a very low temporal resolution. Ground-based lidars have a very high temporal resolution but do not cover the entire globe. For these reasons, lot of research is currently being done in order to derive information on aerosol vertical distribution from passive space-based instruments. Passive sensors cover a large area in a single scan by measuring the backscattered solar radiation at the top of the atmosphere after its interaction with scattering and absorbing species in the Earth's atmosphere. This enables them to revisit a specific point on Earth daily in the case of polar orbiting satellites, or hourly in the case of geostationary satellites. An example of a passive instrument inferring aerosol vertical information is TROPOMI (TROPOspheric Monitoring Instrument) on board the Sentinel-5 Precursor mission by the European Space Agency (ESA), which revisits every part of the Globe at least once each day. In the future, the geostationary Sentinel-4 mission from ESA will provide hourly coverage of Europe and parts of North Africa, with instruments capable of measuring aerosol vertical information.

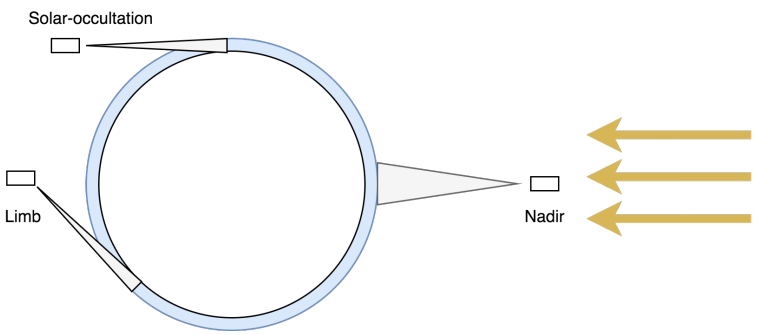

Figure 1.8: A schematic of different kinds of atmospheric remote sensing techniques. The yellow arrows represent shortwave radiation from the Sun.

In the context of aerosol remote sensing, there are two kinds of passive sensors classified on the configuration of their viewing geometry — nadir viewing which involves looking straight downwards and horizontal viewing instruments such as limb sounding instruments that look horizontally and solar occultation instruments which look horizontally towards the Sun. Each of them have their advantages and disadvantages, with horizontal viewing instruments having a better vertical profiling ability but only up until the upper troposphere whereas the nadir viewing instrument views the entire atmospheric column with limited profiling ability. The subject of this dissertation is the nadir-viewing satellite instrument for deriving aerosol vertical information. This is discussed in the following section.

1.3 Forward modeling and inverse methods - techniques used to infer aerosol properties from remote sensing observations

Coupled with physical models describing the interaction of photons with the Earth's atmosphere, remote sensing observations of the Earth's atmosphere can be exploited to retrieve knowledge on aerosol properties at a particular scene being observed by the instrument. For instance, physical models compute reflectance at the top of the atmosphere, which is the ratio of the incoming solar irradiance into the atmosphere and outgoing Earth radiance at the top of the atmosphere. With knowledge on the satellite instrument's response function, these models compute how a satellite would measure reflectance.

To retrieve aerosol vertical information, passive sensors exploit wavelength regions where photons are absorbed by oxygen. Oxygen has unique light absorbing properties at different wavelength regions, for instance in the near-infrared region of the electromagnetic spectrum between 758 nm and 770 nm (see Figure 1.9), also known as the oxygen A-band. In this region, absorption is described by photon-induced magnetic dipole transition between $b^1\Sigma_g^+ \leftarrow X^3\Sigma_g^-(0,0)$ electric potential levels of molecular oxygen, and collision-induced absorption between O_2-O_2 and O_2-N_2. The amount of absorption by oxygen at a specific wavelength gives an indication of the photon path length through the atmosphere; if absorption by oxygen at that wavelength is low, it suggests that the photon has not travelled deep into the atmosphere before getting scattered back by a scattering layer in the atmosphere, whereas higher oxygen absorption at the same wavelength suggests that the photon travelled deeper into the atmosphere unobstructed (resulting in more interaction with oxygen). Radiative transfer models exploit this interaction of photons with oxygen and a scattering layer to infer the height at which the layer is present. These models calculate the amount of light at the top of Earth's atmosphere given a certain atmosphere containing scattering and absorbing species. The simulated top of atmosphere reflectance, coupled with measurements from satellite sensors make up the key ingredients for an aerosol height retrieval algorithm.

The retrieval of aerosol vertical information is an inverse problem that involves two kinds of calculations (see Figure 1.10 for a diagrammatic representation of inverse problems). First, a set of calculations compute with assumed aerosol properties the top of atmosphere reflectance (**R**). These calculations are done by a model called the forward model (f), which in the case of aerosol vertical information x is the radiative transfer model with certain fixed parameters **b**,

$$\mathbf{R} = f(\mathbf{x}, \mathbf{b}). \tag{1.2}$$

The simulated top of atmosphere reflectances are then fed into an inverse method which retrieves aerosol parameters that best match the observed top of atmosphere reflectances. The deciding parameters here is the cost function χ^2, which gives an idea of how far the guess of the aerosol properties is from what is measured by the satellite instrument **y**. In the context of atmospheric retrievals, the cost function is a mathematical derivation of an optimisation parameter, the most common being the mean squared error between the modelled and real observations,

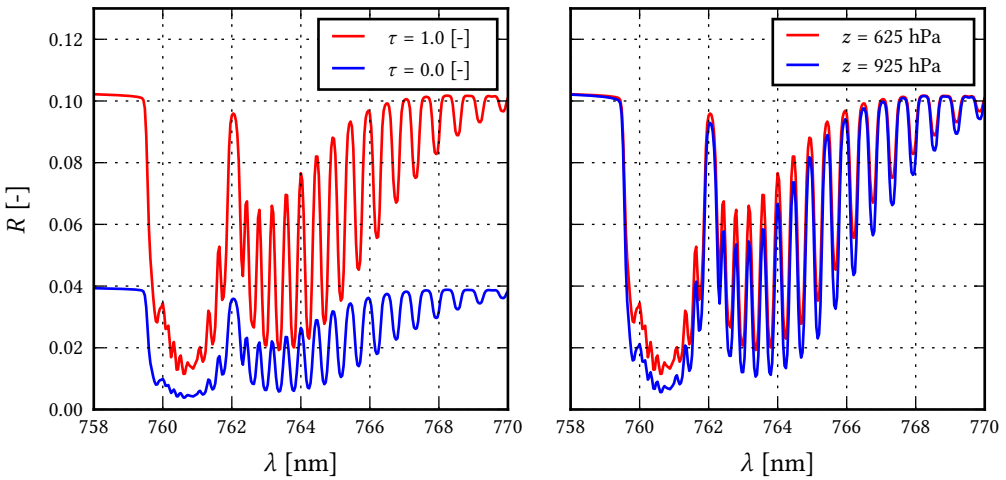

Figure 1.9: Synthetic oxygen A-band spectra for a cloudless atmosphere containing aerosols over a surface with an albedo of 0.03, as measured by a nadir pointing instrument for a solar zenith angle at 45°. The instrument settings are that of the UVN instrument. Aerosol single scattering albedo is fixed at 0.95 and scattering by aerosols is described by a Henyey-Greenstein phase function with an asymmetry factor (g) of 0.7. **Left**: Aerosol layer is fixed at a height of 900 hPa - 950 hPa, for two scenes are different aerosol optical thicknesses. **Right**: Aerosol vertical distribution is varied for an aerosol optical thickness of 1.0 at 760 nm.

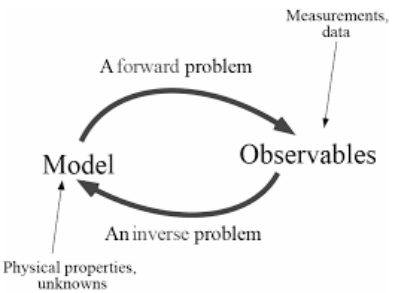

Figure 1.10: Diagrammatic representation of information retrieval from observations using a forward model and inverse method. Image derived from `http://web.gps.caltech.edu/classes/ge193.old/lectures/Lecture1.pdf`.

$$\chi^2 = [\mathbf{y} - \mathbf{F}(\mathbf{x}, \mathbf{b})]^T [\mathbf{y} - \mathbf{F}(\mathbf{x}, \mathbf{b})]. \tag{1.3}$$

If the measurement error $\mathbf{S}_\epsilon$ is known, it can be incorporated into the inverse method, thereby transforming the cost function to

$$\chi^2 = [\mathbf{y} - \mathbf{F}(\mathbf{x}, \mathbf{b})]^T \mathbf{S}_\epsilon^- 1 [\mathbf{y} - \mathbf{F}(\mathbf{x}, \mathbf{b})]. \tag{1.4}$$

The cost function is minimised iteratively. The retrieval is said to have converged to a final solution when the state vector does not change beyond a certain threshold; if the state vector does not change from iteration to iteration, the cost function cannot be minimised further. In the context of development of scientific methods for retrieving information it is insufficient to assume the reliability of the final solution just from the minimised cost function. There could be several assumptions made by the model that are incorrect, meaning that the minimised solution is not representative of reality. There could also be flaws in the instrument, which may need calibration post-launch. Sometimes, the amount of information available in the measured spectra is simply insufficient to reliably assume that the final solution is representative of reality. Therefore, the model parameters that lead to a minimised cost function are that model's best representation of the observation.

Retrieving information in a remote sensing context is an ill-defined problem; there are many unknowns which require assumptions. For instance, as clouds are more efficient at reflecting radiation than aerosols, their presence in the measured scene is known to result in errors in the retrieved aerosol property. Because of this, it is very important to incorporate validation of the retrieved solution as an important step in the development of a retrieval algorithm. Because of the ill-defined nature of the retrieval problem, there are several challenges associated with the retrieval of aerosol information. These are highlighted in the following section.

1.4 Challenges in retrieving aerosol layer height from satellite measurements of the oxygen A-band reflectances

Assuming a thick aerosol layer over a very dark surface, the largest contribution to the top of atmosphere reflectance is scattering from this single aerosol layer. Since the majority of the signal occurs due to aerosols, the retrieval algorithm usually does not face any challenge in retrieving the height of this aerosol layer. These cases are, in reality, the best case scenario. The typical scene for retrieving aerosols can contain multiple aerosol layers over a bright reflecting surface with the possibility of clouds either over or under the aerosol layer. As aerosols are weak scatterers compared to clouds or bright surfaces such as desert, the majority of the signal in the top of atmosphere reflectance in these cases is not from aerosols; retrieving aerosols is now a needle in the haystack problem. The four major challenges in retrieving aerosol vertical information from the oxygen A-band are,

1. **Retrieving aerosol vertical information in the presence of clouds** When it comes to retrieving aerosols in the presence of clouds from passive measurements of the spectral signature of the top of atmosphere reflectance, one approach is to

abandon retrieval attempts. The retrieval of aerosol properties suffers in the presence of clouds; if the retrieval algorithm manages to meet the criteria described for a final solution, the retrieved aerosol layer height does not necessarily represent the true aerosol layer height. In these cases, if the cloud is situated over the aerosol layer, the retrieved aerosol layer height is usually higher than the true aerosol layer height. If clouds are situated below the aerosol layer, the retrieved aerosol layer height is lower than the true aerosol layer height. There is a clear cloud signature in the oxygen A-band, if at all clouds are present in the scene. In fact, the presence of aerosols results in errors in the retrieved cloud product as well. This is a clear sign that the retrieval algorithms for extracting vertical information from the oxygen A-band are actually attempting to characterise the height at which most of the scattering in the atmosphere takes place. As a result of this, aerosol layer height retrieval algorithms must employ strict cloud filtering in order to remove any cloud contamination in the final aerosol product.

2. **The influence of bright surfaces on aerosol vertical information retrieval** The issue of optically brighter objects diminishing aerosol signal in the TOA reflectance extends to cases where, even over a cloudless scene, a bright surface can result in an incorrect aerosol layer height estimate. Consequently, aerosol information content from measured spectra in the oxygen A-band reduces with increasing surface brightness [3, 17]. This is intuitive; generally appearing optically thinner over bright surfaces, aerosol layers allow photons from the top of atmosphere to pass through and interact with the surface. These interactions result in scattering between the aerosol layer and the surface, thereby increasing the photon path length through the atmosphere. A longer photon path length results in a larger number of instances of interactions between photons and molecular oxygen, resulting in more absorption in the oxygen A-band. Since aerosol heights are inferred from oxygen absorption, a longer photon path length implies more absorption which further implies a lower aerosol layer. This has been observed in literature; Sanders et al. [16] report their retrievals of aerosol layer height to be biased closer to the surface over land. There remains a requirement on the scattering aerosol layer in the atmosphere to be brighter than the surface in one way or the other for the retrieved aerosol layer height to be closer to the aerosol layer than the surface itself. This makes retrievals over deserts, snow and ice very challenging. Within the oxygen A-band, vegetation appears bright as the spectral band lies outside the photosynthetically active spectrum where plants absorb Sunlight (see Figure 1.11). This spectral range is known as the Photosynthetically Active Radiation (PAR), beyond which plants do not absorb Sunlight and rather reflect it. The edge of the PAR towards the longer wavelength side is known as the red-edge, beyond which densely vegetated land has the potential to appear brighter than the desert when observed from space. This is due to the unique cell structure of the leaves that allows for very efficient scattering of light [18]. Consequently, retrievals of aerosols over vegetated land are also error-prone.

3. **Computational effort of line-by-line radiative transfer models in the context of aerosol vertical information retrieval** In the case of retrieving the vertical information on weak scattering species such as aerosols, radiative transfer

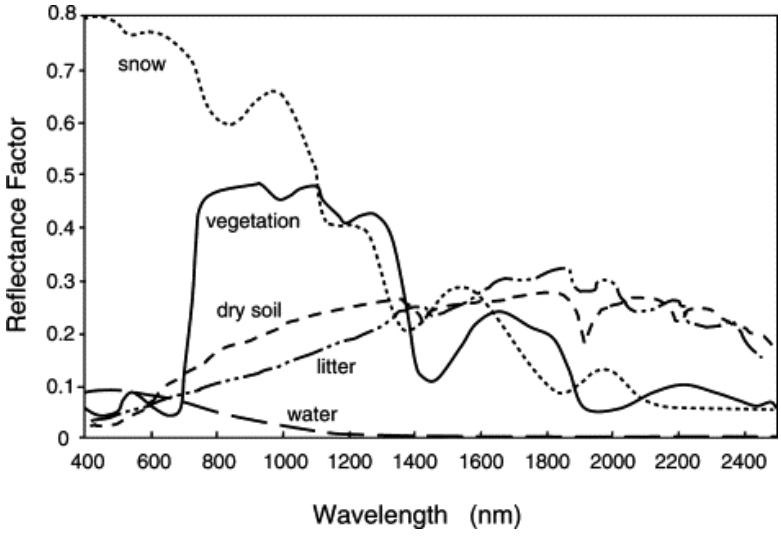

Figure 1.11: Surface reflectance factor as a function of spectral wavelength for different surface types. Image derived from https://www.sciencedirect.com/topics/earth-and-planetary-sciences/spectral-reflectanceSciencedirect.

calculations need to be very accurate as small errors in the reflectance can lead to large errors in the retrieved aerosol layer height. This is especially the case around oxygen absorption lines present within the oxygen A-band, as the vertical information of aerosols is inferred from these absorption lines by the retrieval method. There are a large number of absorption lines in the oxygen A-band, which equates to a large number of calculations. Because each calculation involves the accounting of scattering and absorption in the entire atmospheric column, the computational requirements are very steep. In an iterative estimation process, each step is thus time consuming. If the retrieval algorithm needs several steps to converge to a final solution, a compromised computational speed can severely limit the applicability of the retrieval technique, especially in an operational environment that needs to deliver near-realtime data with limited resources within a limited time frame. This limitation puts a demand on the improvement of the computational speed of the radiative transfer model calculations itself.

4. **Limited aerosol information content in the oxygen A-band** The oxygen A-band has limited amount of information on the various aerosol properties. Because of this, a lot of assumptions and simplifications have to be made in order to retrieve aerosol layer height. From our experience the oxygen A-band can be used to retrieve the height of a single aerosol layer with a certain geometric thickness, whereas the atmosphere contains aerosols at several atmospheric layers, either separated into separate layers or combined into a single layer with thicknesses that vary from hundreds of meters to kilometers. What then does the retrieved aerosol layer height really mean? According to [16], the aerosol layer height from the oxygen A-band should be considered as an effective scattering height more so than an geometric aerosol layer height. If the single aerosol layer in a cloudless scene over a dark

surface is uniform, the effective scattering height aligns with the geometric height; this is important to note as we proceed into this dissertation.

1.5 Research objectives

From the challenges discussed so far, this dissertation identifies two primary topics for research in the context of retrieving aerosol layer height from satellite measurements of the top of atmosphere Earth radiance in the oxygen A-band.

1. **Understanding the influence of reflected radiation from the surface on the retrieved aerosol layer height**. The goal of understanding the influence of surface on aerosol height retrievals is significant, as we are interested in observing fire smoke, volcanic ash, dust events and anthropogenic aerosols that affect human settlements. Understanding this can help in developing methods to limit the influence of surface albedo on aerosol layer height retrievals. To that extent, this dissertation
    - expands upon error sources in the retrieved aerosol layer height product for retrievals over bright surfaces, and
    - proposes an alternative method to minimise the influence of the surface in aerosol layer height retrievals over bright surface albedo scenes.
2. **Speeding up the retrieval algorithm**. The number of computations for retrieving aerosol layer height for a single ground pixel is extremely high, which must be limited significantly to improve the effectiveness of the retrieval algorithm in an operational environment. To tackle this problem, this thesis
    - discusses a strategy that exploits artificial neural networks to reduce the number of computations required by the forward model, and
    - compares the neural network algorithm by comparing aerosol layer height retrievals with the same from an active instrument.

1.6 Outline of this thesis

Chapter 2 discusses the sources of error associated with a retrieved aerosol layer height product, followed by a possible strategy of ameliorating some of these errors in chapter 3. Chapter 4 discusses the machine learning inspired radiative transfer modeling approach in order to improve the computational speed of the retrievals. Chapter 5 validates the neural network aerosol layer height retrieval algorithm using colocated aerosol height retrievals from active space-based instruments. Finally, the dissertation concludes with chapter 6.

References

[1] Allen, R. J., Amiri-Farahani, A., Lamarque, J.-F., Smith, C., Shindell, D., Hassan, T., and Chung, C. E. (2019). Observationally constrained aerosol–cloud semi-direct effects. *npj Climate and Atmospheric Science*, 2(1):1–12.

[2] Choi, J.-O. and Chung, C. E. (2014). Sensitivity of aerosol direct radiative forcing to aerosol vertical profile. *Tellus B: Chemical and Physical Meteorology*, 66(1):24376.

[3] Corradini, S. and Cervino, M. (2006). Aerosol extinction coefficient profile retrieval in the oxygen A-band considering multiple scattering atmosphere. Test case: SCIAMACHY nadir simulated measurements. *Journal of Quantitative Spectroscopy and Radiative Transfer*, 97(3):354–380.

[4] Dubovik, O., Holben, B., Eck, T. F., Smirnov, A., Kaufman, Y. J., King, M. D., Tanré, D., and Slutsker, I. (2002). Variability of Absorption and Optical Properties of Key Aerosol Types Observed in Worldwide Locations. *Journal of the Atmospheric Sciences*, 59(3):590–608.

[5] Hadley, O. L. and Kirchstetter, T. W. (2012). Black-carbon reduction of snow albedo. *Nature Climate Change*, 2(6):437–440.

[6] Haywood, J. and Boucher, O. (2000). Estimates of the direct and indirect radiative forcing due to tropospheric aerosols: A review. *Reviews of Geophysics*, 38(4):513–543.

[7] Haywood, J. M. and Ramaswamy, V. (1998). Global sensitivity studies of the direct radiative forcing due to anthropogenic sulfate and black carbon aerosols. *Journal of Geophysical Research: Atmospheres*, 103(D6):6043–6058.

[8] Haywood, J. M. and Shine, K. P. (1997). Multi-spectral calculations of the direct radiative forcing of tropospheric sulphate and soot aerosols using a column model. *Quarterly Journal of the Royal Meteorological Society*, 123(543):1907–1930.

[9] Henyey, L. C. and Greenstein, J. L. (1941). Diffuse radiation in the Galaxy. *The Astrophysical Journal*, 93:70.

[10] Koren, I., Kaufman, Y. J., Washington, R., Todd, M. C., Rudich, Y., Martins, J. V., and Rosenfeld, D. (2006). The Bodélé depression: a single spot in the Sahara that provides most of the mineral dust to the Amazon forest. *Environmental Research Letters*, 1(1):014005.

[11] Liao, H. and Seinfeld, J. H. (1998). Effect of clouds on direct aerosol radiative forcing of climate. *Journal of Geophysical Research: Atmospheres*, 103(D4):3781–3788.

[12] Mallet, M., Tulet, P., Serça, D., Solmon, F., Dubovik, O., Pelon, J., Pont, V., and Thouron, O. (2009). Impact of dust aerosols on the radiative budget, surface heat fluxes, heating rate profiles and convective activity over West Africa during March 2006. *Atmospheric Chemistry and Physics*, 9(18):7143–7160.

[13] Meloni, D., di Sarra, A., Di Iorio, T., and Fiocco, G. (2005). Influence of the vertical profile of Saharan dust on the visible direct radiative forcing. *Journal of Quantitative Spectroscopy and Radiative Transfer*, 93(4):397–413.

[14] Podgorny, I. A. and Ramanathan, V. (2001). A modeling study of the direct effect of aerosols over the tropical Indian Ocean. *Journal of Geophysical Research: Atmospheres*, 106(D20):24097–24105.

[15] Samset, B. H., Myhre, G., Schulz, M., Balkanski, Y., Bauer, S., Berntsen, T. K., Bian, H., Bellouin, N., Diehl, T., Easter, R. C., Ghan, S. J., Iversen, T., Kinne, S., Kirkevåg, A., Lamarque, J.-F., Lin, G., Liu, X., Penner, J. E., Seland, , Skeie, R. B., Stier, P., Takemura, T., Tsigaridis, K., and Zhang, K. (2013). Black carbon vertical profiles strongly affect its radiative forcing uncertainty. *Atmospheric Chemistry and Physics*, 13(5):2423–2434.

[16] Sanders, A. F. J., de Haan, J. F., Sneep, M., Apituley, A., Stammes, P., Vieitez, M. O., Tilstra, L. G., Tuinder, O. N. E., Koning, C. E., and Veefkind, J. P. (2015). Evaluation of the operational Aerosol Layer Height retrieval algorithm for Sentinel-5 Precursor: application to Oxygen A band observations from GOME-2A. *Atmospheric Measurement Techniques*, 8(11):4947–4977.

[17] Sanghavi, S., Martonchik, J. V., Landgraf, J., and Platt, U. (2012). Retrieval of the optical depth and vertical distribution of particulate scatterers in the atmosphere using O_2 A- and B-band SCIAMACHY observations over Kanpur: a case study. *Atmospheric Measurement Techniques*, 5(5):1099–1119.

[18] Seager, S., Turner, E., Schafer, J., and Ford, E. (2005). Vegetation's Red Edge: A Possible Spectroscopic Biosignature of Extraterrestrial Plants. *Astrobiology*, 5(3):372–390.

[19] Twomey, S. (1974). Pollution and the planetary albedo. *Atmospheric Environment (1967)*, 8(12):1251–1256.

[20] Winker, D. M., Vaughan, M. A., Omar, A., Hu, Y., Powell, K. A., Liu, Z., Hunt, W. H., and Young, S. A. (2009). Overview of the CALIPSO Mission and CALIOP Data Processing Algorithms. *Journal of Atmospheric and Oceanic Technology*, 26(11):2310–2323.

2

A study on errors associated with O_2 A-band aerosol retrievals over bright surfaces

Decades of research into aerosol information in the oxygen A-band has proven its feasibility in retrieving aerosol layer height from satellite measurements of the top-of-atmosphere reflectances. In the context of a theoretical application of understood principles, it is fairly simple to retrieve aerosol layer height: simulate a top-of-atmosphere reflectance spectrum for a scene with known parameterisations and retrieve while assuming ALH to be unknown. Practically, this is a pipe dream: the true parameterisations are never known to a retrieval algorithm. Luckily, significant assumptions in several parameters of the atmosphere makes retrieving aerosol information from the oxygen A-band possible, but with an important caveat. In this case, the largest source of error arises from incorrect knowledge of the surface reflectance. Interestingly, if the surface albedo is very low (a dark surface such as the ocean), incorrect assumptions in other parameterisations such as aerosol properties and so on do not influence the biases in the retrieved aerosol layer height too much. However, if the surface albedo is large, a pandora's box of errors influence the final retrieved product. This chapter discusses this interesting quagmire of retrieving aerosol properties from measured top-of-atmosphere reflectance in the oxygen A-band over optically bright surfaces in the context of the following research goal,

Expand upon error sources in the retrieved aerosol layer height product for retrievals over bright surfaces.[1]

[1]This chapter is published in `https://doi.org/10.5194/amt-11-161-2018`, 2018.

2.1 Introduction

The retrieval of aerosol properties from the oxygen A-band presents a few challenges, one of them being that aerosol layers in the atmosphere are usually optically thin, and are quite difficult to observe in the presence of clouds. This is because clouds have an optical depth which is typically orders of magnitude larger than that of aerosols, and are more efficient in scattering incoming radiation. Consequently, aerosol retrieval algorithms generally refrain from retrieving over cloudy scenes; our algorithm is no exception to this and requires cloud screening to filter out pixels containing clouds. While cloudy pixels can be filtered out to a certain degree, retrieving aerosols from measurements in the oxygen A-band over bright surfaces faces a host of other challenges. From literature, it is understood that aerosol information content from measured spectra in the oxygen A-band reduces as the surface albedo increases [2, 13]. Sanders et al. [12] report potentially large biases in their aerosol layer height retrievals from the oxygen A-band when the surface albedo is fitted. In a previous chapter, Sanders and de Haan [10] also report that certain specific combinations of geometry, aerosol, and surface properties can result in unusually large uncertainties in the retrieved aerosol layer height (see also Figure 8-2 in Sanders and de Haan [11]). Such large biases can perhaps be attributed to a phenomenon known as the critical surface albedo regime [14], wherein for specific surface albedos, the top of atmosphere reflectance becomes independent of the aerosol optical thickness. Sanders et al. [12] observe that when the surface albedo isn't fitted, typical uncertainties in the surface albedo database over land can result in large biases. From our analyses, we understand that for relative errors up to 10% in the surface albedo, retrievals over dark surfaces are not affected, whereas the same over sufficiently bright surfaces (surface albedo greater than 0.2) can suffer from very large biases.

A combination of all the error sources discussed previously can result in large biases. In fact, we observe that the presence of errors often lead to no convergence in the retrieval, with no concrete predictability on which pixel is likely to yield no result. Because of this, the operational algorithm wastes resources trying to retrieve aerosol layer height from pixels that potentially do not have any usable aerosol information. This is especially problematic in the framework of high resolution instruments, which demand operational processors to make efficient use of computational time and effort to process large number of spectra (typically several hundred per second). In order to design more efficient operational algorithms, the concept of critical surface albedo needs to be extended beyond the framework provided by Seidel and Popp [14] into the oxygen A-band for aerosol optical thickness as well as aerosol layer height.

This chapter analyses simulated measured top of atmosphere reflectance spectra in the oxygen A-band and provides an explanation for the loss of aerosol information over bright surfaces. Its implication is provided in an optimal estimation framework, specific to the retrieval of aerosol layer height, with results from sensitivity analyses. The analysis is followed up with a demonstration in a real data environment by retrieving aerosol layer height over a bright surface. The case study chosen is the retrieval of optically thick biomass burning aerosol plumes over the 2010 Russian wildfires, to demonstrate the effect of this loss of aerosol information over land. This chapter is one in a series of chapters on development of an operational oxygen A-band Aerosol Layer Height retrieval algorithm for Sentinel-4/5/5-P by KNMI, preceeded by Sanders and de Haan [10] and Sanders et al.

[12]. The current operational ALH algorithm for S5P is described in Sanders and de Haan [11]. While the results of this chapter are relevant for the Sentinel 5-Precursor algorithm as well, the instrument model used in the sensitivity studies is for the UVN spectrometer on the S4 mission.

The next section (Section 2) provides a description of the forward model and the optimal estimation framework. Section 3 discusses the concept of aerosol-surface ambiguities in the oxygen A-band. Section 4 describes various sensitivities of our retrieval algorithm focusing on the difference between dark and bright surfaces. Section 5 discusses aerosol layer height retrievals over the 2010 Russian wildfires using GOME-2A data. Section 6 concludes this chapter with a discussion and the implication of the findings from this chapter.

2.2 The forward model and the inverse method

2.2.1 Forward model

There are three primary parts of the forward model, namely the atmospheric model, the radiative transfer code, and the instrument model. A radiative transfer code is used to model a high resolution top of atmosphere radiance by propagating radiation through the atmosphere described by the atmospheric model. The top of atmosphere reflectance R computed by the forward model is defined as the ratio of the radiance I of the pixel measured by the instrument to the top of atmosphere solar irradiance E_0 of the pixel on a horizontal surface unit,

$$R(\lambda) = \frac{\pi I(\lambda)}{\mu_0 E_0(\lambda)}. \tag{2.1}$$

μ_0 represents the cosine of the solar zenith angle of the pixel, and λ represents the wavelength.

The top of atmosphere reflectance is calculated after the measured radiance and irradiance are convolved with the Instrument Spectral Response Function (ISRF) of the hyperspectral sensor in order to simulate measured spectra by a satellite instrument. For simulations, the high resolution solar spectrum from Chance and Kurucz [1] is used.

Radiative transfer model

The radiative transfer model is the Layer Based Orders of Scattering (LABOS) method, which is a variant derived from the Doubling-Adding method [3]. Atmospheric properties are calculated line-by-line to compute the reflectance at the top of atmosphere. The radiative transfer code is a part of a software package called DISAMAR (Determining Instrument Specifications and Analysing Methods for Atmospheric Retrievals), which is the main workhorse of operational algorithm development efforts at KNMI for oxygen A-band aerosol height retrieval with S5P/S4/S5 instruments. Scattering by gases is described by Rayleigh scattering, which has a low scattering cross section in this wavelength region. Because of this, polarisation is ignored. Wavelength shifts caused by rotational Raman scattering (RRS) are ignored in order to reduce computational effort, since line by line calculations are computationally expensive in the oxygen A-band. This is convenient, since the Raman scattering cross section is even smaller than that of Rayleigh scattering. The atmosphere in the forward model is plane-parallel for the Earth radiance, and spherically corrected for the incoming solar irradiance.

Atmospheric model

For cloud-free conditions, the following four absorption and scattering processes are significant in the wavelength range between 758 nm and 770 nm: scattering by gases, reflection of light by the surface, scattering and absorption by aerosol particles, and absorption by molecular oxygen. Absorption of solar radiation by O_3 and H_2O are ignored, since they are not dominant absorbing gases in this spectral range.

The surface reflectance is assumed isotropic, described by its albedo. Depending on the surface albedo, a surface can either be bright or dark. Dark surfaces are classified with surface albedo close to 0.05 (or lower), which in the oxygen A-band spectral region typically corresponds to ocean surfaces. Bright surfaces in the oxygen A-band on the other hand have a surface albedo of 0.2 (intermediately bright) and higher and are primarily over land. For the oxygen A-band at 760 nm, typical values of surface albedo over vegetated surfaces exceed 0.4 since the wavelength band is located beyond the red edge where absorption of solar radiation by chlorophyll diminishes. Scenes with snow or ice are not processed.

Aerosols are represented as a single layer with a fixed pressure thickness of 50 hPa, containing aerosol particles with a fixed aerosol optical thickness and aerosol single scattering albedo. Aerosol layer height is defined as the mid-pressure of the aerosol layer — if the aerosol layer extends from 650 hPa to 600 hPa, the aerosol layer height is 625 hPa. In the operational S5P aerosol layer height algorithm, currently the aerosol phase function is a Henyey-Greenstein model [6] with an asymmetry factor of 0.7, and an aerosol single scattering albedo of 0.95 [12]. While a Mie scattering model could be used instead of the Henyey-Greenstein model, the latter is computationally less expensive and hence more optimal for the operational algorithm.

Oxygen absorption cross-sections are derived from the NASA JPL database, following Tran and Hartmann [17] who indicate that line parameters in the JPL database are more accurate than the HITRAN 2008 database. First-order line mixing and collision induced absorption by O_2-O_2 and O_2-N_2 are derived from Tran et al. [16] and Tran and Hartmann [17].

Instrument model

The instrument model is described by the instrument slit function, whose spectral resolution depends on its Full Width at Half Maximum (FWHM), and its noise model. For this study, oxygen A-band is simulated using specifications of the Sentinel-4 Ultraviolet Visible and Near infrared (UVN) instrument, which is set to launch in 2022. The instrument is a sounder with a hourly coverage over Europe and Northern Africa at a spatial resolution of 8 × 8 km^2 sampled at 45°N and 0°E. The instrument has a FWHM of approximately 0.116 nm, oversampled by a factor 3, effectively giving the instrument a spectral sampling interval of 0.04 nm. Aerosol layer height will be an operational product provided by the Sentinel-4 mission. An example of oxygen A-band spectra at a 0.116 nm resolution is provided in Figure 1.9. For retrievals with real data, measurements from the Global Ozone Monitoring Experiment-2 on board the MetOp-A satellite are used. Launched on October 16, 2006, GOME-2A is an optical spectrometer fed by a scanning mirror which enables across-track scanning in the nadir. The instrument has a spectral sampling interval of approximately 0.21 nm at 758 nm (spectral resolution of 0.48 nm for channel 4), and has a nominal spatial resolution of 80 × 40 km^2 [8]. A shot noise model is assumed for the instrument.

2.2.2 Inverse method

The inverse method is based on the Optimal Estimation (OE) framework described by Rodgers [9], which is a Maximum A-Posteriori (MAP) estimator that constrains the least-squares solution with a-priori knowledge on the state vector. The method assumes Gaussian statistics for the a-priori errors. The iterative method is a Gauss-Newton approach, and the estimation parameters are the aerosol optical thickness τ and the aerosol layer height z. The cost function χ^2 is defined as,

$$\chi^2 = [\mathbf{y} - \mathbf{F}(\mathbf{x},\mathbf{b})]^T \mathbf{S}_\epsilon{}^{-1} [\mathbf{y} - \mathbf{F}(\mathbf{x},\mathbf{b})] + (\mathbf{x} - \mathbf{x_a})^T \mathbf{S_a}{}^{-1} (\mathbf{x} - \mathbf{x_a}), \tag{2.2}$$

where $\mathbf{y}$ is the measured reflectance, $\mathbf{F}(\mathbf{x},\mathbf{b})$ is the vector of calculated reflectance using the forward model, $\mathbf{x}$ is the state vector containing fit parameters, $\mathbf{b}$ is the vector containing other model parameters, $\mathbf{S}_\epsilon$ is the measurement error-covariance matrix, $\mathbf{x_a}$ is the a-priori state vector, and $\mathbf{S_a}$ is the a-priori error-covariance matrix. $\mathbf{S_a}$ is diagonal, assuming no correlation between state vector elements. $\mathbf{S}_\epsilon$ is also diagonal, since the measurement error is assumed uncorrelated. $[\mathbf{y} - \mathbf{F}(\mathbf{x},\mathbf{b})]^T \mathbf{S}_\epsilon{}^{-1} [\mathbf{y} - \mathbf{F}(\mathbf{x},\mathbf{b})]$ is the measurement part of the cost function, whereas $(\mathbf{x} - \mathbf{x_a})^T \mathbf{S_a}{}^{-1} (\mathbf{x} - \mathbf{x_a})$ is the state vector part of the cost function.

The a-posteriori error covariance matrix $\hat{\mathbf{S}}$ is computed as,

$$\hat{\mathbf{S}} = (\mathbf{K}^T \mathbf{S}_\epsilon \mathbf{K} + \mathbf{S_a}{}^{-1})^{-1}, \tag{2.3}$$

where $\mathbf{K}$ is the Jacobian with its columns containing partial derivatives of the reflectance with respect to the state vector elements. DISAMAR calculates the Jacobian semi analytically, similar to the reciprocity method described by Landgraf et al. [7]. The Jacobian drives the retrieval towards the solution as an integral component in the update to the state vector,

$$\mathbf{x}_{n+1} = \mathbf{x_a} + (\mathbf{K_n}{}^T \mathbf{S}_\epsilon{}^{-1} \mathbf{K_n} + \mathbf{S_a}{}^{-1})^{-1} \mathbf{K_n}{}^T \mathbf{S}_\epsilon{}^{-1} [\mathbf{y} - \mathbf{F}(\mathbf{x_n}) + \mathbf{K_n}(\mathbf{x_n} - \mathbf{x_a})], \tag{2.4}$$

where $\mathbf{x}_{n+1}$ is the next iteration to the n^{th} iteration in the retrieval, and $\mathbf{K_n}$ is the Jacobian evaluated at the n^{th} iteration. The Jacobian can become singular if the value of the partial derivative of the reflectance to the a state vector parameter is very low, or is correlated to another parameter in the state vector. In these cases, the error covariance matrix does not exist, since the inverse covariance matrix is non-invertible; if it is *nearly* singular, the problem is ill-conditioned and may result in very large biases in the estimation.

The inverse method reaches a solution if the change in the state vector between iterations is below a convergence threshold. It is possible that during iterations, the inverse method estimates state vector elements beyond boundaries. In such a case, the state vector element is adjusted back to just within its physical limits. If the adjustment is made in two consecutive iterations, the retrieval is stopped and no solution is reached. The upper cap in the number of iterations is set at 12, beyond which the retrieval is said to have failed. In this chapter, these failed retrievals are termed as non-convergences. The next section discusses the atmospheric conditions that can potentially lead to these non-convergences.

2.3 Aerosol-surface ambiguities in the oxygen A-band

2.3.1 Influence of surface reflectance on aerosol information content in the oxygen A-band

Assuming the surface to be an isotropic reflector, the top of atmosphere reflectance over a surface with an albedo A_s can be written as the sum of atmospheric path contribution of the photon R_p and surface contribution R_s,

$$R(\lambda, A_s) = R_p(\lambda) + R_s(\lambda, A_s). \tag{2.5}$$

R_p is the top of atmosphere reflectance in the absence of a surface. R_s is calculated by subtracting the path contribution from the total top of atmosphere reflectance, and represents contributions from photons that have been reflected one or more times by the surface. R_s is dependent on the absorbing and scattering species present in the atmosphere, and also includes aerosol influences. R_p is calculated by substituting $A_s = 0.0$ and calculating the top of atmosphere reflectance in DISAMAR. R_s is calculated by subtracting R_p from R. With increasing viewing angle, R_p increases whereas R_s decreases (Figure 2.1). This is in line with expectation, since the slant aerosol optical thickness increases, which increases the amount of contribution that aerosols have in $R(\lambda, A_s)$. At steeper geometries, light at the top of atmosphere is more diffuse than direct, which is the primary reason why R_s decreases (assuming a Lambertian surface).

For a model parameter x with two values x_a and x_b, the difference spectrum $\Delta R_{\Delta x}$, defined as

$$\Delta R_{\Delta x} = R_{x_a} - R_{x_b}, \tag{2.6}$$

can reveal the influence the model parameter x has on the oxygen A-band. The spectral shape of $\Delta R_{\Delta x}$ can also show parts of the spectrum that are more sensitive to x. Following Equations 2.5 and 2.6, $\Delta R_{\Delta x}(\lambda, A_s)$ is defined as

$$\Delta R_{\Delta x}(\lambda, A_s) = \Delta R_{p_{\Delta x}}(\lambda) + \Delta R_{s_{\Delta x}}(\lambda, A_s). \tag{2.7}$$

If $\Delta R_{p_{\Delta x}}$ and $\Delta R_{s_{\Delta x}}$ have opposing signs, $\Delta R_{\Delta x}$ reduces following Equation 2.7 which results in a reduction of sensitivity to the parameter x.

Comparing $\Delta R_{p_{\Delta z}}$ and $\Delta R_{s_{\Delta z}}$ at two different aerosol layer heights (z) for two different scenes with the same atmospheric conditions (Figure 2.2, left panel), it is observed that $\Delta R_{p_{\Delta z}}$ and $\Delta R_{s_{\Delta z}}$ have opposite signs and R_p is relatively more sensitive to aerosol layer height than R_s. This is especially the case in the deepest part of the R-branch between 759.50 nm and 761.30 nm and parts of the P-branch between 761.30 nm and 763.00 nm, where the higher absorption cross section reduces the number of photons that can reach the surface. This ultimately reduces the magnitude of R_s to the top of atmosphere for these absorption sub-bands. $\Delta R_{s_{\Delta z}}$ over ocean and vegetation also shows an increase in its overall magnitude with an increase in surface albedo, and hence an increase in cancellation between $\Delta R_{p\Delta z}$ and $\Delta R_{s\Delta z}$. Figure 2.3 represents the variation of the derivative of reflectance with respect to aerosol properties, for increasing surface albedo. Albeit subtle, the consequence of this cancellation between $\Delta R_{p\Delta z}$ and $\Delta R_{s\Delta z}$ is observed in Figure 2.3 (Top), where $\partial R/\partial z$ for

the deepest part in the R-branch and parts of the P-branch diminishes gradually with an increase in surface albedo.

The same experiment is repeated for aerosol optical thickness (τ), and the results are presented in Figure 2.2 (middle panel). $\Delta R_{p_{\Delta\tau}}$ and $\Delta R_{s_{\Delta\tau}}$ are anti-correlated (Pearson correlation coefficient is -0.99, irrespective of the surface albedo), and the magnitude of $\Delta R_{s_{\Delta\tau}}$ increases with an increase in surface albedo. Figure 2.3 (Middle) shows the partial derivative of the reflectance with respect to τ for increasing surface albedo. This anti-correlation explains negative derivatives in the higher surface albedo regime.

$\Delta R_{p_{\Delta\omega}}$ and $\Delta R_{s_{\Delta\omega}}$ of aerosol single scattering albedo (ω) in Figure 2.2 (right panel) reveals a strong correlation (with a Pearson correlation coefficient of almost unity). This suggests that an increase in surface albedo increases the sensitivity of the model to ω. We suspect that this information predominantly arises from interactions between scattered light by aerosols and surface. The magnitude of the partial derivative of reflectance with respect to ω for increasing surface albedo (shown in Figure 2.3, bottom) shows an increase, which is in line with our analysis of Figure 2.2 (right panel).

For increasing surface albedo, the more dynamic parts of the $\partial R/\partial\tau$ spectrum in Figure 2.3 (Middle) correspond to spectral points with less absorption by molecular oxygen. These are also the parts of the spectrum with a high signal to noise ratio (SNR) and high S_ϵ^{-1}. From Equation 2.4, the inverse method gives a higher priority to spectral points with a higher S_ϵ^{-1}. Intuitively, low information of τ from the oxygen A-band spectrum will increase the dependency of the inverse method to prior information. This is further discussed in the next section.

2.3.2 Aerosol-surface interplay in the top of atmosphere reflectance

In the inverse method, an a-priori error of 100% is assumed for the aerosol optical thickness, which gives it freedom to vary during iterations. If the a-priori aerosol optical thickness is far from the solution, a large a-priori error ensures that the retrieval can estimate the parameter in fewer iterations. However, whether the Gauss-Newton optimisation reaches the correct solution depends on two primary factors, i. if the cost function has a global minimum, and ii. the gradient of the cost function is sufficiently large, such that it is minimised significantly at every iteration.

From our analysis of $\Delta R_{\Delta x}$ for aerosol parameters, we have identified aerosol optical thickness to be the parameter most affected by an increasing surface albedo, due to the cancellation between $\Delta R_{p_{\Delta\tau}}$ and $\Delta R_{s_{\Delta\tau}}$ owing to their similar amplitudes, spectral shapes but opposing signs. Because of this, the top-of-atmosphere reflectance spectrum becomes independent of aerosol optical thickness for higher surface albedo regimes (Figure 2.4).

Over a dark surface such as the ocean, top of atmosphere reflectance in the continuum is unique at different aerosol loads (Figure 2.4, left panel). The variation in the top of atmosphere reflectance in the continuum reduces as the instrument points more towards the nadir. In such geometries, R_s can play a more significant role than R_p and reduce the available information on τ in the $R(\lambda, A_s)$ spectrum. For bright surfaces, the variation in the top of atmosphere reflectance spectrum is less for steeper geometries relative to the same geometries over the ocean (Figure 2.4, middle panel, green and blue line). There can also be cases where, provided sufficiently high aerosol loading, the top of atmosphere

reflectance spectrum in the continuum can be independent of aerosol optical thickness over very bright surfaces such as vegetation (Figure 2.4, right panel, green line). In such cases, more than one value of τ results in the same top of atmosphere reflectance. Henceforth in this chapter, this phenomenon is termed as aerosol-surface ambiguity.

A loss in aerosol information can have special implications in the minimisation of the cost function. As observed in Figure 2.5, for lower surface albedo regimes there exists a single minimum of the cost function. For such scenes, if the a-priori aerosol optical thickness is far from the true value, the gradient is sufficiently large such that a small change in the state vector between iterations leads to a significant minimisation of the cost function. As the surface albedo increases, this gradient decreases significantly, and can also result in the presence of multiple minima in the cost function (Figure 2.5, right) if the state vector is far away from the truth. This makes the retrieval dependent on the initial guess of τ.

Because of a model error (described in Figure 2.5) in the aerosol layer height between $\mathbf{y}$ and $\mathbf{F}(\mathbf{x},\mathbf{b})$ (in Equation 2.2), the global minimum of the cost function shifts away from the true τ. This shift is biased higher than the truth if the aerosol layer is lower in the atmosphere in comparison to the aerosol layer in the synthetic true spectrum, because the model has to compensate the extra absorption by molecular oxygen. If the aerosol layer is higher in the atmosphere, the minimum of the cost function is situated at a τ lower than the true τ. As observed in Figure 2.5 (left, red line), this shift of the cost function minimum from the true τ is larger over bright surfaces for a viewing angle close to nadir, where R_s is more dominant. For the same angle, the global minimum over a dark surface is situated at the true τ value, even with the presence of a model disagreement with the simulated 'true' spectrum. As the viewing angle increases over the bright surface, R_p increases and the global minimum of the cost function moves closer towards the true τ.

If the a-priori error assigned to aerosol optical thickness is large, presence of aerosol-surface ambiguities can result in non-convergences. Because the a-priori part of the cost function has a smaller value than the measurement part, reducing a-priori error assigned to the aerosol optical thickness does not necessarily guarantee a solution to this issue since it does not remove the multiple-minima present in the cost function. Since errors between aerosol optical thickness and aerosol layer height are correlated [12], a large error in the optical thickness will lead to a large error in the aerosol layer height estimate. The next section discusses the sensitivity of the aerosol layer height algorithm to this phenomenon by introducing model errors in a simulation environment.

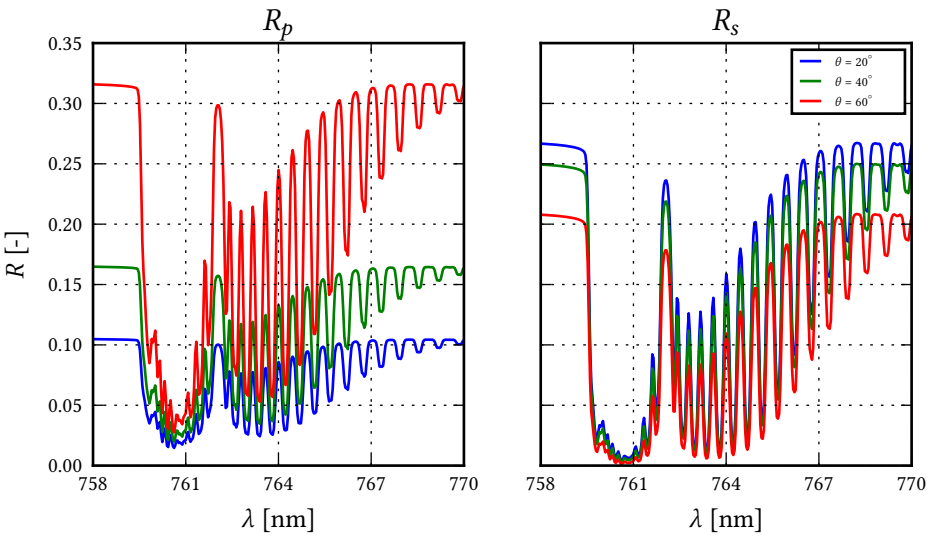

Figure 2.1: R_p and R_s for increasing viewing zenith angle θ over a surface with an albedo of 0.4 at 760 nm. The solar zenith angle is fixed at 45° and a relative azimuth angle of 0°. Aerosol optical thickness is fixed at 1.0 for an aerosol single scattering albedo of 0.95. Aerosol scattering phase function is a Henyey-Greenstein with g = 0.7. The aerosol layer is situated at 600 hPa, with a thickness of 50 hPa.

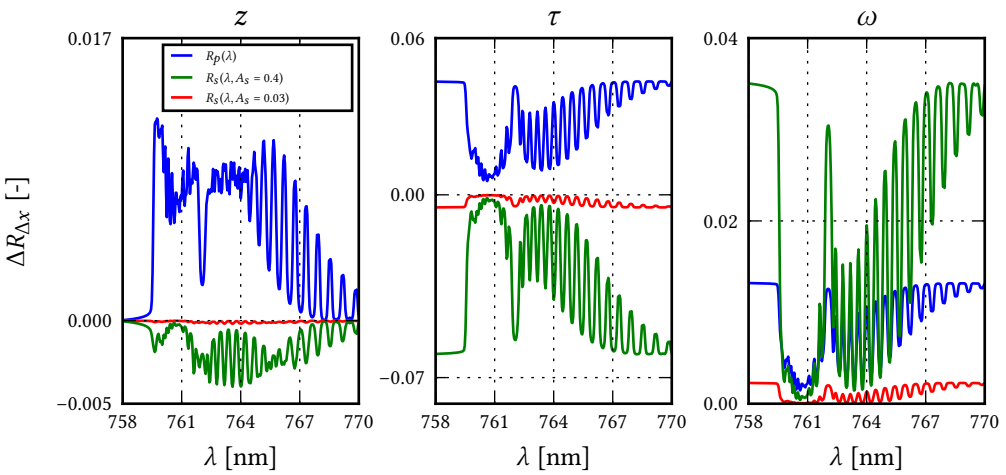

Figure 2.2: $\Delta R_{p_{\Delta x}}$ (in blue) and $\Delta R_{s_{\Delta x}}$ (in red, for A_s = 0.03 and green for A_s = 0.4) to model parameter x in the oxygen A-band, as measured by a nadir pointing instrument for a solar zenith angle at 45°. $\Delta R_{p_{\Delta x}}$ is calculated as the difference of the modeled top-of-atmosphere reflectance between two atmospheres, both cloudless and contain aerosols, which differ only in the parameter x for values x_a and x_b, according to Equation 2.6. The phase function is described by a Henyey-Greenstein model with an anisotropy factor of 0.7, and the thickness of the aerosol layer is fixed at 50 hPa. **Left**: τ = 1.0 and ω = 0.95 with different aerosol layer heights, z_a = 600 hPa and z_b = 800 hPa. **Middle**: τ_a = 1.0 and τ_b = 0.5 at z = 600 hPa and ω = 0.95. **Right**: τ = 1.0 and z = 600 hPa for ω_a = 0.95 and ω_b = 0.9. Y-axis has optimised per plot.

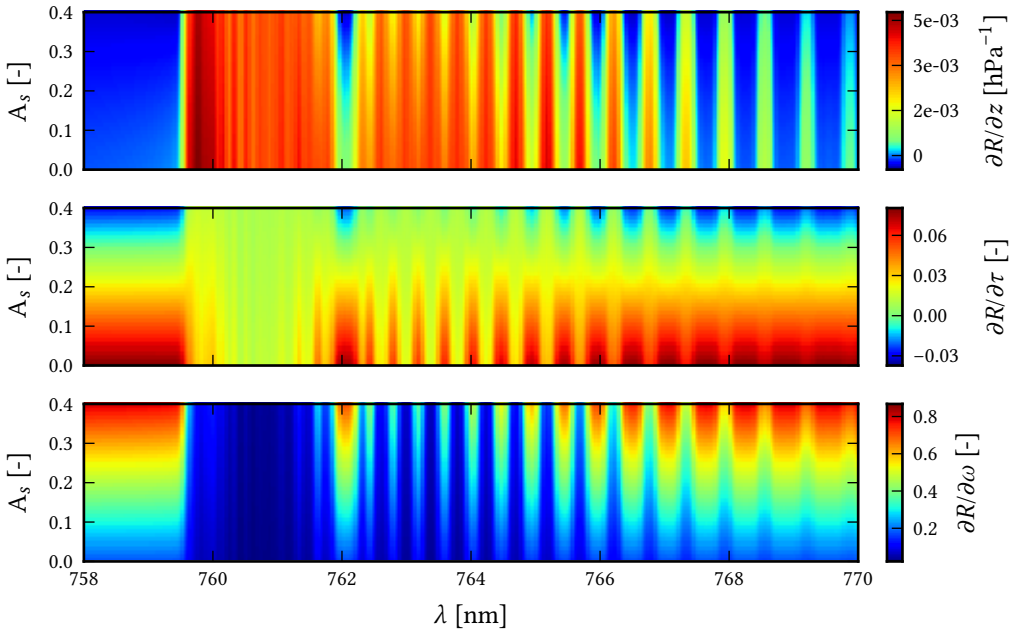

Figure 2.3: Derivative of reflectance with respect to aerosol properties for different surface albedos A_s. The z is centered around 600 hPa, with τ = 1.0, ω = 0.95, and a Henyey-Greenstein phase function with g = 0.7. The solar zenith angle is 45° and the viewing zenith angle is 0°. **Top**: derivative of reflectance with respect to z. **Middle**: derivative of reflectance with respect to τ. **Bottom**: derivative of reflectance with respect to ω. The colorbar has optimised per plot.

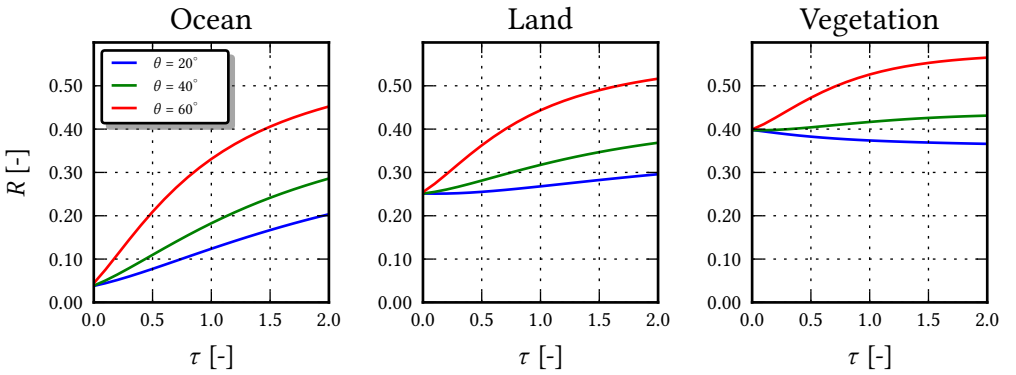

Figure 2.4: Top-of-atmosphere reflectance at 755 nm, well outside the oxygen A-band, from simulated spectra of scenes containing aerosols over dark and bright surfaces. Red, blue and green lines represent different viewing zenith angles θ, as a function of increasing aerosol optical thickness. Aerosols have a single scattering albedo of 0.95, and the aerosol scattering is described by a Henyey-Greenstein phase function with $g = 0.7$. Aerosol layer is situated at 925 hPa. The solar zenith angle is 45° and a relative azimuth angle is 0°. **Left**: The surface albedo is 0.03 at 760 nm, typical over the ocean. **Middle**: The surface albedo is 0.25 at 760 nm, typical over land. **Right**: The surface albedo is 0.4 at 760 nm, typical over vegetated land.

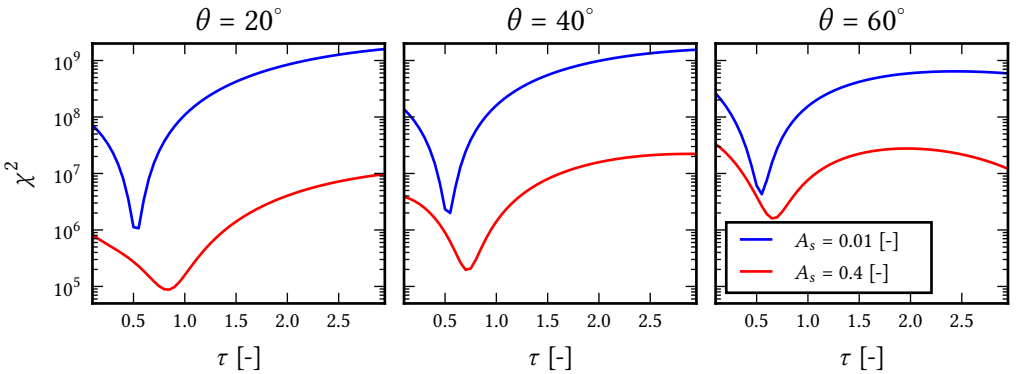

Figure 2.5: Cost function (χ^2) for retrieving aerosol optical thickness as a function of aerosol optical thickness per iteration (τ) for a dark and a bright surface. The true aerosol optical thickness is 0.5, and the aerosol layer is situated at 600 hPa with a 50 hPa layer thickness. The aerosol single scattering albedo is fixed at 0.95, for a Henyey-Greenstein aerosol phase function with $g = 0.7$. The solar zenith angle is fixed at 45° for varying viewing angles as specified in the plot titles. The relative azimuth angle is 0°. The state vector also contains aerosol layer height, whose a-priori value is fixed at 700 hPa.

2.4 Error analysis

In DISAMAR, forward models for simulation and retrieval have been kept separate so that errors can be introduced into the simulated spectra to mimic errors in a real retrieval scenario. In this section, the instrument model of the Sentinel-4 UVN near infrared spectrometer is used. The wavelength range for simulations and retrievals is between 758 nm and 770 nm. A comparative analysis of biases in the retrieved aerosol layer height is conducted over ocean (A_s = 0.03) and land (A_s = 0.25, and A_s = 0.4). Bias in the aerosol layer height is defined as the difference between retrieved and true aerosol layer height (in hPa) — a positive sign indicates that the aerosol layer is retrieved below the true aerosol layer height. The aerosol layer height retrieved is a single layer for the entire atmospheric column, with a fixed thickness of 50 hPa.

2.4.1 Sensitivity to model error in the aerosol layer thickness

In a typical real-world scenario, aerosol plumes can be as thick as 200 hPa in the atmosphere, or more. We simulate a scene containing an aerosol layer that extends approximately from the surface (1000 hPa) to 800 hPa in the atmosphere. The true τ is 1.0, and the a-priori τ is 0.5. The a-priori value of the aerosol layer height is 650 hPa, and the aerosol layer thickness is fixed at 50 hPa. In an ideal retrieval instance, the retrieved aerosol layer height (which has a thickness of 50 hPa) should coincide with the height of the simulated thicker aerosol layer. We observe that, in general, the error in the retrieved aerosol layer height reduces as the viewing zenith angle increases (Figure 2.6, top left). This is explained by a reduction in R_s and an increase in R_p, (Figure 2.1, red line), which explains why difference in errors between retrievals over different surfaces reduces with an increase in viewing angle (Figure 2.6, top left, high viewing zenith angles).

At lower viewing zenith angles, the difference in aerosol layer height errors between retrievals over the different surfaces is the largest, since the effect of R_s interfering with R_p is significantly larger (Figure 2.1, blue line), which increases with an increase in surface albedo (Figure 2.2, left). The retrieved aerosol layer is biased towards the surface in all three surface albedo scenarios, with the aerosol layer being placed closer to the surface if the surface albedo is brighter. This should not suggest a sensitivity to the geometrical thickness of the aerosol layer. As the surface albedo increases, the number of photons that pass through the atmosphere to interact with the surface before reaching the detector increases. These photons have a longer path length, which results in an increased absorption by oxygen at specific spectral points with weak oxygen absorption lines. In comparison to photons at wavelengths with strong oxygen absorption lines, these photons have a higher SNR since relatively more of them reach the detector. A higher SNR ensures lower noise, and hence a higher value in the inverse of the measurement error covariance matrix S_ϵ. If a spectral point has a higher value in S_ϵ^{-1} matrix, it has a higher representation in the cost function (in Equation 2.2), and hence a higher preference (or weight) in the optimal estimation. Because of this, the retrieval prefers to retrieve an aerosol layer height described by photons that travel through the aerosol layer closer to the surface. If, however, the aerosol optical thickness is so large that the photons cannot penetrate the aerosol layer, the retrieved aerosol layer height would be more accurate. Retrieving height of optically thin aerosol layers can also be quite challenging, owing to the fact that these layers will

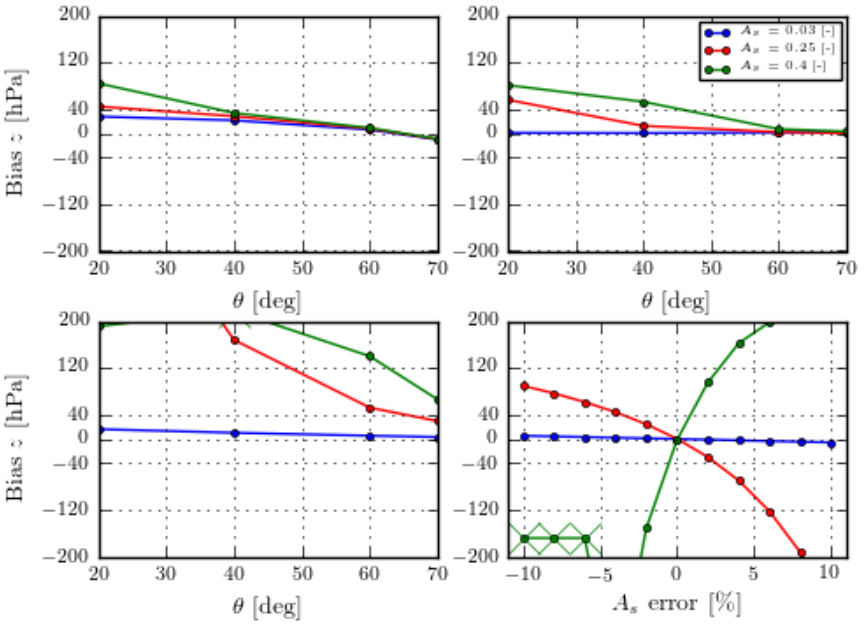

Figure 2.6: Bias in aerosol layer height in the presence of model errors. Unless specified, the relative azimuth angle is 0° and the solar zenith angle is 45°, aerosol single scattering albedo of 0.95 and Henyey-Greenstein g of 0.7, and an aerosol layer at 650 hPa. **Top left**: Model error is introduced in the thickness of the aerosol layer. The simulated spectra contains a 200 hPa thick aerosol plume extending from the 1000 hPa to 800 hPa. **Top right**: Model error is introduced in the aerosol phase function. The simulated scenes contain aerosols with scattering physics described by a Henyey-Greenstein phase function with g = 0.65 and retrieved with g = 0.7. **Bottom left**: Model error is introduced in the single scattering albedo. The simulated spectra contains aerosols with ω = 0.95, which is fixed in the retrieval forward model at 0.90. **Bottom right**: A relative error is introduced in the surface albedo. The viewing angle is fixed at 20°.

allow more photons to pass through and interact with the surface, leading to an increase in R_s, and hence an increase in the cancellation between R_p and R_s. As a result of this, large biases in the retrieved aerosol layer height can be expected for optically thin layers over bright surfaces.

Another consequence of retrieving aerosol layer height over bright surfaces is that the retrieval may become more susceptible to model error in aerosol and surface properties, such as the aerosol phase function anisotropy factor g, the aerosol single scattering albedo ω and especially the surface albedo A_s, which are fixed in the model. These are investigated in the following.

2.4.2 Sensitivity to model error in the aerosol phase function

The presence of a model error in the aerosol phase function can result in large biases if the surface is bright (Figure 2.6, top right). For a higher surface brightness and a viewing angle close to nadir, this bias is larger. As the viewing angle increases, the biases reduce significantly. The correlation of bias with surface albedo suggests that biases cause by model errors are exacerbated by the surface contribution R_s, which reduces as viewing angle increases (Figure 2.1, right).

2.4.3 Sensitivity to model error in aerosol single scattering albedo

From Figure 2.3, aerosol single scattering albedo plays an increasingly significant role in the retrieval of aerosol layer height as the surface gets brighter. Because of this, a mis-characterisation of aerosol single scattering albedo in the model can lead to very large biases over bright surfaces (Figure 2.6, bottom left), and also non-convergences. This is not the case for retrievals over the ocean, since the influence of aerosol single scattering albedo on the oxygen A-band spectrum is low. It is observed that, as the viewing angle increases, these biases drop significantly. This is again attributed to the decrease in R_s and increase in R_p with increasing viewing angle (again, over a Lambertian surface).

2.4.4 Sensitivity to model error in surface albedo

Surface albedo is a critical component in the accurate retrieval of aerosol layer height over bright surfaces. Because it is a fixed parameter in the forward model, an error in the surface albedo can result in large biases in the retrieval. To simulate model errors, relative errors of -10% to 10% are introduced in the retrieval forward model, such that the surface is modeled darker or brighter than the true value. For relative errors of ±10%, the retrieved aerosol layer height can be biased more than two orders of magnitude larger over land than over ocean (Figure 2.6, bottom right). For retrievals over a bright surface such as vegetation (A_s = 0.4 or greater), the model error can result in non-convergences. As the model error reduces, retrievals over land with a surface albedo of 0.25 become more acceptable. However, over very bright surfaces, an inaccuracy in surface albedo of more than 2% can result in biases greater than 100 hPa.

The next section demonstrates the implication of these errors in a real retrieval scenario.

2.5 Demonstration case: 2010 Russian wildfires

The 2010 Russian wildfires began in late July and lasted for several weeks until the beginning of September. Literature reports droughts and record summer temperatures in the same year as a precursor to the wildfires, both of which have been attributed to climate change [5]. A consequence of the forest fires were optically thick aerosol plumes over the country, especially over Moscow. In the first few weeks of August, 2010, due to the presence of a strong anti-cyclonic circulation pattern in the atmosphere, the impact of biomass burning aerosols on air quality in Moscow was markedly larger than what was observed from previous wildfire incidences — the UV Aerosol Index (AI) reported by the Ozone Monitoring Instrument (OMI) on board the NASA Aura mission observed an increase by a factor of 4.1 from previous years [19] over Moscow, due to aerosol plumes originating from the South and East of the city.

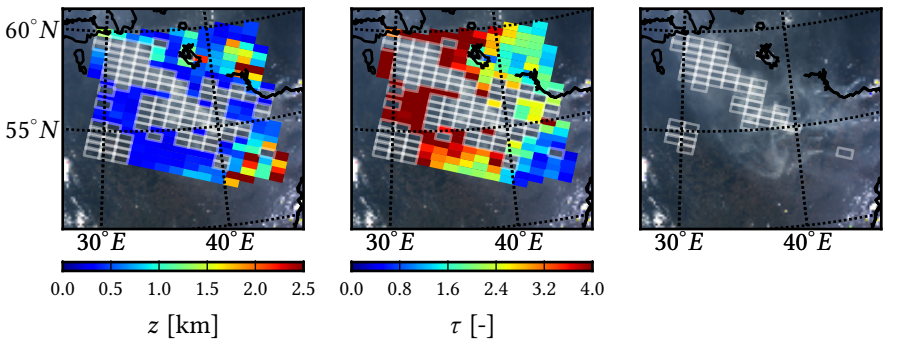

Figure 2.7: **Left**: Retrieved aerosol layer height from GOME-2A measurements of the 2010 Russian wildfires, in kilometers above the ground with the aerosol layer height retrieval algorithm. Empty white boxes represent pixels that do not converge to a solution. **Middle**: Retrieved aerosol optical thickness from the same retrievals. **Right**: GOME-2A pixels for which there exist possible aerosol-surface ambiguities (empty pixels with white borders).

The aerosol plume above Russia on the 8th of August, 2010 serves as a test case for the aerosol layer height retrieval algorithm, due to fairly cloud-free conditions and the optical thickness of the aerosol plume (see Figure 2.7, right). Because of this, we do not employ a cloud-screening method. The GOME-2A instrument crosses over the scene at approximately 09:45 hrs - 09:47 hrs at local time. The GOME-2A pixels within the region of interest are recorded between 0745 hrs UTC and 0748 hrs UTC, at approximate latitude bounds of 52° and 60° and longitude bounds 29° and 45°. This corresponds to 255 pixels in total. Meteorological information relevant to the retrieval are temperature-pressure profiles and surface pressure, acquired from the European Center for Medium-Range Weather Forecast (ECMWF) ERA-Interim database [4] at the GOME-2A pixel using nearest neighbour interpolation. Surface albedo is derived using nearest neighbour interpolation for version 1.3 of GOME-2A LER climatology derived from Tilstra et al. [15], which is at a 1° x 1° grid. Typical values of the surface albedo over the region of interest is around 0.21. In the inverse method, the a-priori value of the aerosol layer height is approximately 800 hPa. The a-priori aerosol optical thickness is 1.0 at 760 nm.

CALIOP data is used for validation, which provides vertical distribution of aerosols and clouds for a footprint of approximately 70 m, with a 5 km horizontal resolution [18]. While the coverage of the instrument is not as expansive as the GOME-2 instrument, the level of information available from CALIOP gives a good idea on the vertical position of aerosols in the atmosphere. For a better validation dataset, CALIOP data recorded between coordinates 52.0° latitude and 64.0° latitude, approximately around 1045 hrs UTC is used for comparison of GOME-2A aerosol layer height retrieval results. The Level-1 CALIOP attenuated backscatter data from 1064 nm is used because lidar in the visible region (532 nm) can get heavily attenuated over optically thick plumes. As can be seen from Figure 2.8, the aerosol layer is situated in between the surface and 5 km above the surface. In total, 82 GOME-2A pixels falling within 100 km of the CALIPSO track are considered for comparison.

The operational algorithm retrieves aerosol layer height and aerosol optical thickness, with fixed a-priori values, as mentioned in Table 2.1. Following evaluation of the algorithm on GOME-2A pixels by Sanders et al. [12], the surface albedo is not included in the state vector. The single scattering albedo is not fitted in the sensitivity analyses in order to maintain consistency with the current operational algorithms for the Sentinel missions, which currently do not fit this parameter.

2.5.1 Results from the retrieval algorithm

Out of the chosen 255 GOME-2A pixels, 155 pixels converged and 100 pixels failed to converge to a solution (40% of the pixels do not converge). The algorithm retrieved aerosol layers primarily in the lower troposphere, roughly within 0 - 3 kilometers (Figure 2.7, left). The mean aerosol layer height retrieved is 714 m above the ground with a standard deviation of 647 m and a median of 450 m. The retrieved aerosol layers are optically thick (Figure 2.7, middle), with an mean retrieved aerosol optical thickness of 3.0, a standard deviation of 1.8, and a median of 2.5. The retrievals over the primary aerosol plume do not converge to a solution.

Figure 2.8 (top) provides results of retrieving aerosol layer height over the chosen 82 GOME-2A pixels co-located to the CALIPSO track. The CALIOP backscatter data shows that the aerosol plume extends from the ground to approximately 4 km between latitudes 53° and 60°. Beyond 60° latitude, the aerosol layer is elevated. Of the 82 pixels, 52 converge to a solution. From Figure 2.8, it is observed that the retrieved aerosol layer heights are generally biased closer to the surface. This is explained by the increase in surface contribution R_s which represents photons passing through the atmosphere and interacting with the surface before reaching the detector. The spectral points representing these photons have a higher weight in the optimal estimation in comparison to the photons that do not interact with the surface and hence the aerosol layer height is retrieved closer to the surface.

In Figure 2.8, the retrieval does not converge to a solution between latitudes 57° and 60°. This area also corresponds to the primary biomass burning plume in Figure 2.7. However, the estimated aerosol layer height in the last iteration for these pixels seems to be located within the aerosol plume (Figure 2.8, top, white crosses between latitudes 57° and 60°). To investigate this, we retrieve τ from the top-of-atmosphere reflectance in the continuum with different a-priori optical thickness values in order to test whether the non-uniqueness

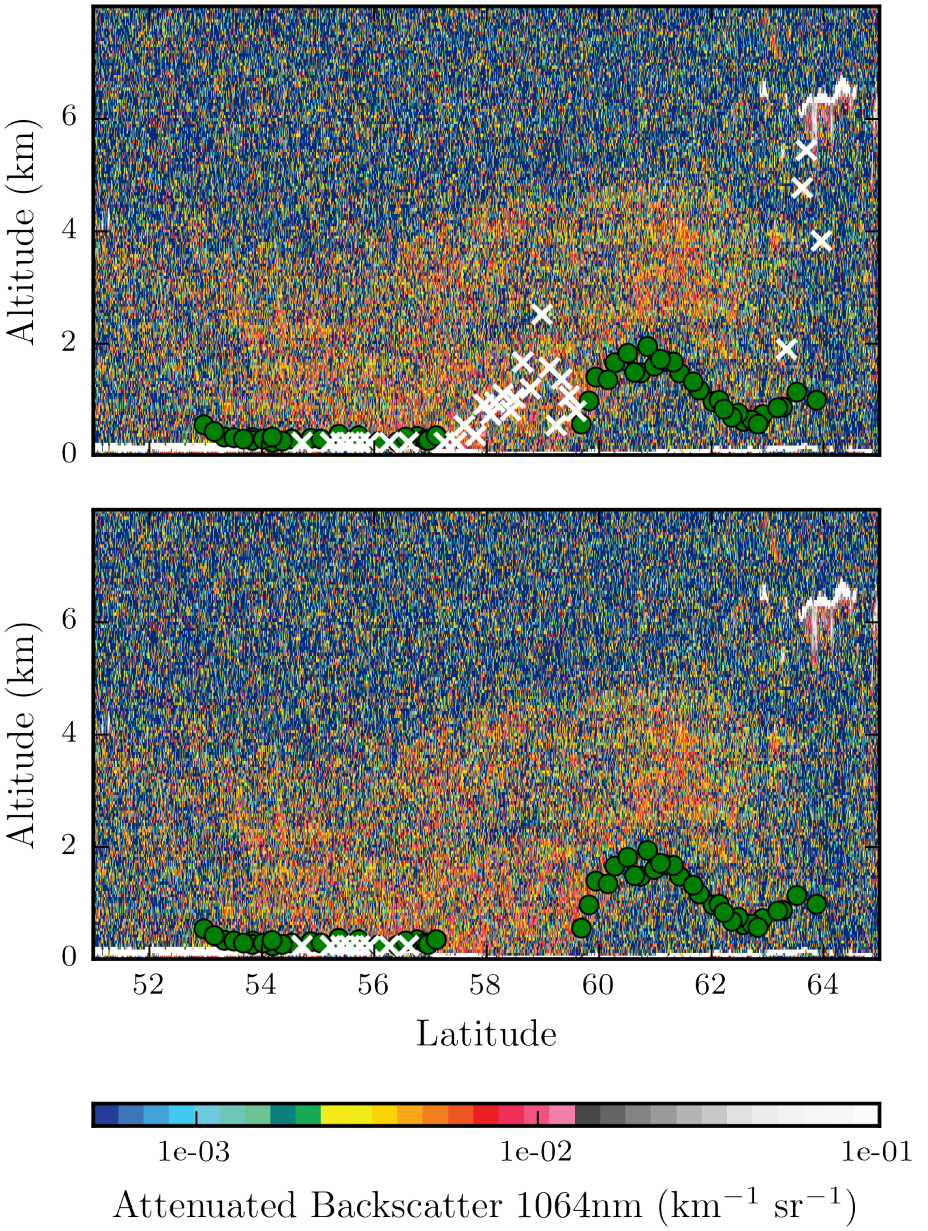

Figure 2.8: CALIOP lidar backscatter cross-section of a track falling within the region of interest over the 2010 Russian wildfire plume on 8th of August, 2010. **Top**: green dots and white crosses are GOME-2A pixels falling within 100 km of the CALIPSO ground track — green dots represent converged aerosol layer heights, and white crosses represent the aerosol layer heights at the last iteration for pixels that do not converge to a solution. These retrieved altitudes are reported in km above ground surface. **Bottom**: Retrieval results are presented for pixels for which the the prefit method retrieves both $\tau_a^{'}$ and $\tau_b^{'}$ at similar values.

Table 2.1: A-priori and validation information required to process data over 2010 Russian wildfires on the 8^{th} of August, 2010.

parameter	**source**	**remarks**
radiance and irradiance	GOME-2A	data between latitudes 52° and 60° and longitudes 29° and 45° (255 pixels)
solar and satellite geometry	GOME-2A Level 1-b data	
surface albedo A_s	[15]	GOME-2A LER at 1° x 1° grid at 758 nm and 772 nm
surface pressure p_s	ERA-Interim	
temperature pressure profile	ERA-Interim	
aerosol optical thickness τ		state vector element, a-priori = 1.0
aerosol layer height h_{mid} [km]		state vector element, a-priori = p_s - 200 hPa
aerosol single scattering albedo ω		fixed at 0.95
aerosol phase function $P(\theta)$		Henyey-Greenstein with asymmetry factor g of 0.7
cloud mask		none
validation	CALIOP lidar profiles	5 km × 5 km total attenuated backscatter at 1064 nm

of aerosol optical thickness is a potential cause of retrieval non-convergence.

2.5.2 Retrieving aerosol layer height with multiple a-priori aerosol optical thickness values

Aerosol optical thickness (τ) is first retrieved from the continuum before the oxygen A-band between 755 nm - 756 nm. τ is retrieved with two a-priori values τ_a and τ_b. In these retrievals, the aerosol layer height is kept fixed at any arbitrary value, since its value will hardly affect the continuum.

First, τ_a = 1.0 is chosen, and the retrieved solution $\tau_a^{'}$ is then used to decide the a-priori value τ_b. If the solution for $\tau_a^{'}$ is not reached, then $\tau_b^{'}$ is not calculated. In the case that $\tau_a^{'}$ is retrieved, τ_b is chosen in the following manner,

$$\tau_b = \begin{cases} \tau_a^{'}/2 & \text{if } \tau_a^{'} < \tau_a \\ \tau_a^{'} + 0.5 & \text{if } \tau_a \leq \tau_a^{'} < 10.0. \end{cases} \tag{2.8}$$

If the retrieval for $\tau_b^{'}$ fails, then we can infer a dependence on a-priori information. If the retrieval is successful, $\tau_a^{'}$ and $\tau_b^{'}$ are compared to check if they are similar using the following criterion,

$$\tau_a^{'} \approx \tau_b^{'} \text{ if } \mathbf{abs}(\tau_a^{'} - \tau_b^{'}) < T \times \mathbf{min}(\tau_a^{'}, \tau_b^{'}), \tag{2.9}$$

where T is a threshold, chosen to be 0.15. Increasing this threshold increases the margin of similarity of $\tau_a^{'}$ and $\tau_b^{'}$. This method is henceforth called the prefit method.

Applying the prefit method to the GOME-2A pixels processed previously, it is observed that out of 255 pixels, 215 pixels retrieve $\tau_a^{'}$ and 40 pixels do not. Upon analysis of these 40 pixels, it is observed that the these pixels do not converge because the retrieved aerosol optical thicknesses are in excess of 10.0, and DISAMAR stops the retrieval since τ reaches boundary conditions (beyond 20.0). Such large optical thicknesses may be attributed to the saturation of the top of atmosphere reflectance at very high aerosol loads, observed in Figure 2.4. It is also possible that these retrievals do not converge because of the presence of other model errors. Two pixels retrieve $\tau_a^{'}$ above 10.0, and hence are not considered for retrieving $\tau_b^{'}$.

From these 213 pixels, 209 pixels converge to $\tau_b^{'}$, whereas four pixels do not converge to a solution. These four pixels that do not converge are confirmed cases of the presence of aerosol-surface ambiguities, since the retrieval toggles between two values at every iteration until the maximum number of allowable iterations is reached. This is also a consequence of a non-unique top of atmosphere reflectance at high aerosol load scenarios. Out of the 209 pixels that retrieve both $\tau_a^{'}$ and $\tau_b^{'}$, 205 pixels have similar retrieved optical thickness values according to criterion in Equation 2.5.2. The rest have values which are off by more than 2.0.

From Figure 2.7 (right), pixels that contain aerosol-surface ambiguities primarily lie within the main aerosol plume. This is in-line with our expectation of the top of atmosphere being saturated at very high aerosol loads. Interestingly, these pixels also comprise 50% of the pixels that do not converge for aerosol layer height retrieval. Figure 2.8 (bottom)

provides a plot of the retrieval of CALIPSO co-located GOME-2A pixels, in which 22 pixels are absent from the plot (relative to Figure 2.8, top). These are pixels for which the prefit method retrieves different $\tau_a^{'}$ and $\tau_b^{'}$.

2.5.3 Discussion

Out of the 100 pixels that do not converge, 50 pixels have been identified which may be affected by aerosol-surface ambiguities. For a majority of these pixels, the retrieved aerosol optical thickness is typically beyond 4.0. It is possible that the true number of pixels that are affected by aerosol-surface ambiguities are higher than 50 pixels — our analysis is represented by a similarity criterion which relies on a similarity threshold T, which we have set at 15% (Equation 2.5.2). With a more strict criterion, more pixels affected by aerosol-surface ambiguities may be detected. Other non-convergences may be a result of model errors. Comparing our retrievals with the CALIOP attenuated backscatter profile from the infrared channel, we observe that our retrievals are biased closer to the surface, with non-convergences occurring for pixels within the primary biomass burning plume.

2.6 Conclusions

Depending on the surface brightness, the interaction of photons scattered from the atmosphere and the surface can result in a possible reduction of available aerosol information in the oxygen A-band spectrum. Our basis for this assertion depends on the distinction of aerosol information present in atmospheric path contributions R_p and surface contributions R_s to the top of atmosphere reflectance in the spectrum (Figure 2.1). The reduction of aerosol information increases with increasing surface brightness and decreasing viewing angle.

Our analyses reveal that the derivatives of the atmospheric path and surface contributions with respect to aerosol optical thickness are anti-correlated (see Figure 2.2, middle), which affects the derivative of reflectance with respect to aerosol optical thickness (see Figure 2.3). As the surface gets brighter, the magnitude of this derivative decreases, which reduces the sensitivity of the oxygen A-band spectrum to aerosol optical thickness. We expect this anti-correlation behaviour to be strong for viewing angles closer to the nadir, since R_p increases and R_s decreases with an increase in viewing angle (see Figure 2.1). One of the consequences of this interference is the effect on cost function for retrieving aerosol optical thickness. We report that the gradient of the cost function tends to become more shallow as the surface albedo increases. This is especially the case when the viewing angle is closer to the nadir (see Figure 2.5). We also notice that the cost function reduces at high aerosol optical thickness beyond the local minimum near the truth (Figure 6, right), which indicates the presence of multiple minima in the cost function. We attribute this behaviour to the saturation of the top of atmosphere reflectance at high aerosol loads (see Figure 2.4).

Similar analyses on the available information on aerosol layer height in R_p and R_s in the oxygen A-band reveals that parts of the oxygen A-band spectrum with a low absorption by oxygen have an increased cancellation of $\Delta R_{p\Delta z}$ and $\Delta R_{s\Delta z}$ (see Figure 2.2, left) and hence a reduction in aerosol layer height sensitivity in specific parts of the spectrum (see Figure 2.6, top). This increases as surface albedo increases. It is also observed that the derivative of $\Delta R_{p\Delta\omega}$ and $\Delta R_{s\Delta\omega}$ are both positive (see Figure 2.2, right), which increases the overall

sensitivity of the oxygen A-band spectrum to ω with increasing surface albedo. This is observed in the derivative of reflectance with respect to ω, which increases in magnitude with an increase in surface albedo.

The interaction between photons scattering back from the atmosphere (R_p) to the detector and photons that travel through the atmosphere to the surface and back to the detector (R_s) has direct consequences to the retrieval of aerosol layer height from the oxygen A-band. Over bright surfaces, the retrieval algorithm becomes increasingly susceptible to errors in the aerosol layer height estimates as well as non-convergences in the presence of model errors (see Figure 2.6). The sign difference of $\Delta R_{p\Delta z}$ and $\Delta R_{s\Delta z}$ also explains why retrieving a aerosol layer over bright surfaces with a 50 hPa thickness for thicker layer (say 200 hPa thickness) can be biased closer to the ground (see Figure 2.6, top left). To demonstrate this assertion in a real retrieval scenario, we have retrieved aerosol layer height over the 2010 Russian wildfires in the 8th of August, 2010, using measured oxygen A-band spectra recorded by the GOME-2 instrument on board the Metop-A satellite. For validating our retrievals, we refer to lidar measurements by the CALIOP instrument on board the CALIPSO mission which records, among other measurements, attenuated backscatter at 1064 nm over the same wildfires scene a few hours after the GOME-2A acquisition. Comparison of co-located GOME-2A and CALIPSO pixels reveals that, in the case of both boundary and elevated aerosol layers, the retrieved aerosol layer height is biased closer to the surface. For pixels with a high aerosol load, the algorithm fails to converge to a solution (see Figure 2.7). Over optically thick plumes, the retrieval becomes dependent on the a-priori aerosol optical thickness (see Figure 2.7, right).

The following chapter (Chapter 3) applies the knowledge gained from this study in the development of the aerosol layer height retrieval algorithm for retrieving aerosols over land.

References

[1] Chance, K. and Kurucz, R. (2010). An improved high-resolution solar reference spectrum for earth's atmosphere measurements in the ultraviolet, visible, and near infrared. *Journal of Quantitative Spectroscopy and Radiative Transfer*, 111(9):1289–1295.

[2] Corradini, S. and Cervino, M. (2006). Aerosol extinction coefficient profile retrieval in the oxygen A-band considering multiple scattering atmosphere. Test case: SCIAMACHY nadir simulated measurements. *Journal of Quantitative Spectroscopy and Radiative Transfer*, 97(3):354–380.

[3] de Haan, J. F., Bosma, P. B., and Hovenier, J. W. (1987). The adding method for multiple scattering calculations of polarized light. *Astronomy and Astrophysics*, 183.

[4] Dee, D. P., Uppala, S. M., Simmons, A. J., Berrisford, P., Poli, P., Kobayashi, S., Andrae, U., Balmaseda, M. A., Balsamo, G., Bauer, P., Bechtold, P., Beljaars, A. C. M., van de Berg, L., Bidlot, J., Bormann, N., Delsol, C., Dragani, R., Fuentes, M., Geer, A. J., Haimberger, L., Healy, S. B., Hersbach, H., Hólm, E. V., Isaksen, L., Kållberg, P., Köhler, M., Matricardi, M., McNally, A. P., Monge-Sanz, B. M., Morcrette, J.-J., Park, B.-K., Peubey, C., de Rosnay, P., Tavolato, C., Thépaut, J.-N., and Vitart, F. (2011). The ERA-Interim reanalysis:

configuration and performance of the data assimilation system. *Quarterly Journal of the Royal Meteorological Society*, 137(656):553–597.

[5] Hansen, J., Sato, M., and Ruedy, R. (2012). Perception of climate change. *Proceedings of the National Academy of Sciences*, 109(37):E2415–E2423.

[6] Henyey, L. C. and Greenstein, J. L. (1941). Diffuse radiation in the Galaxy. *The Astrophysical Journal*, 93:70.

[7] Landgraf, J., Hasekamp, O. P., Box, M. A., and Trautmann, T. (2001). A linearized radiative transfer model for ozone profile retrieval using the analytical forward-adjoint perturbation theory approach. *Journal of Geophysical Research: Atmospheres*, 106(D21):27291–27305.

[8] Munro, R., Lang, R., Klaes, D., Poli, G., Retscher, C., Lindstrot, R., Huckle, R., Lacan, A., Grzegorski, M., Holdak, A., Kokhanovsky, A., Livschitz, J., and Eisinger, M. (2016). The GOME-2 instrument on the Metop series of satellites: instrument design, calibration, and level 1 data processing – an overview. *Atmospheric Measurement Techniques*, 9(3):1279–1301.

[9] Rodgers, C. D. (2000). *Inverse methods for atmospheric sounding: theory and practice*, volume 2. World Scientific.

[10] Sanders, A. F. J. and de Haan, J. F. (2013). Retrieval of aerosol parameters from the oxygen A band in the presence of chlorophyll fluorescence. *Atmospheric Measurement Techniques*, 6(10):2725–2740.

[11] Sanders, A. F. J. and de Haan, J. F. (2016). TROPOMI ATBD of the Aerosol Layer Height product.

[12] Sanders, A. F. J., de Haan, J. F., Sneep, M., Apituley, A., Stammes, P., Vieitez, M. O., Tilstra, L. G., Tuinder, O. N. E., Koning, C. E., and Veefkind, J. P. (2015). Evaluation of the operational Aerosol Layer Height retrieval algorithm for Sentinel-5 Precursor: application to Oxygen A band observations from GOME-2A. *Atmospheric Measurement Techniques*, 8(11):4947–4977.

[13] Sanghavi, S., Martonchik, J. V., Landgraf, J., and Platt, U. (2012). Retrieval of the optical depth and vertical distribution of particulate scatterers in the atmosphere using O_2 A- and B-band SCIAMACHY observations over Kanpur: a case study. *Atmospheric Measurement Techniques*, 5(5):1099–1119.

[14] Seidel, F. C. and Popp, C. (2012). Critical surface albedo and its implications to aerosol remote sensing. *Atmospheric Measurement Techniques*, 5(7):1653–1665.

[15] Tilstra, L. G., Tuinder, O. N. E., Wang, P., and Stammes, P. (2017). Surface reflectivity climatologies from UV to NIR determined from Earth observations by GOME-2 and SCIAMACHY: GOME-2 and SCIAMACHY surface reflectivity climatologies. *Journal of Geophysical Research: Atmospheres*.

[16] Tran, H., Boulet, C., and Hartmann, J.-M. (2006). Line mixing and collision-induced absorption by oxygen in the A band: Laboratory measurements, model, and tools for atmospheric spectra computations. *Journal of Geophysical Research*, 111(D15).

[17] Tran, H. and Hartmann, J.-M. (2008). An improved O2 A band absorption model and its consequences for retrievals of photon paths and surface pressures. *Journal of Geophysical Research: Atmospheres*, 113(D18):D18104.

[18] Winker, D. M., Vaughan, M. A., Omar, A., Hu, Y., Powell, K. A., Liu, Z., Hunt, W. H., and Young, S. A. (2009). Overview of the CALIPSO Mission and CALIOP Data Processing Algorithms. *Journal of Atmospheric and Oceanic Technology*, 26(11):2310–2323.

[19] Witte, J. C., Douglass, A. R., da Silva, A., Torres, O., Levy, R., and Duncan, B. N. (2011). NASA A-Train and Terra observations of the 2010 Russian wildfires. *Atmospheric Chemistry and Physics*, 11(17):9287–9301.

3

A weighted least squares approach to limit errors in aerosol layer height retrievals over bright surfaces

Having established the information-cancelling effect that increasing surface brightness introduces on the derivative of top-of-atmosphere reflectance in the oxygen A-band with respect to aerosol properties, the question now is whether this physics can be exploited to ameliorate the effects of bright surfaces on the retrieved aerosol properties. The first indication is the cancelling of aerosol layer height information occurs in parts of the oxygen A-band spectra which have a low oxygen absorption cross section. A lower oxygen absorption cross section results in a higher photon count, relative to parts of the spectrum with a higher absorption cross section, in the measured signal. Consequently, the measured signal now has a higher signal to noise ratio for parts of the spectrum with less aerosol information.

The signal to noise ratio has a unique impact in the optimal estimation framework that the KNMI aerosol layer height retrieval algorithm is based on — in a way, it directs the retrieval to focus on parts of the spectrum more than other parts, in order to derive (in this context) aerosol information. This chapter discusses a method called dynamic scaling, which alters the signal to noise ratio by reducing its value at parts of the spectrum with low aerosol information than parts of the spectrum with higher aerosol information. The research goal covered in this chapter is,

Propose an alternative method to minimise the influence of the surface in aerosol layer height retrievals over bright surface albedo scenes.[1]

[1]This chapter is published in `https://doi.org/10.5194/amt-11-3263-2018`, 2018.

3.1 Introduction

Algorithms that estimate properties of atmospheric species from satellite measurements of top-of-atmosphere (TOA) radiance (including spectral signatures of gases) in planetary atmospheres typically employ an inverse method based on least squares. In the case of retrieving terrestrial properties, this approach requires spectrally resolved measurements of the TOA Earth radiance, solar irradiance, and a forward model as the minimal base ingredients to retrieve the state vector parameters (which are also model parameters). The goal of the least squares approach is to minimize a cost function, which aims to reduce discrepancies between the forward model and the measurement by iteratively manipulating state vector parameters. Upon minimization, the iterative scheme converges to a solution that, in principle, best describes the forward model's representation of the measurement.

Many atmospheric retrieval algorithms employ a weighted least-squares estimation (WLSE) method modified to include a-priori information on the state vector. An example of such an inverse method setup is optimal estimation (OE, Rodgers [17]), which is an attractive method particularly because of its efficacy in providing posteriori error statistics on the retrieved parameter. The KNMI aerosol layer height (ALH) retrieval algorithm uses an inverse method based on OE, and exploits the spectral structure of the near-infrared spectrum of the top-of-atmosphere radiance between 758 - 770 nm, where photons traveling through the Earth's atmosphere predominantly get absorbed by molecular oxygen. Oxygen is a well-mixed gas and has a pressure-dependent spectral structure of its absorption lines [12]; the further light in the oxygen A band passes through the atmosphere, the more it gets absorbed until it interacts with scattering species (such as clouds and aerosols) and scatters back to the TOA. It is this feature of the oxygen A band that has made it an attractive wavelength region for retrieving aerosol information [3, 7, 8, 10, 15, 18–21, 27]. The algorithm is operational for the TROPOspheric Monitoring Instrument (TROPOMI) on board the Sentinel-5 Precursor (S5P) mission [26], and is also a part of the Sentinel-4 (S4) and Sentinel-5 (S5) missions [11] under the Copernicus satellite program of the European Union.

Due to the large spectral variability in absorption within the oxygen A band, the measured TOA radiance and the measurement noise have a high dynamic range. The minimization of the propagation of measurement noise to the final retrieval solution should be a critical component of any retrieval algorithm. In WLSE, this is accomplished by the inverse measurement error covariance matrix which ranks the measurement on each detector pixel using the information available on the measurement noise. Due to the extent of the dynamic range of the measurement noise in the oxygen A band, this ranking matrix becomes a primary controlling entity; if the measurement noise is very large, the inverse noise variance is very low, which results in a lower rank to the measured signal from that specific detector pixel.

Since the measured signal is scene dependent, the spectral rank of each detector pixel is also scene dependent. This has special consequences over bright surfaces, where the dynamic range of the measured signal is much larger than over dark surfaces. Due to this, photons at wavelengths where the oxygen A band has a lower absorption cross section are less absorbed (subsequently traveling further into the atmosphere) and have a much larger representation in the WLSE method. A consequence of this, reported by Nanda et al. [14], is that the retrieved ALH values are inaccurate for measurements over land.

In order to account for unknown instrument and model errors, Sanders et al. [20] multiply the measurement error from L1b by two for their GOME-2 case studies and by ten in SCIAMACHY case studies (Sanders et al. 2018, manuscript in preparation) for retrieving ALH over ocean and land. They observe that increasing the measurement noise results in an increase in the number of retrieval convergences without significantly decreasing the accuracy of the retrieved ALH for the already-converged solutions. The method utilized by Sanders et al. [20] does not change the shape of the noise spectrum since it is multiplied by a constant. This chapter investigates a vector-based weighing scheme (we call it the dynamic scaling method, as opposed to the formal approach which is unscaled OE), which dynamically varies from scene to scene; such a weighting scheme changes the shape of the noise spectrum itself. The objective of the dynamic scaling method is to influence the inverse measurement error covariance matrix in its choice in ranking the instrument's detector pixels in its spectral dimension in order to maximize sensitivity to aerosol layer height. The study discussed in this chapter is a part of a series of chapters discussing the ALH retrieval algorithm developed at the KNMI [14, 18–20].

The retrieval algorithm is described in section 3.2, which provides a description of the forward model and the formalism of OE. The incompatibility of retrieving aerosol properties from oxygen A band measurements with the formal design of the measurement error covariance matrix are briefly discussed in the same section (section 3.2), before a full description of the proposed method in section 3.3 and a demonstration in a synthetic environment in section 3.4 are given. This method is applied to real data in section 3.5. The Russian wildfires in August 2010, which were discussed by Nanda et al. [14], are revisited to compare the two approaches. The data are derived from the GOME-2A (Global Ozone Monitoring Experiment on board the MetOp-A platform of the EUropean Organization for the Exploitation of METeorological SATellites, or EUMETSAT) instrument, and validated with a co-located CALIPSO (Cloud-Aerosol Lidar and Infrared Pathfinder Satellite Observation of the National Aeronautics and Space Administration, or NASA) overpass. The dynamic scaling method is further applied to the Portugal fires plume over Western Europe on the 17th of October, 2017, using data from the GOME-2B instrument, with validation from the ground-based EUropean METeorological services NETwork (EUMETNET, Alexander et al. [1]) ceilometer network in the Netherlands and Germany, along with radiosonde measurements of the relative humidity profile and the back trajectory of the aerosol plumes. This demonstration is followed by the conclusion in section 3.6.

3.2 The ALH retrieval algorithm

The algorithm is comprised of a forward model and an inverse method. The forward model uses a radiative transfer model described by de Haan et al. [4] to calculate the top-of-atmosphere (TOA) Earth radiance (I) in the oxygen A band. This is done by propagating incoming solar irradiance (E_0) in the oxygen A band through the Earth's atmosphere, which is described by an atmospheric model. Finally, this model is fitted to the measured spectrum to retrieve the primary unknown ALH, while fitting the Aerosol Optical Thickness (AOT). For more details, the reader may refer to Sanders et al. [20].

3.2.1 The forward model

The atmospheric model describes the interaction of photons with various components of the Earth's atmosphere that either absorb photons or scatter it in different directions. The oxygen absorption cross-sections are derived from the NASA Jet Propulsion Laboratory database, and first-order line mixing and collision induced absorption between O_2-O_2 and O_2-N_2 are defined from Tran et al. [24] and Tran and Hartmann [25]. The scattering species in the atmosphere include gases and molecules that follow Rayleigh scattering principles, aerosols, clouds and the surface. At present, the algorithm assumes cloud-free scenes, since the presence of clouds can result in large biases in the retrieved ALH [19, 20]. Aerosols are modeled as a single layer with a fixed thickness of 50 hPa. ALH is defined as the mid pressure of the aerosol layer, converted to a height above the ground. The aerosol layer has a constant aerosol extinction coefficient and a fixed aerosol single scattering albedo (ω). Scattering by aerosols is described by a Henyey-Greenstein phase function [9] with an anisotropy factor g of 0.7. This choice is motivated by the model's simplicity in describing scattering, which facilitates faster radiative transfer calculations than a more complex Mie scattering model. Currently, the surface is modeled as Lambertian.

The radiative transfer calculations are done line-by-line within the wavelength range of 758 nm - 770 nm, which requires a large computational effort for a single retrieval per iteration. In order to reduce computational time per iteration, polarization is ignored. This is a viable step, since the Rayleigh scattering cross section is very low in the near-infrared region. Because of the low Rayleigh Scattering cross section in the near-infrared, Rotational Raman Scattering can also be ignored.

The solar irradiance and Earth radiance are convolved with an Instrument Spectral Response Function (ISRF) $f_{\mathrm{ISRF}}(\lambda - \lambda_i)$ to simulate a spectrum observed by a satellite instrument. The TOA Reflectance (R) is computed as

$$y_i = R(\lambda_i) = \frac{\pi}{\mu_0} \frac{\int f_{\mathrm{ISRF}}(\lambda - \lambda_i) I(\lambda) d\lambda}{\int f_{\mathrm{ISRF}}(\lambda - \lambda_i) E_0(\lambda) d\lambda} \tag{3.1}$$

where μ_0 is the cosine of the solar zenith angle θ_0, and the subscript i is the index of the spectral channel. For a more in-depth description of the forward model, please refer to Sanders et al. [20]. All synthetic spectra presented in this chapter are from a hypothetical instrument with a Gaussian ISRF and a spectral resolution (FWHM) of 0.11 nm oversampled by a factor 3. These specifications are very similar to the Sentinel-4 Ultraviolet Visible and Near infrared (UVN) instrument. The sensitivity analyses conducted in this chapter may also be applicable to instruments with a lower spectral resolution. Further on in this chapter, experiments are conducted with measured spectra from the GOME-2 A and B instruments, which have a lower spectral resolution than the S4 UVN instrument.

3.2.2 The role of the measurement error covariance matrix in optimal estimation of ALH

The matrix $\mathbf{S}_\epsilon$ (Equation 2.4) plays a very important role in the WLSE framework by, essentially, ranking each spectral point based on the absolute measurement error in order to reduce the effect of measurement noise in the retrieved parameter. This is done by the $\mathbf{S}_\epsilon{}^{-1}$ matrix, which assigns a relatively higher value for spectral points with a lower noise covariance, and vice versa. The spectral points with a higher $\mathbf{S}_\epsilon{}^{-1}$ value essentially have

an overall stronger influence in the WLSE. The design of this WLSE framework makes the retrieval solution intrinsically dependent on the quality of the $\mathbf{S}_\epsilon{}^{-1}$ matrix. This matrix will always rank higher those spectral points that represent photons less absorbed by oxygen, i.e. those which travel through the atmosphere more easily, as the relative error at these spectral points is low. Because aerosols are weak scatterers of light, a large fraction of photons pass through the aerosol layer and interact with the surface before returning to the detector.

A spectrometer's detector pixel (in the spectral dimension) that contains a higher concentration of oxygen absorption lines receives less number of photons, in comparison to spectral points that contain fewer or no absorption lines. As a result of this, the relative error at these spectral points is larger, resulting in a lower signal-to-noise ratio (SNR). The expression of noise in the $\mathbf{S}_\epsilon$ matrix at each spectral point is, hence, dependent on the average absorption line strength within a spectral point. When the surface becomes brighter (e.g. over land), the number of photons traveling from the surface to the detector increases heterogeneously, depending on many contributing factors such as oxygen absorption line strength, aerosol optical thickness, aerosol layer height, and other atmospheric properties. In principle, however, the increase in signal for detector pixels with low oxygen absorption cross section is much higher than the same for detector pixels with a high oxygen absorption cross section. This will be reflected in the $\mathbf{S}_\epsilon$ matrix, which will (for example) rank measurements in the continuum higher than the same in the deepest part of the absorption band.

If the information on ALH is derived from absorption by oxygen, this design of the $\mathbf{S}_\epsilon{}^{-1}$ matrix does not encourage an accurate ALH retrieval. From a WLSE standpoint, the consequences of an increase in the number of photons in the TOA reflectance that travel to the surface can be quite significant, some of which are reported Figure 2.6. A possible avenue of improving the $\mathbf{S}_\epsilon{}^{-1}$ matrix involves its dynamical manipulation. The manipulation proposed in this chapter has been termed as the dynamic scaling method. The next section elucidates this method, with a comparative analysis against the formal inverse method, henceforth called the formal approach, presented further on in this chapter.

3.3 The dynamic scaling method

The dynamic scaling method identifies favorable spectral points for ALH retrieval by first identifying spectral points that are the least favorable. The noise is increased at these unfavorable points, while keeping the noise at the other points unchanged. These favorable and unfavorable spectral points are identified using a class of vectors known as modifying vectors (with the symbol M, and length equal to the number of spectral points).

To identify the unfavorable spectral points at which the measurement noise is to be modified, a modifying vector $\boldsymbol{M}_{\mathrm{A_s/z_{aer}}}$ is proposed as,

$$M_{\mathrm{A_s/z_{aer}}}(\lambda_i) = \frac{K_{\mathrm{A_s}}(\lambda_i)}{K_{z_{\mathrm{aer}}}(\lambda_i)}\ [\mathrm{hPa}], \tag{3.2}$$

where $K_{\mathrm{A_s}}(\lambda_i)$ is the derivative of the TOA reflectance with respect to surface reflectance at the i^{th} index of the spectral point on the detector, and $K_{z_{\mathrm{aer}}}(\lambda_i)$ is the same for z_{aer}. In principle, the ratio of $\boldsymbol{K}_{\mathrm{A_s}}$ and $\boldsymbol{K}_{z_{\mathrm{aer}}}$ is used as an identification tool since our primary

retrieval parameter is z_{aer} whose information reduces as A_s increases. This opposing nature is discussed by Nanda et al. [14] (Figure 3 and Figure 4 in their chapter), where they show an anti-correlation in the sensitivity of τ and z_{aer} in the atmospheric path contribution and surface contribution to the TOA reflectance. A large value in $M_{\text{A}_\text{s}/z_{\text{aer}}}(\lambda_i)$ represents spectral points in the measurement with more sensitivity to A_s than to z_{aer}. The motivation for choosing derivatives as the means for modification is also partly motivated from the fact that they are scene-dependent parameters, which make each modification unique to the scene.

Spectral points with a $M_{\text{A}_\text{s}/z_{\text{aer}}}(\lambda_i)$ higher than a specific threshold value should have a limited representation in the estimation — these are the unfavorable spectral points. We define this threshold as the modifying threshold (T), which is the 20^{th} percentile value of $\boldsymbol{M}_{\text{A}_\text{s}/z_{\text{aer}}}$. The threshold value set in our method has been chosen in a way to avoid scaling the deeper parts of the R and P branches in the A band. The choice of thresholding remains configurable to the user of this method, based on their requirements — in our case we have chosen to use a static rule for deciding the value of T, but this could also be made dynamic. An example of the shape of $\boldsymbol{M}_{\text{A}_\text{s}/z_{\text{aer}}}$ is provided in Figure 3.1 (top row).

The reason for increasing the noise at specific unfavorable spectral points is to increase the value of S_ϵ at these points. With a higher S_ϵ value, the ${\text{S}_\epsilon}^{-1}$ value will be lower, and hence that spectral point will have a lower weight in the estimation. In principle, this is equivalent to artificially increasing noise of measurements that contain less sensitivity to aerosol layer height. To do this, the modified SNR (denoted as SNR_M) is defined as,

$$\text{SNR}_M(\lambda_i) = \begin{cases} \text{SNR}(\lambda_i), & \text{if } M_{\text{A}_\text{s}/z_{\text{aer}}}(\lambda_i) < T \\ \text{SNR}(\lambda_i)/M_{\text{A}_\text{s}/\tau}(\lambda_i), & \text{otherwise} \end{cases} \tag{3.3}$$

where $M_{\text{A}_\text{s}/\tau}(\lambda_i)$ (belonging to the class of modifying vectors) is defined as the ratio between the derivative of the TOA reflectance with respect to the surface ($K_{\text{A}_\text{s}}(\lambda_i)$) and the same with respect to aerosol optical thickness (τ) at 760 nm ($K_\tau(\lambda_i)$),

$$M_{\text{A}_\text{s}/\tau}(\lambda_i) = \frac{K_{\text{A}_\text{s}}(\lambda_i)}{K_\tau(\lambda_i)}\ [\text{-}]. \tag{3.4}$$

The choice of modifying the SNR based on $\boldsymbol{M}_{\text{A}_\text{s}/\tau}$ arises from the fact that the amount of contribution by the aerosol layer to the TOA reflectance depends on its optical thickness. In such a case, we are interested in how much this contribution fares against the contribution from the surface. Information on both of these contributions can be inferred from the ratio of $\boldsymbol{K}_{\text{A}_\text{s}}$ and $\boldsymbol{K}_\tau$, which have comparatively similar shapes. If the measurement of a spectral pixel i is more sensitive to A_s, $M_{\text{A}_\text{s}/\tau}(\lambda_i)$ will be larger, and hence the noise at i will be increased, following Equation 3.3.

To run a retrieval using the dynamic scaling method, the derivatives of the reflectance with respect to A_s, z_{aer} and τ at 760 nm are calculated first, followed by the modification of SNR according to Equation 3.3. The state vector parameters τ and z_{aer} are then estimated using SNR_M. Users of this method may choose to scale the measurement error covariance matrix at each iteration, since the derivatives change at each iteration. Nevertheless, we have chosen to do it semi-statically since the measurement error covariance matrix is a static matrix throughout every iteration.

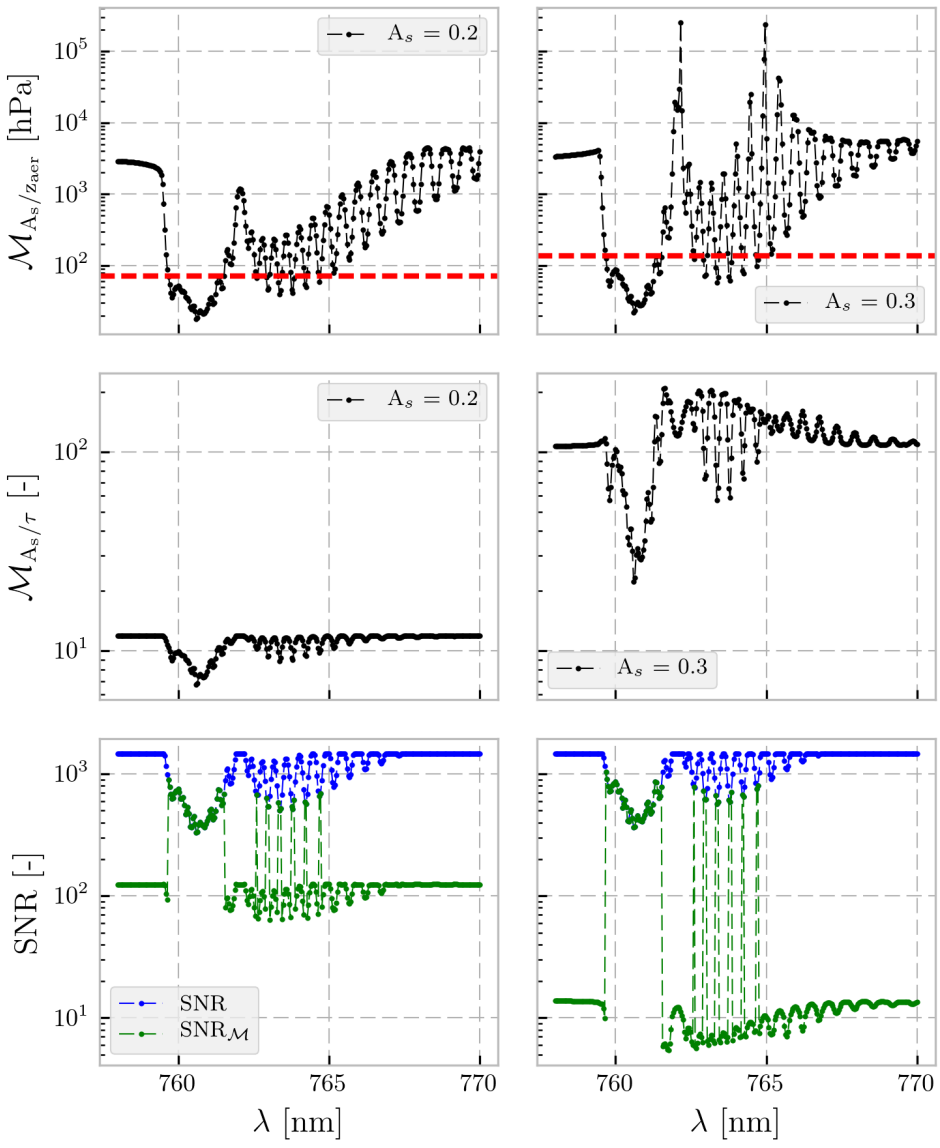

Figure 3.1: **Top row**: Modifying Vector $\boldsymbol{M}_{A_s/z_{aer}}$ as a function of wavelength λ. The solar zenith angle is 45°, the viewing zenith angle is 20° and the relative azimuth angle is 0°. The aerosol optical thickness (τ) is 0.5 at 760 nm, over a surface with an albedo of 0.2 (left column) and 0.3 (right column) at 760 nm. The height of the aerosol layer is 900 hPa with a pressure thickness of 200 hPa. The aerosol single scattering albedo is 0.95 and the aerosol scattering is described by a Henyey-Greenstein phase function with an asymmetry factor of 0.7. The red dashed line represents the modification threshold value T, which has been set at the 20th percentile of $\boldsymbol{M}_{A_s/z_{aer}}$ in this example. **Middle row**: Modifying function $\boldsymbol{M}_{A_s/\tau}$, Equation 3.4 as a function of wavelength. **Bottom row**: The blue line represents the unscaled SNR whereas the green line represents the modified SNR according to Equation 3.3.

Examples of modifying vectors and SNR_M are provided in Figure 3.1 (bottom row), which shows the robustness of the method in scaling the SNR for different surfaces. The spectra generated in the figure represents two scenes with identical atmospheric parameters, solar and satellite geometries, but different A_s. $\boldsymbol{M}_{A_s/z_{aer}}$, T and $\boldsymbol{M}_{A_s/\tau}$ for different surfaces are different — this is important, since over-scaling the SNR can force the retrieval to rank the measurements of photons traveling from the upper parts of the atmosphere higher, while ignore the same from the lower parts of the atmosphere. This is why the modifying vector $\boldsymbol{M}_{A_s/\tau}$ is chosen as a dynamically scene-dependent parameter (according to Equation 3.4), such that the scaling is large when A_s is large (Figure 3.1, mid row). In the next section, the dynamic scaling method is demonstrated and compared to the formal approach (which is the unscaled OE method) for synthetically generated spectra.

3.4 Sensitivity Analyses

To demonstrate the dynamic scaling method, synthetic spectra are generated for randomly varying values in z_{aer}, τ, solar-satellite geometry (θ, θ_0 and $\phi - \phi_0$), and A_s, while keeping other parameters constant. Noise is not added to the synthetic spectra. This method of randomly generating model parameters for generating synthetic spectra gives a broad picture of the method's behavior. Table 3.1 provides a brief overview of the input model parameters chosen for generating these spectra. An error is introduced in the forward model during retrieval, and the bias in z_{aer} (defined as retrieved - true) is used to assess retrieval. The a priori z_{aer} and τ are set at 825 hPa and true τ, respectively. While there are many possible sources of errors, this chapter presents two kinds of errors, a) error in the thickness of the aerosol layer, and b) error in the surface albedo database. A reason for limiting the retrieval experiment scope to these two errors in the atmospheric part of the forward model is due to the fact that they are one of the more common contributors to retrieval biases. In real cases, aerosol layers may not be concentrated in a single layer of 50 hPa thickness, and the true surface albedo may vary significantly (to the order of 10% relative errors) from a monthly database of Lambertian Equivalent Reflectivity (LER) values depending on many parameters. In total, 2000 synthetic spectra are generated for each synthetic experiment and the parameters z_{aer} and τ are estimated using both the formal approach and the dynamic scaling method, to be compared side-by-side. The results from analyzing biases in retrieved z_{aer} are plotted in Figure 3.2. Although the dynamic scaling method is specifically designed for land, retrievals over surfaces with a low A_s (less than 0.1) are also included.

3.4.1 Error in aerosol layer thickness

The synthetic spectra generated assume an aerosol layer thickness (p_{thick}) of 100 hPa, whereas the retrieval forward model assumes a 50 hPa thickness. For simplicity, a PDF (denoted as φ) of the biases of retrieved z_{aer} is calculated, the peak of which represents the value of maximum frequency of occurrence, and the full-width at half maximum of which represents the spread.

In comparison with the formal approach (Figure 3.2a), the peak of φ for the dynamic scaling method is closer to 0 hPa and has a larger magnitude (Table 3.2). The retrieval biases for $A_s \leq 0.1$ and above 0.1 are indicative of the robustness of the dynamic scaling method

Table 3.1: Input parameters for synthetic experiments.

name	value/remarks
atmospheric parameters	
A_s	0.01 - 0.4 @ 760 nm (Lambertian)
τ	1.0 - 5.0 @ 550 nm (or, 0.60 - 3.0 @ 760 nm)
z_{aer}	600.0 - 900.0 hPa
ω	0.95
g	0.7
Angstrom Exponent (Å)	1.5
temperature-pressure profile	mid-latitude summer
instrument parameters	
slit function FWHM	0.11 nm
spectral oversampling factor	3
slit function shape	Gaussian
solar-satellite geometry parameters	
θ (viewing zenith angle)	0° - 70°
θ_0	0° - 70°
$\phi - \phi_0$ (relative azimuth angle)	$\phi = 180^\circ$, ϕ_0 varied between 0° - 360°

in its scaling of the SNR (Table 3.2, p_{thick} bias row). For $A_s \leq 0.1$, the retrieval biases from both dynamic scaling and formal approach are almost identical. Splitting the results to $\tau \leq 2.0$ and $\tau > 2.0$, it is observed that the dynamic scaling method reduces retrieval biases of z_{aer} by 40% relative to the same from the formal approach for high aerosol loads, and about 11.5% for low aerosol loads. This is because a scene containing low aerosols allow for more interactions between photons and the surface, which results in ALH retrievals being biased closer to the surface. The dynamic scaling method ameliorates this behavior by reducing the sensitivity of the retrieval algorithm to these photons. The formal approach retrieves 27 more pixels than the dynamic scaling method for $A_s > 0.1$. An observation to note is that there are instances where even the dynamic scaling method can result in large retrieval biases (Figure 3.2b). Generally however, the dynamic scaling method is shown to reduce retrieval biases in the presence of model errors in the aerosol layer thickness.

3.4.2 Error in surface albedo database

For generating errors in surface albedo, randomly varying relative errors (with respect to the true surface albedo in the synthetic spectra) ranging between -10% to 10% were introduced to the retrieval forward model. The results heavily favor the dynamic scaling method, which shows a significant improvement in retrieval behavior over the formal method. The dynamic scaling method retrieves 73 more pixels than the formal approach (Table 3.2, A_s error row), while also having a much smaller spread of retrieval biases around the peak (Figure 3.2c). For $A_s \leq 0.1$, the dynamic scaling method and the formal approach are almost identical, with the dynamic scaling method having a smaller spread. For $A_s > 0.1$, however, the dynamic scaling method improves the spread of the retrieval biases significantly. The mean biases for the dynamic scaling approach are slightly larger than the same for the formal approach, and the spread of retrieval biases in Figure 3.2d indicates

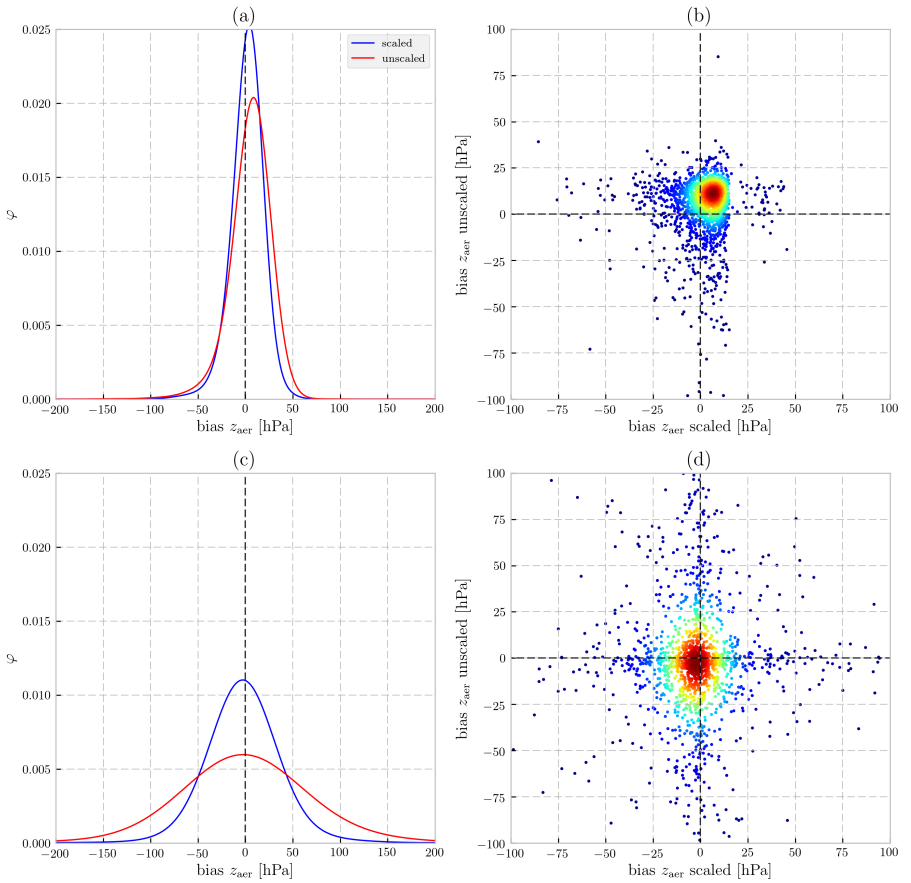

Figure 3.2: Biases in retrieved z_{aer} (in hPa) from synthetic measurements (2000 in total for each experiment) discussed in Section 3.4. The top row represents z_{aer} biases in the presence of a model error in the thickness of the aerosol layer. The bottom row represents z_{aer} biases in the presence of a model error in A_s. **(a), (c)** Probability distribution function φ of retrieval biases. Blue line represents results from the dynamic scaling method, and the red line represents the same for the formal approach. **(b), (d)** 2D density plot showing the distribution of biases (density ranges from high in red to low in blue). The x axis represents biases from the dynamic scaling method, whereas the y axis represents biases from the formal approach.

that the dynamic scaling method does not necessarily improve retrieval biases for all cases. However, the dynamic scaling method improves convergence from 89.3% to 92.3%, and reduces bias for 86.4% of the cases.

The analysis of retrieval biases from the synthetic sensitivity analyses are very encouraging for the dynamic scaling method. The method has shown significant improvements for $A_s > 0.1$ (at 760 nm) in the presence of two very relevant model errors. The fact that the dynamic scaling method is almost identical to the formal approach for $A_s \leq 0.1$ reaffirms the design of the modifying vector $\boldsymbol{M}_{A_s/\tau}$, which is intended to modify the SNR only if the modification is necessary. A similar split of results for $\tau \leq 2.0$ and $\tau > 2.0$ reveals that the dynamic scaling method is almost similar to the formal approach for low values of τ, and only results in significant improvements if the scene contains sufficient aerosols. Relative to z_{aer} biases from the formal approach, the biases from the dynamic scaling are reduced by 53% for $\tau > 2.0$, and is practically the same for $\tau \leq 2.0$. The success of the dynamic scaling method in a synthetic environment also confirms the fact that the design of the $\mathbf{S}_\epsilon{}^{-1}$ plays an important role in the biases of the retrieved z_{aer}. The next section applies the dynamic scaling method to measured spectra from GOME-2A and GOME-2B instruments over aerosol plumes from forest fire events in Europe.

Table 3.2: Results of the retrieval accuracy of z_{aer} from sensitivity analyses, split into two classes of A_s. The number of successful retrievals are reported in the 'retrieved' column. Columns with the heading A are the locations of the peak of φ, representing the z_{aer} bias value with the highest frequency of occurrence. The same with B are the full width at half maximum of φ, representing the spread of z_{aer} biases.

			Formal Approach			**Dynamic scaling**		
	As	total spec-tra	ret	A [hPa]	B [hPa]	ret	A [hPa]	B [hPa]
p_{thick}	≤ 0.1	453	453	8.70	22.31	453	8.70	20.04
	> 0.1	1547	1473	8.70	48.62	1446	3.34	38.76
		2000	1926	8.70	44.18	1899	4.70	35.56
A_s	≤ 0.1	451	451	-2.00	17.84	451	-2.00	14.36
	> 0.1	1549	1335	-2.00	178.27	1408	-3.34	96.07
		2000	1786	-2.00	150.64	1859	-3.34	81.85

3.5 Application to GOME-2 data

The GOME-2 instrument is a part of an operational mission by the European Organization for the Exploitation of Meteorological Satellites (EUMETSAT) to monitor trace gases and aerosols in the atmosphere. It is a spectrometer with an across-track scanning mirror that projects the TOA Earth radiance and solar irradiance through a prism on a grating to get information in the ultraviolet, visible and the near-infrared regions of the electromagnetic spectrum. In the oxygen A band, the spectral sampling interval is typically about 0.20 nm and the FWHM is 0.50 nm [13]. The GOME-2 instrument is designed to have a footprint size of 80×40 km^2 in the oxygen A band. The instrument also measures the linear polarization of Earth radiance, which is important for correcting measured signal to calculate reflectance accurately.

In this section, measured spectra from the GOME-2A instrument on-board the Metop-A satellite over Russian wildfires on August 8, 2010 (Figure 3.3a) and the Portuguese fire plume with the GOME-2B instrument on-board the MetOp-B satellite on October 17, 2017 over Western Europe (Figure 3.3b) are used. The formal OE method is compared to the dynamic scaling method by using space-based and ground based validation data. The noise spectrum is derived from the GOME-2 Level 1-b product, which is a combination of the systematic and random error components of the measurements [6].

Auxiliary information required for these retrievals are meteorological data, surface albedo, and a-priori values for the optimal estimation (Table 3.3). The meteorological data required are temperature-pressure profiles and the surface pressure, derived from the ERA-Interim database from Dee et al. [5]. These meteorological parameters are available in regular space ($1^\circ \times 1^\circ$ spatial resolution) and time grids, and require interpolation to the satellite pixel's coordinates and time of record. This interpolation is done using nearest neighbor. The surface albedo database is derived from Tilstra et al. [23] version 2.1, which has a resolution of $0.25^\circ \times 0.25^\circ$, derived from the GOME-2A instrument. The surface LER is chosen as the median of all LER database pixels intersecting the GOME-2 instrument pixel, at wavelengths 758 nm and 772 nm with linear interpolation used for calculating LER values at intermediate wavelengths. Algorithm settings are detailed in Table 3.3. The test cases chosen in this chapter are relatively cloud-free, although not fully.

For validation, atmospheric lidar data from satellite and ground-based instruments are chosen. For the 2010 Russian wildfires, the lidar attenuated backscatter at 1064 nm from the CALIOP instrument (Cloud-Aerosol LIdar with Orthogonal Polarization) on board NASA's CALIPSO (Cloud-Aerosol Lidar and Infrared Pathfinder Satellite Observations) mission are used. These data have a very good representation of the scattering ability of clouds and aerosols in the atmosphere at a vertical resolution of 60 m and a horizontal resolution of 5 km. For the 2010 Russian wildfires, the CALIPSO overpass is at 10:45 UTC. All GOME-2A pixels co-located withing a 100 km vicinity of a CALIOP profile are considered for validation. For the October 17, 2017 Portugal fire plume over Western Europe, ground-based ceilometer data are used for validation (Table 3.4). These ceilometers are a part of the ALC (Automated Lidars and Ceilometers) network of the E-PROFILE observation program in the framework of the EUropean METeorological services NETwork (EUMETNET). The parameter used for validation is the uncalibrated raw backscatter profile, since the chapter focuses on qualitatively assessing the aerosol height retrievals with the lidar backscatter profiles. Lidar profiles within an hour of the satellite instrument overpass

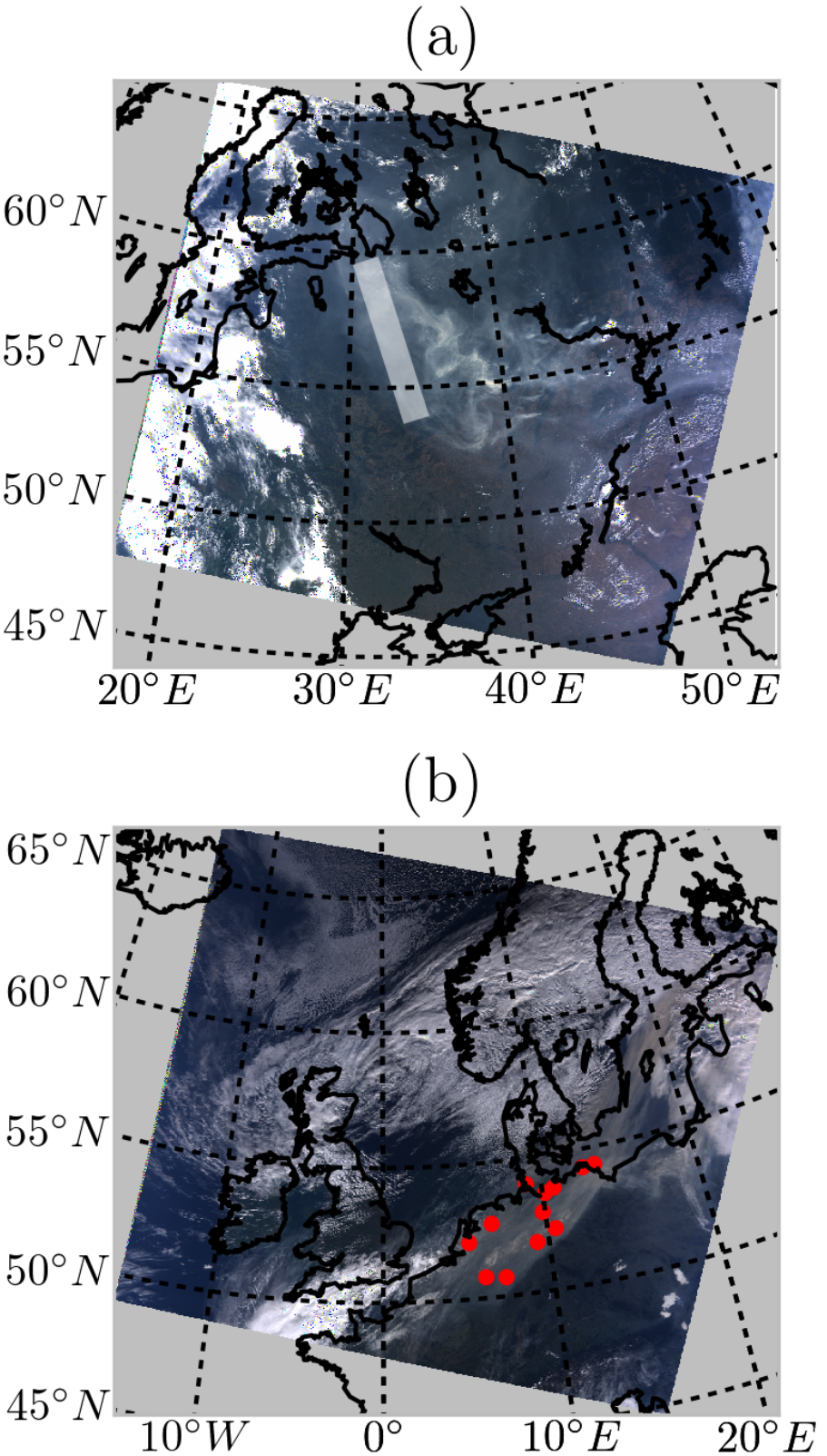
(a)
60° N
55° N
50° N
45° N
20° E
30° E
40° E
50° E
(b)
65° N
60° N
55° N
50° N
45° N
10° W
0°
10° E
20° E

time are averaged into a single averaged profile, in order to reduce noise. These lidars have a vertical range of approximately 15 m, and record data at a very high temporal resolution, nominally every 6 seconds [1]. Although CALIOP data is available for the plume over Western Europe for October 2017, CALIPSO does not have as good a co-location (both spatially and temporally) in comparison to the ceilometers.

Table 3.3: Input data and algorithm setup for retrieving aerosol properties from GOME-2 measurements in the oxygen A band.

parameter	**source**	**remarks**
radiance and irradiance	GOME-2A/GOME-2B	3 minute granules
SNR measured spectrum	GOME-2A/GOME-2B operational Level-1b product	3 minute granules
solar and satellite geometry	GOME-2A/GOME-2B Level 1-b data	3 minute granules
surface albedo A_s	Tilstra et al. [23] GOME-2A LER at 0.25° x 0.25° grid at 758 nm and 772 nm	
temperature-pressure profile	ERA-Interim	nearest-neighbor interpolated
aerosol optical thickness τ		state vector element, a-priori = 0.8
aerosol layer height h_{mid} [km]		state vector element, a-priori = 800 hPa
aerosol single scattering albedo ω		fixed at 0.95
aerosol phase function $P(\theta)$		Henyey-Greenstein model with anisotropy factor g of 0.7
cloud mask		none
validation (Russian wildfires in 2010)	CALIOP lidar profiles	5 km × 5 km total attenuated backscatter at 1064 nm
validation (Portugal fires in 2017)	Alexander et al. [1]	ground-based ceilometer network

3.5.1 Russian wildfires on August 8, 2010

The wildfire plumes in and around Moscow on the 8th of August, 2010 are chosen as the test case for the dynamic scaling method. Anti-cyclonic conditions on this day meant that the region of interest was predominantly cloud-free. This case is the same in Chapter 2 (but with a smaller pixel selection to only focus on the plumes), with the exception that the study presented in the current chapter uses a more-recent version of the surface LER product from Tilstra et al. [23] with a larger amount of GOME-2A data incorporated into its creation. The inclusion of this more-recent LER database has slightly improved the results from the formal approach, but not significantly. A MODIS Terra image taken over the region on the same day (Figure 3.3a) shows that the plume, although thick, is

Table 3.4: Ceilometer stations in Western Europe used for validating the the retrieved z_{aer} from GOME-2B for plumes from the October 17, 2017 Portugal wildfires.

name	**institute**	**coordinates**	**GOME-2B overpass time**
Hoogeveen	KNMI	52.74° 6.59°	09:31:10 UTC
Bonn	DWD	50.74° 7.19°	09:31:51 UTC
Luegde	DWD	51.86° 9.27°	09:31:18 UTC
Putbus	DWD	54.36° 13.47°	09:30:21 UTC
Luebeck	DWD	53.81° 10.71°	09:30:40 UTC
De Bilt	KNMI	52.09° 5.17°	09:31:21 UTC
Barth	DWD	54.34° 12.71°	09:30:25 UTC
Elpersbuettel	DWD	54.06° 9.01°	09:30:41 UTC
Soltau	DWD	52.95° 9.80°	09:30:56 UTC
Aachen	DWD	50.79° 6.03°	09:31:43 UTC
Hamburg	DWD	53.65° 10.10°	09:30:56 UTC
Braunschweig	DWD	52.29° 10.44°	09:31:05 UTC

non-homogeneously distributed in the scene, since the source of fires are very close to the region of interest described in the test case. There are 85 GOME-2A pixels over the primary biomass burning plume that are considered for retrieving aerosol optical thickness and aerosol layer height. During the iterations, if the inverse method estimates non-physical state vector values (such as an aerosol layer below the surface and a negative aerosol optical thickness or a cloud-like optical thickness) twice in a row, the retrieval is stopped and is said to have failed to converge. The algorithm also puts an upper cap of 12 iterations, beyond which the retrieval is also labeled to have failed to converge.

On applying the formal ALH retrieval approach, 49 pixels converge and 36 pixels do not converge to a solution (Figure 3.4 a,b). The fitted aerosol optical thickness values are in excess of 6.0 in many cases — on average, the fitted AOT is 5.34 with a standard deviation of 1.87 (Figure 3.5a, red). These values are too high - the AErosol RObotic NETwork (AERONET) station in Moscow observed, on the same day, values between 1.0 at 870 nm and 1.5 at 675 nm between 09:00 UTC and 10:00 UTC, whereas our retrieval estimates an AOT of 6.60 at 760 nm over Moscow using dynamic scaling. The distribution of fitted τ appears to be spatially inconsistent with the aerosol plume observed by MODIS Terra (Figure 3.4, a). The formal approach misses the primary biomass burning aerosol plume. The average retrieved height of the plume is 0.5 km above the ground, with a standard deviation of 0.15 km (Figure 3.5b, red histogram). Realistically, one can expect aerosols this close to the surface, especially if the boundary layer captures much of the pollution. However, aerosol-corrected boundary layer height modeled by Péré et al. [16] for the same day over Moscow shows that the atmospheric boundary layer is approximately around 1.5-2.0 km altitude. Comparing the retrieval to co-located CALIPSO data in Figure 3.6 (blue markers), there are aerosols observed up to 4 km altitude, possibly in a multi-layered structure. Based on the CALIPSO observations and the modeled height of the atmospheric boundary layer, the retrieved ALH seems to be biased low in the atmosphere, thus too close to the surface. These results are summarized in Table 3.5.

Applying the dynamic scaling method to the same scenario, we observe an increase in

Table 3.5: Retrieval results from GOME-2 experiments. Columns marked with A, B, C and D are mean retrieved z_{aer} (in km), standard deviation of retrieved z_{aer} (in km), mean fitted τ and standard deviation of the fitted τ, respectively. n_{total} represents the total number of pixels in the scene, and n_{ret} represents the number of retrieved pixels. A_s avg represents the average surface albedo of the scene.

case	n_{tot}	A_s	formal approach					dynamic scaling method				
			n_{ret}	A	B	C	D	n_{ret}	A	B	C	D
A	85	0.19	49	0.5	0.15	5.34	1.87	78	1.37	0.37	4.82	2.04
B	206	0.15	161	2.66	1.85	2.31	1.69	173	3.35	1.75	2.22	1.83

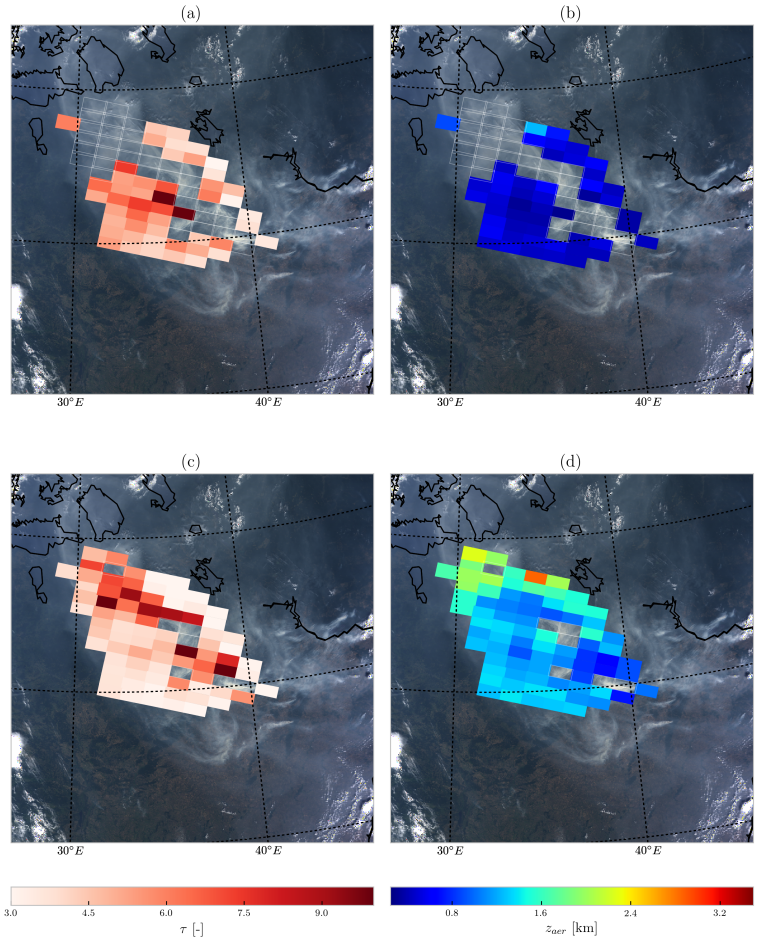

Figure 3.4: Results from processing 85 GOME-2A pixels over Russia on the 8th of August, 2010 using the formal approach and the dynamic scaling method. Empty GOME-2A pixels with a white border represent non-convergences. **(a)** Fitted τ at 760 nm from the formal approach. **(b)** Retrieved z_{aer} from the formal approach. **(c)** Fitted τ at 760 nm from the dynamic scaling method. **(d)** Retrieved z_{aer} from the dynamic scaling method. The background image for all plots is a subset of the MODIS Terra image in Figure 3.3a.

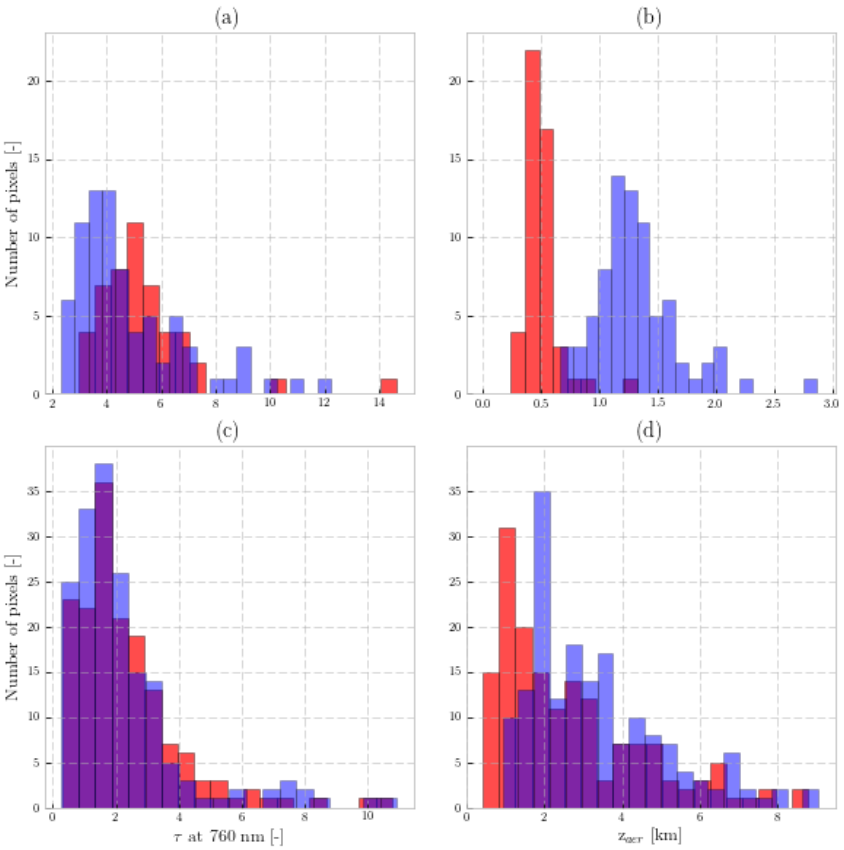

Figure 3.5: Histograms of fitted aerosol optical thickness (τ, left column) and aerosol layer height (z_{aer}, right column) from GOME-2A and GOME-2B pixels. Histograms in red are retrievals from the formal approach and the histograms in blue are results from the dynamic scaling method. **(a)** Fitted τ from the GOME-2A pixels over the August 8, 2010 wildfires plume over Russian. **(b)** Retrieved z_{aer} from the GOME-2A pixels over the August 8, 2010 wildfires plume over Russian. **(c)** Fitted τ from the GOME-2B pixels over the October 17, 2017 wildfires plume over Western Europe. **(d)** Retrieved z_{aer} from the GOME-2B pixels over the October 17, 2017 wildfires plume over Western Europe. The axes are adjusted for each plot.

the number of convergences to 78 pixels out of the 85 chosen (60% increase compared to the formal approach), as shown in Figure 3.4 (c and d). The fitted aerosol optical thickness is approximately 4.82, with a standard deviation of 2.04 (Figure 3.5a, blue histogram). While these fitted AOT values are still high to the scene, the spatial distribution is consistent with the biomass burning plume seen by MODIS (Figure 3.4c). The retrieved aerosol layer height is, on average, 1.37 km, with a standard deviation of 0.367 km (Figure 3.5b, blue histogram). Looking at CALIPSO data, this value appears to be more realistic for the biomass burning plume (Figure 3.6, black markers), as the aerosol particles are located farther away from the surface.

3.5.2 Portugal fire plume over Western Europe on October 17, 2017

The October 2017 Portugal wildfires began in the third week of October. On the 16th of October, the hurricane Ophelia made landfall over Ireland as a mid-latitude cyclone. Due to the cyclonic conditions the forest fire aerosol plumes were pulled from Portugal into Western Europe along with Saharan desert dust [2], which was observed the next day (Figure 3.3b). The aerosol plume from these fires are different from the aerosol plumes observed with the 2010 Russian wildfires case, primarily because the region of our interest is farther away from the fires; the plume over Western Europe appears to be more homogeneous. The GOME-2B overpass on the 17^{th} October, 2017, is approximately around 09:30 UTC, and the MODIS image in Figure 3.3b is approximately around 11:00 UTC. Although some of these GOME-2B pixels may be cloud-contaminated, our retrieval assumes cloud-free conditions. This assumption can result in large values in retrieved aerosol heights and fitted optical thicknesses. 206 GOME-2B pixels are chosen for this study. On average, the LER of this scene from the 2017 fires is 0.15 at 760 nm, whereas the same for the 2010 fires is 0.19, see Table 3.5.

Out of the 206 pixels, 161 pixels converge to a solution from the formal approach (Figure 3.7 a, b). The fitted τ at 760 nm is on average 2.31, with a standard deviation of 1.69 (Figure 3.5c, red histogram). Typical fitted τ over the plume seems to be around 3.0, which is too high of a value for this case since it disagrees with AERONET measurements, which show AOT values approximately between 2.0 and 1.0 at 675 nm and 870 nm over Lille during the GOME-2B overpass time. The retrieved z_{aer} is, on average, approximately 2.66 km from the ground with a standard deviation of 1.85 km (Figure 3.5d, red histogram). Many of the pixels that do not converge seem to be cloudy (the bottom corner of the GOME-2B pixels, Figure 3.7a). The dynamic scaling method increases the number of convergences to 173 pixels (Figure 3.7 c, d). On average, this method retrieves an aerosol layer height of 3.35 km, with a standard deviation of 1.75 km (Figure 3.5d, blue histogram). The average aerosol optical thickness at 760 nm fitted is 2.22 with a standard deviation of 1.83 (Figure 3.5c, blue histogram).

Comparing the retrieved z_{aer} is to profiles from a ground-based ceilometer in De Bilt, Netherlands (Figure 3.8a, black profile), the first observation is that the dynamic scaling method seems to retrieve a height that is more representative of the top of the aerosol layer, whereas the formal approach retrieves a more realistic aerosol height that is more-or-less the mid of the elevated layer's profile. It is, however, important to note that pulses from ceilometers are weak and tend to get attenuated beyond the bottom of the aerosol layer.

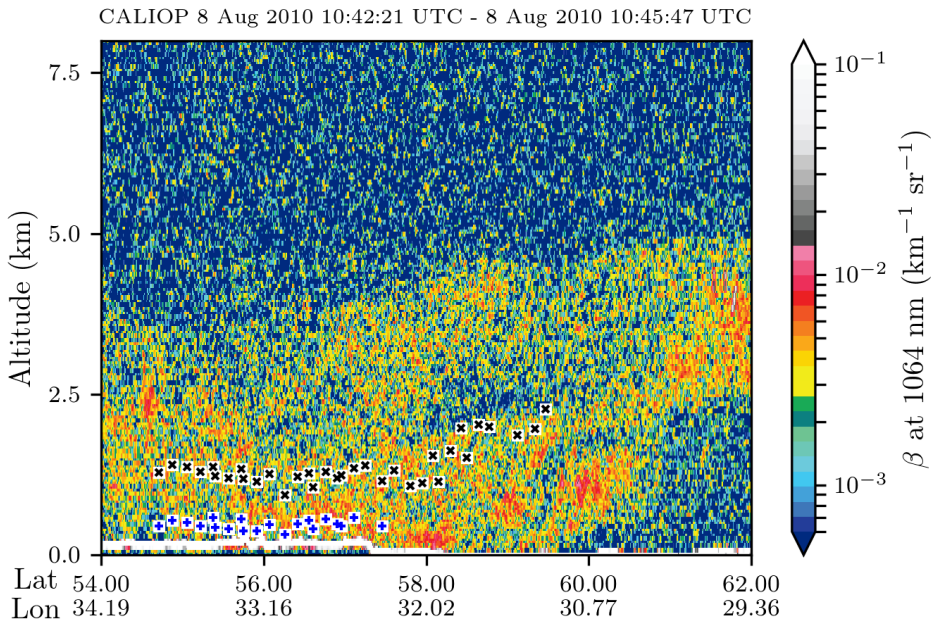

Figure 3.6: GOME-2A derived aerosol layer heights colocated within 100 km to the CALIPSO ground track (using great circle distance), plotted over attenuated backscatter (β) of the CALIOP lidar at 1064 nm. The blue and black markers in white squares represent converged ALH from the formal approach and the dynamic scaling method, respectively.

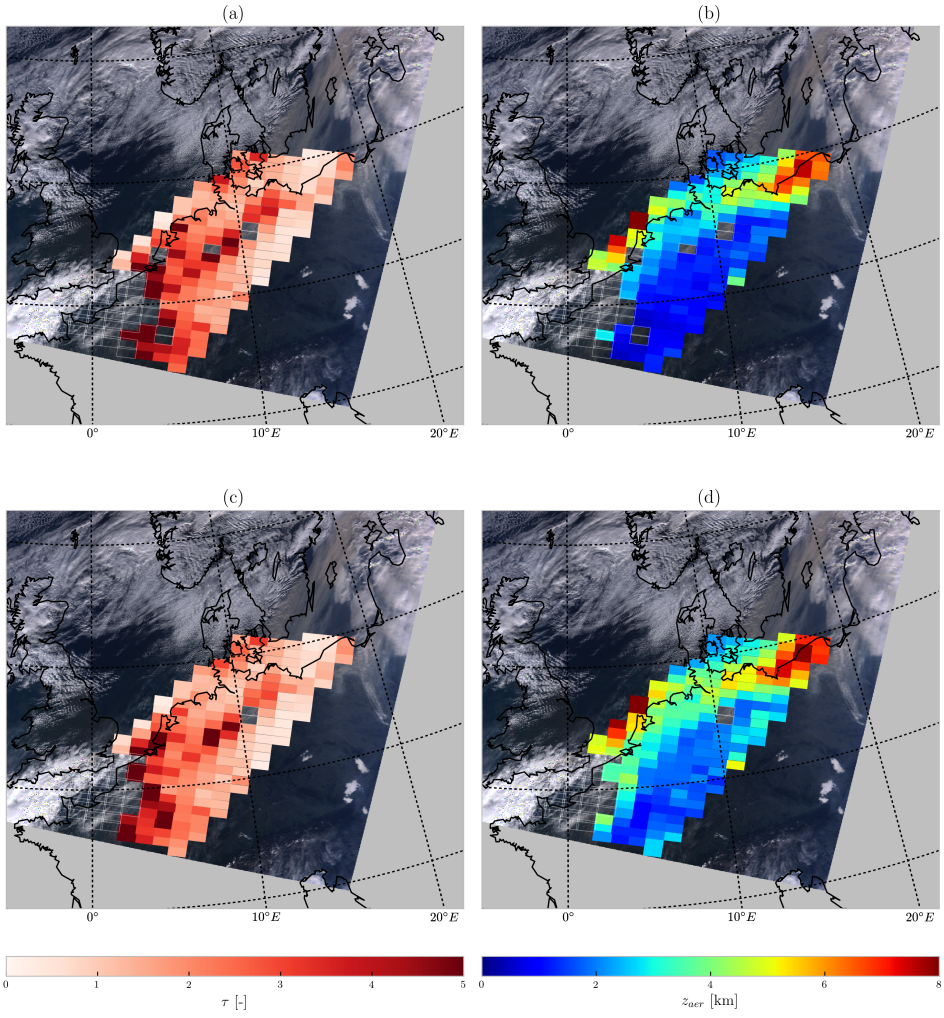

Figure 3.7: Results from processing 206 GOME-2B pixels over Western Europe using the formal approach and the dynamic scaling method. Empty GOME-2B pixels with a white border represent non-convergences. **(a)** Fitted τ at 760 nm from the formal approach. **(b)** Retrieved z_{aer} from the formal approach. **(c)** Fitted τ at 760 nm from the dynamic scaling method. **(d)** Retrieved z_{aer} from the dynamic scaling method. The background image is a subset of the MODIS Terra image in Figure 3.3b.

Because of this, layers above these can appear as weak backscatterers even though they may not be. A radiosonde profile of the relative humidity reveals the presence of an atmospheric layer that extends well beyond the altitude range from where the lidar backscatter becomes progressively weaker. This profile also shows the presence of a layer at the 200 - 400 hPa pressure levels, coinciding with a weak attenuated backscattered signal observed by the ceilometer in the same atmospheric level. A look into back trajectories, calculated using the TRAJKS model described in Stohl et al. [22], shows that the pressure levels between 800 hPa to 600 hPa (at De Bilt) likely contains aerosols carried from Portugal to De Bilt (Figure 3.8b). The back trajectory of air mass at 250 hPa also passes through this peninsula, but may not contain biomass burning aerosols since the layer at this atmospheric level does not mix with the lower level (according to the TRAJKS calculations). Following this, we have compared the retrieved z_{aer} from both methods to backscatter profiles from other ceilometer stations, reported in Figure 3.9. In general, while both the dynamic scaling method and the formal approach retrieve z_{aer} values that fall within the aerosol plumes, the dynamic scaling method retrieves heights that are slightly higher. This has to do with our conclusions from Figure 3.8.

The LER of a scene tells us which surface is brighter. In this case, the surface in the 2010 Russian fires was brighter than the same in the 2017 Western Europe case. The values of the modifying vectors $\boldsymbol{M}_{\mathrm{A_s/z_{aer}}}$ and $\boldsymbol{M}_{\mathrm{A_s}/\tau}$ over the two different scenes, however, can tell us the influence of the surface on the measurements itself, since these parameters are a direct comparison of the sensitivity of the measurement to aerosol properties and surface albedo. On average, $\boldsymbol{M}_{\mathrm{A_s/z_{aer}}}$ and $\boldsymbol{M}_{\mathrm{A_s}/\tau}$ in the 2010 Russian wildfires case are much larger in comparison to the same for the 2017 Portugal fire plume over Western Europe (Figure 3.10). This suggests that backscatter from the surface for the 2010 Russian wildfires case plays a bigger role in the measurements observed by the GOME-2 instrument. The dynamic scaling method is, hence, effectively able to apply a wavelength-dependent scaling of the SNR by relying on scene-dependent parameters. If the modifying vector $\boldsymbol{M}_{\mathrm{A_s}/\tau}$ is very low, aerosol properties retrieved from the dynamic scaling method will be approximately equal to the same from the formal approach. This is an example of the robustness of the method — the SNR should only be scaled when there is a need for it to be scaled.

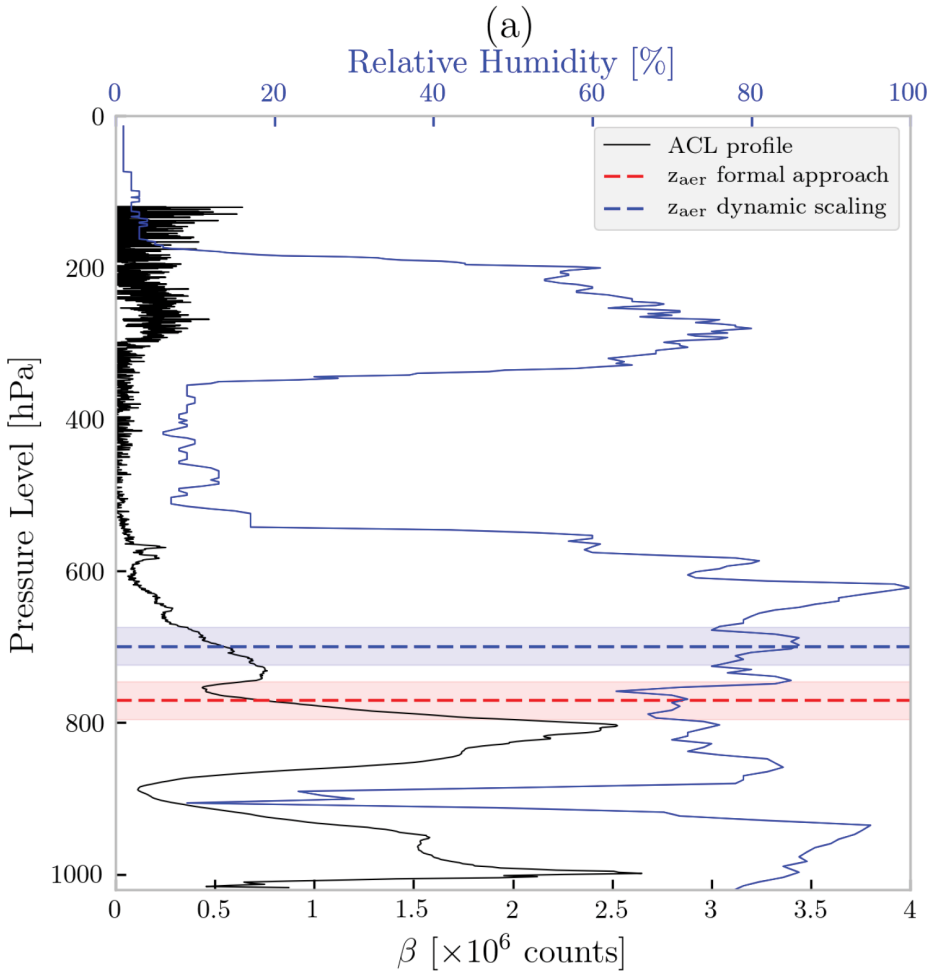
(a)
Relative Humidity [%]
0
20
40
60
80
100
ACL profile
z_{aer} formal approach
z_{aer} dynamic scaling
Pressure Level [hPa]
200
400
600
800
1000
0
0.5
1
1.5
2
2.5
3
3.5
4
β [$\times 10^6$ counts]

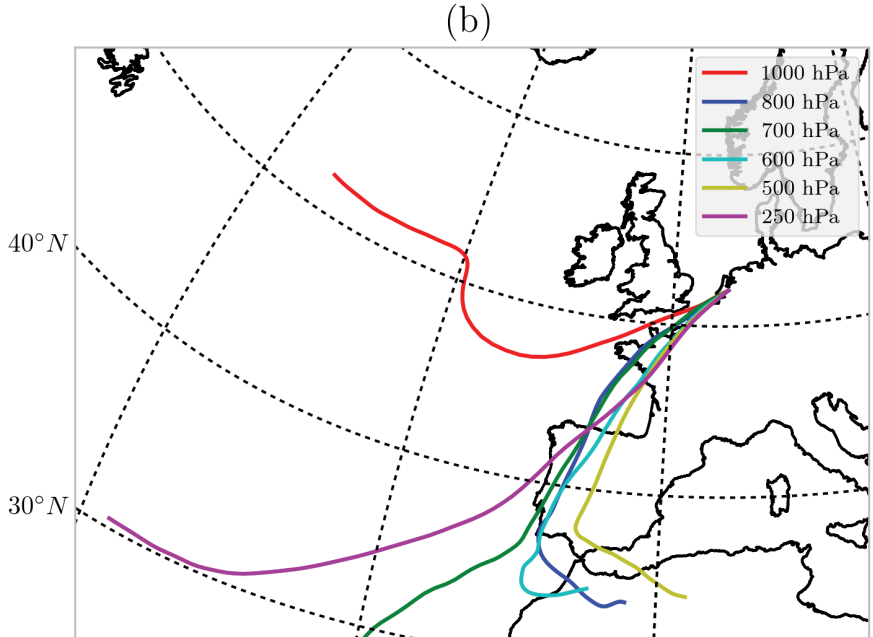
(b)
1000 hPa
800 hPa
700 hPa
600 hPa
500 hPa
250 hPa
40°N
30°N

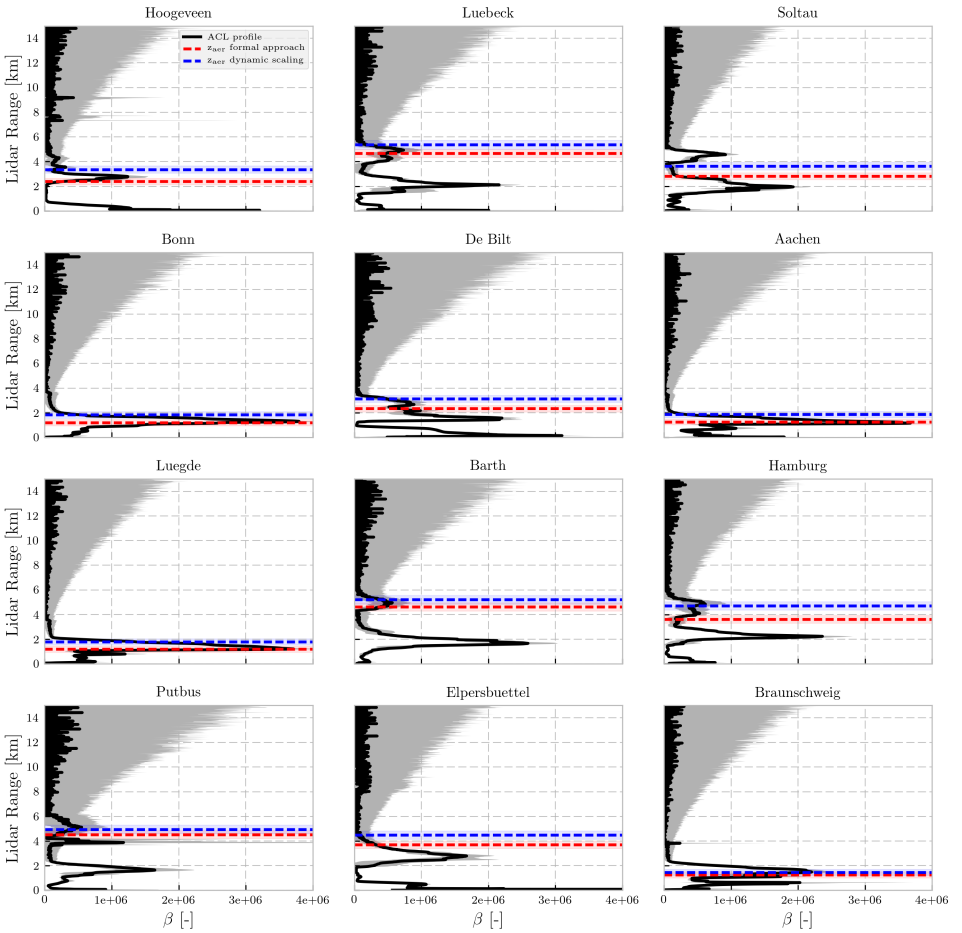

Figure 3.9: Validation of the retrieved aerosol layer height over Western Europe from ceilometers located in Netherlands and Germany from the CEILONET and DWD network. The black lines represent averaged ceilometer profiles of acquisitions 1 hour before and after the GOME-2B overpass over each location (600 profiles). The profiles are uncalibrated raw attenuated backscatter β as a function of lidar range (in km). The gray shaded region represents the standard deviation of the profiles used to create the averaged profile. The red and blue dashed line represents retrieved aerosol layer height using the formal approach and the dynamic scaling method, respectively. The red and blue shaded boxes represent the aerosol layer from the respective retrieval methods.

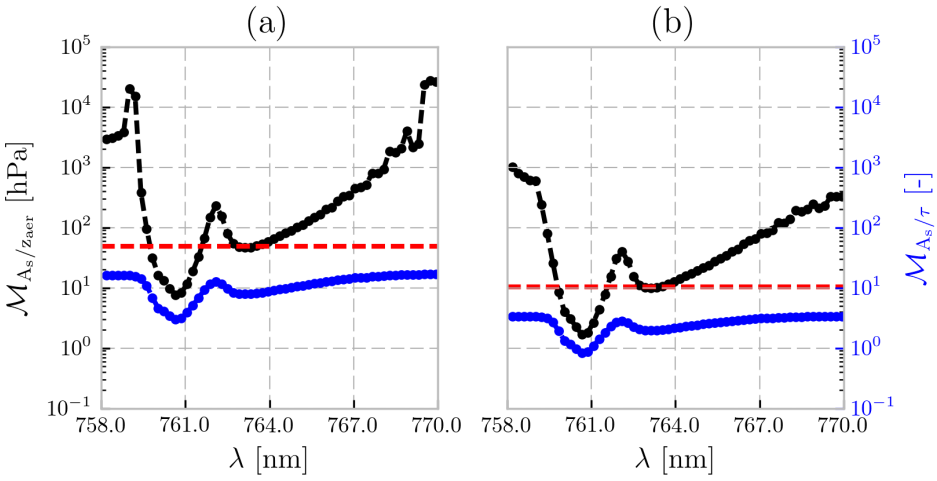

Figure 3.10: A comparison of the calculated matrices in the dynamic scaling method for all chosen GOME-2 pixels as a function of wavelength calculated for **(a)** the 2010 Russian wildfires, and **(b)** the 2017 Portugal wildfires. The black dotted line is the averaged modifying vector $\boldsymbol{M}_{A_s/z_{aer}}$ (Equation 3.2) and the blue line is the averaged modifying vector $\boldsymbol{M}_{A_s/\tau}$ (Equation 3.4) for all GOME-2 pixels chosen in each scene. The y-axis on the left is the range of values for $\boldsymbol{M}_{A_s/z_{aer}}$, and the same on the right is for $\boldsymbol{M}_{A_s/\tau}$. The red line is the averaged modifying threshold T, which is set at the 20^{th} percentile of $\boldsymbol{M}_{A_s/z_{aer}}$.

3.6 Conclusion

Inversion algorithms that retrieve aerosol properties from spectral measurements in the oxygen A band (between 758 nm and 770 nm) can face a lot of trouble over land. This is primarily because of the location of oxygen A band band beyond the red-edge, a wavelength region with diminishing ability of vegetation to absorb solar radiation as wavelength increases. This is especially the case when retrieving aerosol layer height using optimal estimation and radiative transfer models, as observed from Nanda et al. [14], Sanders and de Haan [19], and Sanders et al. [20].

The optimal estimation framework, an application of the weighted least squares technique, is designed to rank data points (in this case, spectral points in the measured TOA radiance and solar irradiance) higher when the SNR is higher, in order to reduce the influence of measurement error in the final retrieved solution. In the oxygen A band, these spectral points coincide with weak oxygen absorption cross sections, since low absorption equates to a high number of photons that can traverse through the atmospheric medium. Over oceans, due to its low albedo the number of photons that travel back from the surface are few. The signal recorded by satellites from an ocean scene, hence, predominantly arise from scattering and absorption by atmospheric species (in this case, aerosols). Over land, however, the number of photons that travel back from the surface increases dramatically. Due to this, the optimal estimation framework ranks spectral points representing photons that have traveled back from the surface higher than the same from aerosol layers. This is the primary error source when it comes to biases in aerosol retrievals from oxygen A band measurements over land.

This chapter introduces the dynamic scaling method, which is designed to retrieve

aerosol layer height over bright surfaces from oxygen A band measurements. The core principle of this proposed improvement is the wavelength-dependent modification of the measurement error covariance matrix by the subsequent wavelength-dependent modification of the signal-to-noise ratio of the measured spectrum, in order to reduce its preference towards photons that interact with the surface. The modification uses the scene-dependent Jacobian matrix, which makes it robust. The dynamic scaling method is compared with formal optimal estimation approach by retrieving aerosol layer height and aerosol optical thickness from synthetically generated spectra with randomly varied model parameters and model errors (that is, the forward models for simulation and retrieval have different model parameters). The results from the synthetic experiments generally favor the dynamic scaling method, which shows a significant improvement of the accuracy of retrieved aerosol layer height in the presence of errors in the assumed aerosol geometric thickness and the surface albedo (up to 10% relative errors) in the model.

The dynamic scaling method is also demonstrated for real spectra by using GOME-2A and GOME-2B oxygen A band measurements of two separate wildfire incidences in Europe, one being the 8^{th} of August, 2010 Russian wildfires and the other being the more-recent 17^{th} of October, 2017 Portugal wildfires. In the case of the 2010 Russian wildfires, the formal optimal estimation retrieval approach produces few convergences, and misses out the primary biomass burning aerosol plume (as observed from a MODIS Terra image). The fitted aerosol optical thickness are unrealistically high and spatially inconsistent with the aerosol plume observed by MODIS Terra. Co-located CALIOP lidar profiles show that the retrieved aerosol layer height is biased low in the atmosphere, closer to the surface. The dynamic scaling method, on the other hand, increases the number of converged pixels by 60% in comparison to the formal approach. The fitted aerosol optical thickness is still too high, but the spatial distribution of the aerosol optical thickness, as compared to same observed in the MODIS Terra image, is consistent. The retrieved aerosol layer heights are also more realistic, as they are positioned close to the centroid of the CALIOP backscatter profile describing aerosols. For the Portugal wildfire plume in the 17^{th} of October, 2017 over Western Europe, the dynamic scaling method does not increase the number of convergences significantly. The dynamic scaling method retrieves aerosol layer heights that are only slightly higher, and fits aerosol optical thicknesses at values are slightly lower in comparison to the same from the formal approach. The retrieved heights from both method are compared to lidar profiles from the EUMETNET ACL network of ceilometers. The comparison shows that both methods retrieved heights that are within the profiles that could be associated with aerosol layers. Analyzing a radiosonde profile of the relative humidity and calculated back trajectories, it is observed that the ceilometer profiles miss higher aerosol layers due to attenuation of the signal at lower atmospheric levels. This explains why the retrieved heights from the dynamic scaling method are slightly higher than the same from the formal approach.

In general, the dynamic scaling method improves the number of converged pixels. Between the two discussed cases, the dynamic scaling method provides a better improvement in the 2010 Russian wildfires case. This is primarily because the method is scene dependent. An important driver that determines the improvement of retrievals is the level to which the surface influences the TOA reflectance, which is jointly influenced by two parameters — the surface albedo and the aerosol optical thickness. The average surface albedo of the

scene for the 2010 Russian wildfires case was observed to be brighter than the same for the 2017 Portugal wildfires case. This is a possible explanation for the differences in the performance of the dynamic scaling method for the two cases.

The fitted aerosol optical thickness is systematically lower for the dynamic scaling method in comparison to the formal approach. A part of this can be attributed to the reduction of influence of spectral points in the measurement with a larger influence from the surface albedo. While this is expected, the method does not necessarily make the fitted aerosol optical thickness more realistic. It may well be the influence of assumptions in aerosol properties such as aerosol single scattering albedo and the phase function. It could, however, also be that the method does not fully remove the influence of surface in the measured top-of-atmosphere reflectance signal. In any case, the dynamic scaling method improves the representativity of the fitted aerosol optical thickness of the MODIS Terra observed smoke plume.

While the dynamic scaling may improve the the outcome of a retrieval attempt, it definitely places a burden on the operational algorithm — there are now more pixels for the operational algorithm to go through, which means more iterations in the optimal estimation method. Each iteration requires significant computational time, owing to the fact that the radiative transfer model computes the top-of-atmosphere reflectance in a line-by-line fashion. This is a problem that must be addressed. The following chapter (Chapter 4) provides an alternative approach to line-by-line calculations in an operational environment.

References

[1] Alexander, H., Maxime, H., Myles, T., Jean-Luc, L., Martial, H., Volker, L., team, E.-P., and team, T. (2016). The E-PROFILE network for the operational measurement of wind and aerosol profiles over Europe. In *Instruments and Observing Methods*, volume 125, Madrid, Spain. World Meteorological Organization.

[2] CAMS (2017). Saharan dust and smoke over France and UK.

[3] Corradini, S. and Cervino, M. (2006). Aerosol extinction coefficient profile retrieval in the oxygen A-band considering multiple scattering atmosphere. Test case: SCIAMACHY nadir simulated measurements. *Journal of Quantitative Spectroscopy and Radiative Transfer*, 97(3):354–380.

[4] de Haan, J. F., Bosma, P. B., and Hovenier, J. W. (1987). The adding method for multiple scattering calculations of polarized light. *Astronomy and Astrophysics*, 183.

[5] Dee, D. P., Uppala, S. M., Simmons, A. J., Berrisford, P., Poli, P., Kobayashi, S., Andrae, U., Balmaseda, M. A., Balsamo, G., Bauer, P., Bechtold, P., Beljaars, A. C. M., van de Berg, L., Bidlot, J., Bormann, N., Delsol, C., Dragani, R., Fuentes, M., Geer, A. J., Haimberger, L., Healy, S. B., Hersbach, H., Hólm, E. V., Isaksen, L., Kållberg, P., Köhler, M., Matricardi, M., McNally, A. P., Monge-Sanz, B. M., Morcrette, J.-J., Park, B.-K., Peubey, C., de Rosnay, P., Tavolato, C., Thépaut, J.-N., and Vitart, F. (2011). The ERA-Interim reanalysis: configuration and performance of the data assimilation system. *Quarterly Journal of the Royal Meteorological Society*, 137(656):553–597.

[6] EUMETSAT (2014). GOME-2 Level 1: Product Generation specification.

[7] Frankenberg, C., Hasekamp, O., O'Dell, C., Sanghavi, S., Butz, A., and Worden, J. (2012). Aerosol information content analysis of multi-angle high spectral resolution measurements and its benefit for high accuracy greenhouse gas retrievals. *Atmos. Meas. Tech.*, 5(7):1809–1821.

[8] Gabella, M., Kisselev, V., and Perona, G. (1999). Retrieval of aerosol profile variations from reflected radiation in the oxygen absorption A band. *Applied Optics*, 38(15):3190–3195.

[9] Henyey, L. C. and Greenstein, J. L. (1941). Diffuse radiation in the Galaxy. *The Astrophysical Journal*, 93:70.

[10] Hollstein, A. and Fischer, J. (2014). Retrieving aerosol height from the oxygen A band: a fast forward operator and sensitivity study concerning spectral resolution, instrumental noise, and surface inhomogeneity. *Atmospheric Measurement Techniques*, 7(5):1429–1441.

[11] Ingmann, P., Veihelmann, B., Langen, J., Lamarre, D., Stark, H., and Courrèges-Lacoste, G. B. (2012). Requirements for the GMES Atmosphere Service and ESA's implementation concept: Sentinels-4/-5 and -5p. *Remote Sensing of Environment*, 120:58–69.

[12] Min, Q. and Harrison, L. C. (2004). Retrieval of Atmospheric Optical Depth Profiles from Downward-Looking High-Resolution O2 A-Band Measurements: Optically Thin Conditions. *Journal of the Atmospheric Sciences*, 61(20):2469–2477.

[13] Munro, R., Lang, R., Klaes, D., Poli, G., Retscher, C., Lindstrot, R., Huckle, R., Lacan, A., Grzegorski, M., Holdak, A., Kokhanovsky, A., Livschitz, J., and Eisinger, M. (2016). The GOME-2 instrument on the Metop series of satellites: instrument design, calibration, and level 1 data processing – an overview. *Atmospheric Measurement Techniques*, 9(3):1279–1301.

[14] Nanda, S., de Graaf, M., Sneep, M., de Haan, J. F., Stammes, P., Sanders, A. F. J., Tuinder, O., Veefkind, J. P., and Levelt, P. F. (2018). Error sources in the retrieval of aerosol information over bright surfaces from satellite measurements in the oxygen A band. *Atmos. Meas. Tech.*, 11(1):161–175.

[15] Pelletier, B., Frouin, R., and Dubuisson, P. (2008). Retrieval of the aerosol vertical distribution from atmospheric radiance. volume 7150, page 71501R. International Society for Optics and Photonics.

[16] Péré, J. C., Bessagnet, B., Mallet, M., Waquet, F., Chiapello, I., Minvielle, F., Pont, V., and Menut, L. (2014). Direct radiative effect of the Russian wildfires and its impact on air temperature and atmospheric dynamics during August 2010. *Atmospheric Chemistry and Physics*, 14(4):1999–2013.

[17] Rodgers, C. D. (2000). *Inverse methods for atmospheric sounding: theory and practice*, volume 2. World Scientific.

[18] Sanders, A. F. J. and de Haan, J. F. (2013). Retrieval of aerosol parameters from the oxygen A band in the presence of chlorophyll fluorescence. *Atmospheric Measurement Techniques*, 6(10):2725–2740.

[19] Sanders, A. F. J. and de Haan, J. F. (2016). TROPOMI ATBD of the Aerosol Layer Height product.

[20] Sanders, A. F. J., de Haan, J. F., Sneep, M., Apituley, A., Stammes, P., Vieitez, M. O., Tilstra, L. G., Tuinder, O. N. E., Koning, C. E., and Veefkind, J. P. (2015). Evaluation of the operational Aerosol Layer Height retrieval algorithm for Sentinel-5 Precursor: application to Oxygen A band observations from GOME-2A. *Atmospheric Measurement Techniques*, 8(11):4947–4977.

[21] Sanghavi, S., Martonchik, J. V., Landgraf, J., and Platt, U. (2012). Retrieval of the optical depth and vertical distribution of particulate scatterers in the atmosphere using O_2 A- and B-band SCIAMACHY observations over Kanpur: a case study. *Atmospheric Measurement Techniques*, 5(5):1099–1119.

[22] Stohl, A., Haimberger, L., Scheele, M. P., and Wernli, H. (2001). An intercomparison of results from three trajectory models. *Meteorological Applications*, 8(2):127–135.

[23] Tilstra, L. G., Tuinder, O. N. E., Wang, P., and Stammes, P. (2017). Surface reflectivity climatologies from UV to NIR determined from Earth observations by GOME-2 and SCIAMACHY: GOME-2 and SCIAMACHY surface reflectivity climatologies. *Journal of Geophysical Research: Atmospheres*.

[24] Tran, H., Boulet, C., and Hartmann, J.-M. (2006). Line mixing and collision-induced absorption by oxygen in the A band: Laboratory measurements, model, and tools for atmospheric spectra computations. *Journal of Geophysical Research*, 111(D15).

[25] Tran, H. and Hartmann, J.-M. (2008). An improved O2 A band absorption model and its consequences for retrievals of photon paths and surface pressures. *Journal of Geophysical Research: Atmospheres*, 113(D18):D18104.

[26] Veefkind, J. P., Aben, I., McMullan, K., Förster, H., de Vries, J., Otter, G., Claas, J., Eskes, H. J., de Haan, J. F., Kleipool, Q., van Weele, M., Hasekamp, O., Hoogeveen, R., Landgraf, J., Snel, R., Tol, P., Ingmann, P., Voors, R., Kruizinga, B., Vink, R., Visser, H., and Levelt, P. F. (2012). TROPOMI on the ESA Sentinel-5 Precursor: A GMES mission for global observations of the atmospheric composition for climate, air quality and ozone layer applications. *Remote Sensing of Environment*, 120:70–83.

[27] Wang, P., Tuinder, O. N. E., Tilstra, L. G., de Graaf, M., and Stammes, P. (2012). Interpretation of FRESCO cloud retrievals in case of absorbing aerosol events. *Atmospheric Chemistry and Physics*, 12(19):9057–9077.

4

Speeding up the forward modeling: an approach to make the retrievals operationally more feasible

For a retrieval algorithm to be operationally feasible, there are certain requirements that need to be met. For instance, the retrieval algorithm must be able to process an entire granule of data telemetered down by the satellite to the ground station before the next telemetry instance. This means processing spectral data for a very large (sometimes millions) of pixels, requiring significant of computational time and resources. It is to the benefit of a retrieval algorithm to be fast and diligent in its processing of real-time satellite data.

In the case of the aerosol layer height retrieval algorithm discussed thus far, line-by-line radiative transfer calculations require several minutes in order to process a single pixel, with little certainty on whether retrieving aerosol layer height from a certain pixel will lead to a converged solution or diverge to no solution at all. This cripples the retrieval product, which is forced to process a subset of the data instead of all of the data. The bottleneck is the radiative transfer calculations itself, which require almost a minute for computing top-of-atmosphere reflectance spectra in the oxygen A-band. This chapter proposes a neural network modeling of the line-by-line radiative transfer model, and applies it to real data to show that the current algorithm can be made operationally feasible. The research goal of this chapter is,

Describe a strategy that exploits artificial neural networks to reduce the number of computations required by the forward model.[1]

[1]This chapter is published in https://doi.org/10.5194/amt-12-6619-2019, 2019.

4.1 Introduction

Launched in October 13, 2017, The TROPOsperic Monitoring Instrument [37] on board the Sentinel-5 Precursor mission is the first of the satellite-based atmospheric composition monitoring instruments in the Sentinel mission of the European Space Agency. The aerosol layer height (ALH) retrieval algorithm [23, 24, 28, 30] is a part of TROPOMI's operational product suite, expected to be delivered near real time. The ALH (symbolised as z_{aer}) retrieval algorithm, operating within the near infrared region in the oxygen A-band between 758 nm - 770 nm, exploits information about heights of scattering layers derived from absorption of photons by molecular oxygen — the amount of absorption indicates whether the scattering layer is closer or farther from the surface; if the number of photons absorbed by oxygen is higher, it suggests a longer photon path length due to an aerosol layer present closer to the surface. This principle has been applied to cloud height algorithms such as FRESCO (Fast Retrieval Scheme for Clouds from the Oxygen A-band) by Wang et al. [38], which use look up tables for generating top of atmosphere (TOA) reflectances to compute cloud parameters. Since clouds are such efficient scatterers of light, FRESCO can approximate scattering by cloud using a Lambertian model — this simplification works for optically thick cloud layers quite well. For aerosol layers, however, such calculations need to be done in much greater detail due to their weaker scattering properties. TROPOMI's ALH algorithm employs the science code Disamar (Determining Instrument Specifications and Methods for Atmospheric Retrievals) that uses the Layer-Based Orders of Scattering (LABOS) radiative transfer model based on the doubling-adding method [8] that calculates reflectances at the TOA and its derivatives with respect to aerosol layer height and aerosol optical thickness (τ). These calculations are done line-by-line, requiring calculations at 3980 wavelengths to generate these TOA reflectances within the oxygen A-band. Having computed the TOA reflectance spectra, aerosol layer heights are retrieved with Optimal Estimation (OE), an iterative retrieval scheme developed by Rodgers [27] that incorporates a priori knowledge of retrieval parameters into their estimation. Such a retrieval scheme also provides a posteriori error estimations, which are important for assimilation models and diagnosing the retrieval results.

The ALH retrieval algorithm is computationally expensive, requiring several minutes to compute z_{aer} for a single ground pixel [30]. As near-real time processors need to consistently go through large volumes of data recorded by the satellite for the mission lifetime, the operational computation capability is much restricted for TROPOMI recording approximately 1.4 million pixels within a single orbit where, on average, 50,000 pixels are typically identified as aerosol contaminated pixels (with a UVAI value greater than 0.0) for retrieving aerosol layer height. This places a steep requirement on the computational infrastructure to process all possible pixels from a single orbit. The online radiative transfer model severely limits the ALH data product, processing only a small fraction of the total possible pixels within a single orbit while compromising the timeliness of the data delivery.

The bottleneck identified here is the large number of calculations that the forward model has to compute to retrieve information on weak scatterers such as aerosols. Several steps to circumvent this bottleneck exist, such as using correlated k-distribution method to reduce the number of calculations [14], using a look up table for calculating forward model outputs, or entirely foregoing the forward model and directly retrieving z_{aer} from observed spectra using neural networks [3, 4]. Studies by Sanders and de Haan [29] have

shown that the look up table for reflectance alone measure up to 46 GB in size, and perhaps similar or larger sizes for the derivatives. Chimot et al. [3] describe an approach using a radiative transfer model to generate slant column densities of the O_2-O_2 band at 477 nm from Ozone Monitoring Instrument (OMI) measurements for different aerosol optical depths (among other input parameters) to train several artificial neural network models that directly retrieve aerosol layer height. Operationally, their neural network models use the MODIS aerosol optical depth at 550 nm and retrieved OMI slant column densities, thereby entirely foregoing line-by-line calculations and significantly speeding up the retrieval algorithm. The trained neural network models directly retrieved aerosol layer heights from spectra measured by OMI on board the NASA Aura mission, without using line-by-line calculations or an iterative estimation step such as OE [4]. A similar example of retrievals is the ROCINN (Retrieval of Cloud Information using Neural Networks) cloud algorithm developed by Loyola [21] which uses neural networks to compute convolved reflectance spectra to retrieve cloud properties. These retrievals show the exploitable capabilities of artificial neural networks in the context of retrieving atmospheric properties from oxygen absorption bands.

The work of Chimot et al. [4] and Loyola et al. [20] bring to light the efficacy of artificial neural networks in satellite remote sensing of oxygen absorption bands for retrieving properties of scattering species in the atmosphere. This chapter discusses a method inspired by Chimot et al. [3] and Loyola [21] to retrieve aerosol layer height from oxygen A-band measurements by TROPOMI. While Chimot et al. [3] directly retrieve aerosol layer heights from their neural network models, the operational algorithm in this chapter utilises neural networks to calculate top-of-atmosphere radiances in the forward model. This is subsequently used by an optimal estimation scheme to retrieve aerosol layer heights. Similarly while Loyola [21] derive top-of-atmosphere sun-normalised radiances only for their cloud property retrieval algorithm, the method in this chapter has dedicated neural network models that calculate the Jacobian as well as the top-of-atmosphere sun-normalised radiances. By reducing the time consumed for calculating forward model outputs, computational efficiency of TROPOMI's aerosol layer height retrieval algorithm can be significantly improved.

Section 4.2 introduces the operational aerosol layer height algorithm and discusses the line-by-line forward model. The neural network forward model approach is detailed in section 4.3, and its verification on a test data set is discussed in same section. This approach is then applied to various test cases using synthetic and real TROPOMI spectra (section 4.4) before concluding in section 4.5.

4.2 The TROPOMI aerosol layer height retrieval algorithm

The TROPOMI aerosol layer height is one of the many algorithms that exploit vertical information of scattering aerosol species in the oxygen A-band [5–7, 10–13, 16, 24, 26, 28–31, 35, 39, 43, 44]. These methods invert a forward model that describes the atmosphere, to compute the height of the scattering layer. This section discusses the setup of the TROPOMI ALH retrieval algorithm, which consists of the inversion of a forward model representing the atmosphere using optimal estimation as the retrieval method, and a description of the

forward model.

4.2.1 The Disamar forward model and its many simplifications of atmospheric properties

Optimal estimation iteratively simulates TOA radiance spectra until the convergence of χ^2 (Equation **??**). For this, disamar computes reflectances at a high resolution wavelength grid. The computed high resolution reflectances are combined with a reference solar spectrum derived from Chance and Kurucz [2] to obtain a high resolution Earth radiance. The high resolution Earth radiance and the solar spectrum are convolved with the instrument spectral response function to obtain Earth radiance and solar irradiance spectrum in the instrument's wavelength grid, before finally computing the reflectance spectrum in the instrument grid using Equation **??**. It is important to note that the steps of including the reference solar spectrum to compute reflectances in the instrument's wavelength grid are not undertaken by the neural network algorithm. The neural network aerosol layer height retrieval algorithm directly convolves the reflectance. The difference between including an excluding a reference spectrum in the convolution process results in differences in the order of 4% to 5% around 762 nm and 766 nm. Further on in this chapter, a direct comparison between disamar retrievals of aerosol layer height and retrievals with the neural network algorithm is provided.

Reflectances are calculated by accounting for scattering and absorption of photons from their interactions with aerosols, the surface, and molecular species. Molecular scattering of photons in the oxygen A-band is described by Rayleigh scattering, and absorption is described by photon-induced magnetic dipole transition between $b^1\Sigma_g^+ \leftarrow X^3\Sigma_g^-(0,0)$ electric potential levels of molecular oxygen, and collision-induced absorption between O_2-O_2 and O_2-N_2. The total influence of the O_2 A-band on the TOA reflectance is described by its extinction cross-section, which is a sum of the three aforementioned contributions. As the vertical distribution of oxygen is exactly known, the extinction cross-section can be exploited to retrieve z_{aer} from satellite measurements of the oxygen A-band. For this, Disamar calculates absorption (or extinction) cross sections at 3980 wavelengths within the range 758 nm - 770 nm.

To reduce the number of calculations, various atmospheric properties are simplified. As the Rayleigh optical thickness is low at 760 nm, Disamar only computes the monochromatic component of light by calculating the first element of the Stoke's vector. The exclusion of higher order Stoke's vector elements of the radiation fields has not shown to be a significant source of error [29].

Calculating the influence of Rotational Raman Scattering (RRS) is also ignored, as it is a computationally expensive step. While this exclusion of RRS is not advised by literature [33, 36], preliminary experiments by Sanders and de Haan [29] have ascertained that the errors in the retrieved aerosol layer height resulting from ignoring RRS of the oxygen A-band in the forward model are significantly smaller than the effect of other model errors such as errors due to incorrect surface albedo. Therefore, RRS has been historically not simulated in the forward model of the KNMI aerosol layer height retrieval algorithm. The atmosphere is assumed cloud-free, which is a required simplification as the retrieval of z_{aer} in the presence of clouds is still challenging and thereby is performed only for pixels which are unlikely to contain clouds. Compared to totally cloud-free scenes, errors in

retrieved z_{aer} are large for cloud-free scenes containing undetected optically thin cirrus clouds [30]. The fraction of the pixel containing aerosols is assumed to be 100%, which further simplifies the representation of aerosols within the atmosphere.

Perhaps the largest simplification of the atmosphere lies in model's description of aerosols, assumed to be distributed in a homogeneous layer at a height z_{aer} with a 50 hPa thickness, a fixed aerosol optical thickness (τ) and a single scattering albedo (ω) of 0.95 (so, scattering aerosols). A Henyey-Greenstein model [15] with an asymmetry parameter g value of 0.7 is used to parameterize the aerosol scattering phase function, which is one of the widely used approximations. These fixed aerosol optical properties have been derived from AERONET data and tested by Sanders et al. [30], who retrieved z_{aer} from GOME-2 spectra to show that the algorithm is robust to fixing aerosol model parameters such as the single scattering albedo and the Henyey-Greenstein phase function asymmetry parameter. The surface is assumed to be an isotropic reflector with a brightness described by its Lambertian Equivalent Reflectivity (LER). This is also an important simplification, requiring less computations over other surface models such as a Bi-directional Reflectance Model. Although the forward model is capable of including sun-induced chlorophyll fluorescence into the retrieval, it is currently being considered for a future implementation of TROPOMI's operational ALH retrieval algorithm. Lastly, the atmosphere is spherically corrected for incoming solar radiation and remains plane-parallel for outgoing Earth radiance.

These simplifications in the Disamar forward model are a necessity for the line-by-line aerosol layer height algorithm, owing to its slow computational speed. The speed up of forward model simulation encourages increasing the complexity of simulation assumption.

4.2.2 Application to TROPOMI

TROPOMI's near infrared (NIR) spectrometer records data between 675 nm - 775 nm, spread across two bands — band 5 contains the oxygen B-band and band 6 the oxygen A-band. The spectral resolution, which is described by the full width at half maximum (FWHM) of the instrument spectral response function (ISRF), is 0.38 nm with a spectral sampling interval of 0.12 nm. The spatial resolution is around 7 km × 3.5 km for band 5 and 6. Initial observations from the TROPOMI NIR spectrometer show a signal to noise ratio (SNR) of 3000 in the continuum before the oxygen A-band. The instrument polarization sensitivity is reduced to below 0.5% by adopting the technology of the polarization scrambler of OMI [19, 37]. Disamar utilizes TROPOMI's swath-dependent ISRFs to convolve $I(\lambda)$ and $E_0(\lambda)$ into $I(\lambda_i)$ and $E_0(\lambda_i)$ in the instrument's spectral wavelength grid, after which the modeled reflectance is calculated using Equation **??**.

Input parameters required by the TROPOMI ALH retrieval algorithm encompass satellite observations of the radiance and the irradiance, solar-satellite geometry, and a host of atmospheric and surface parameters required for modeling the interactions of photons within the Earth's atmosphere (see Table 4.1). Meteorological parameters are taken from ECMWF (European Centre for Medium-range Weather Forecast), including the temperature-pressure profile at 91 atmospheric levels (of which the surface is a part). The various geophysical parameters are interpolated to TROPOMI's ground pixels using nearest neighbour interpolation.

TROPOMI incorporates information from the VIIRS instrument to detect the presence

of cirrus clouds in the measured scene (using a cirrus reflectance threshold of 0.01). This information is further combined with cloud fraction retrievals by the TROPOMI FRESCO algorithm (maximum cloud fraction of 0.6), and the difference between the scene albedo in the database in the UV band and the apparent scene albedo at the same wavelength calculated using a lookup table (if the difference is larger than 0.2, it suggests cloud contamination). A combination of these different cloud detection strategies results in the cloud_warning flag in the level-2 TROPOMI ALH product. In this chapter, however, we use a strict FRESCO cloud fraction filter of 0.2 alone to remove cloudy pixels.

Calculation of TOA reflectance and its derivatives with respect to z_{aer}, and τ in a line-by-line fashion takes approximately 40-60 seconds to complete on a computer equipped with Intel(R) Xeon(R) CPU E3-1275 v5 at a clock speed of 3.60 GHz. In an iterative framework such as the Gauss-Newton method, the retrieval of z_{aer} can take between 3-6 iterations depending on the amount of aerosol information available in the observed spectra, requiring several minutes to compute retrieval outputs for a specific scene. If these retrievals fail by not converging within the maximum number of iterations, the processor can waste up to 10 minutes on a pixel without retrieving a product. In order to compute Disamar's outputs quicker, a neural network implementation is discussed in the next section.

Table 4.1: Input parameters required for retrieving aerosol layer height using TROPOMI measured spectra.

Parameter	Source	Remarks
Radiance and irradiance	TROPOMI Level-1b product	
SNR measured spectrum	TROPOMI Level-1b product	
Geolocation parameters	TROPOMI Level-1b product	
Surface albedo	GOME-2 LER database	[34]
Meteorological parameters	ECMWF	17km horizontal resolution
Cloud fraction	TROPOMI Level-2 FRESCO product	
Absorbing aerosol index (AAI)	TROPOMI Level-2 AAI product	
Land-sea mask	NASA Toolkit	
Surface altitude	GMTED 2010	pre-averaged

4.3 The neural network (NN) forward model

4.3.1 Artificial Neural Networks

The history of neural networks began with a paper by McCulloch and Pitts [22] who theorised on how a brain neuron might work. This led eventually to Donald O. Hebb, who in his book Organization of Behaviour (published in 1949) explained that neural pathways are strengthened the more they are used [32]. While these contributions to science were entirely related to the biological neural network, computer scientists in the 1960s began to take interest in simulating neural networks. This led to the development of the first ever neural network called the perceptron by Bernard Widrow and Marcian Hoff from Stanford University called ADALINE [42], which was used to filter out echoes from telephone lines. Many years later, artificial neural networks are now an integral part of the modern day world, with a wide variety of applications including processing data at very high speeds for atmospheric remote sensing.

Artificial neural networks, as the name implies, is a network of individual processing units known as neurons or nodes (see Figure 4.1). Each node computes an output for certain inputs. The interaction of these individual processing units, also known as nodes (or neurons), enable the connecting network to map a set of inputs (also known as the input layer) to a set of outputs (or, the output layer) via layers of nodes between the input and output layers (called the hidden layers). The connections are known as weights whose value symbolises the strength of a connection between two nodes. Since the nodes connect inputs to the outputs, higher values in a set of connecting weights represent a stronger influence of a particular parameter in the input layer over a particular parameter in the output layer. The weights between two nodes are calculated by training the neural network to a data containing the neural network's input and output.

The training (or optimisation) of a neural network begins with a training data set containing many instances of input and output layer elements. Initially, the weights of the neural network are randomly generated. The output of the neural network is the amalgamation of the output of each individual node — these calculations are known as forward propagation. As true values of the output layer for a given set of inputs are exactly known in the training data set, the output of the neural network calculated after using randomised, non-optimised weights will result in an error between the expected and the computed neural network output. These biases are called prediction errors, an essential element in the optimization of the neural network weights.

The mean squared error (MSE) between the true output and the calculated output is also called the loss function (henceforth annotated as Δ), which is synonymous to a cost function (Equation 4.1),

$$\Delta = \frac{1}{n_\lambda} \sum_{\forall \lambda} (nn_\lambda - o_\lambda)^2 \tag{4.1}$$

where λ is the wavelength, n_λ represents the number of elements in the output layer, nn_λ represents the calculated output for wavelength via forward propagation, and o_λ are the outputs in the training data set. The optimisation of the neural network then aims to minimise the loss function Δ, which is a function of weights in the neural network. This is achieved by calculating the gradient of each weight w, which is the partial derivative $\partial\Delta/\partial w$ — the gradient computes the change in the loss function for a change in each weight. These

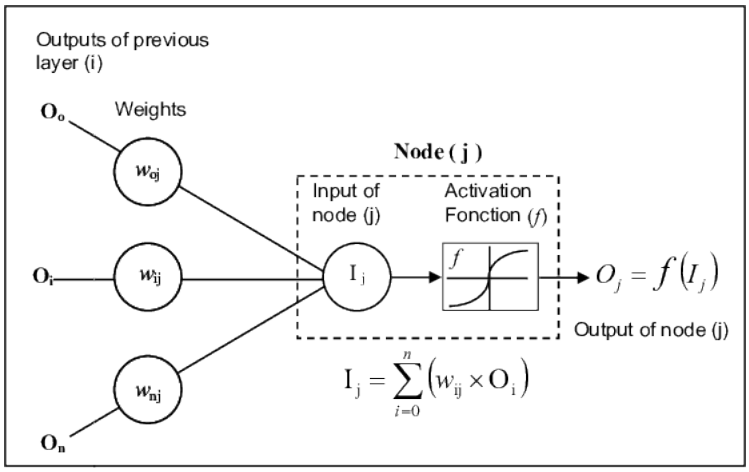

Figure 4.1: The basic element of an artificial neural network — the node (the element described in the box labelled node(*j*)). The input to a node is the output from a previous layer, either a hidden layer or the input layer, which is weight-summed using the weights between the previous layer element and the note *j*. The summation is then passed through an activation function f to calculate the output of the node *j*. Image derived from Chokmani, Karem Khalil, Bousnobra Ouarda, Taha Bourdages, Raymond. (2020). Estimation of River Ice Thickness Using Artificial Neural Networks.

gradients are then used by optimisers such as the ADAM optimiser (Adaptive Moment Estimation) by Kingma and Ba [17] to minimise Δ, in an iterative manner. The training of a neural network is concluded when the loss function is minimised until it cannot be minimised anymore for that specific neural network configuration.

4.3.2 The TROPOMI NN forward model for the ALH retrieval algorithm

The standard architecture of the NN-augmented operational aerosol layer height processor includes three neural network models for estimating top of atmosphere sun-normalised radiance, the derivative of the reflectance with respect to z_{aer}, and the same for τ. It is also possible to assign the neural network to compute the reflectance instead of the sun-normalized radiance — the results will not change. The definition of sun-normalised radiance used in this chapter is the ratio of Earth radiance to solar irradiance. Disamar calculates derivatives with respect to reflectance, which is the sun-normalised radiance multiplied by the ratio of π and cosine of solar zenith angle. All three neural network models share the same input model parameters. Optimising a single neural network model for all three forward model outputs is not necessary; the correlations between the input parameters and the different forward model outputs are different, which can complicate the optimisation of a general-purpose neural network. This chapter, however, acknowledges modern developments in neural network optimisation techniques that now afford selectively optimising a neural network for different tasks [18, 40].

The models are trained using the python Tensorflow module [1], and further implemented into an operational processor using C++ interface to Tensorflow. These neural network models require training data containing Disamar input and output parameters

and a connecting architecture that encompasses the input feature vector containing scene-varying model parameters, the number of hidden layers, number of nodes in each hidden layer, and an activation function that maps the input to the final output layer containing Disamar outputs. In Tensorflow, the derivative of Δ with respect to the weights are computed using reverse-mode automatic differentiation, which computes numerical values of derivatives without the use of analytical expressions [41].

The inputs for NN are referred together as the feature vector. The choice of the parameters included into the feature vector is a very important factor deciding the performance of the neural network. The primary classes of model parameters (relevant to retrieving z_{aer}) varying from scene to scene are solar-satellite geometry, aerosol parameters, meteorological parameters and surface parameters (Table 4.2). The various aerosol parameters that are fixed from scene to scene are the aerosol single scattering albedo (ω), the asymmetry factor of the phase function, and the angstrom exponent, as they are also fixed in the line-by-line operational aerosol layer height processor. The scattering phase function of aerosols is currently limited to a Henyey-Greenstein model with a fixed g value of 0.7 to mimic Disamar. Surface pressure as well as the temperature-pressure profile are two important meteorological parameters relevant to retrieving z_{aer}. A difference between Disamar and NN models is the definition of this temperature information in the input. Disamar requires the entire temperature-pressure profile of the atmosphere, whereas NN only uses the temperature at z_{aer}. Surface albedo is specified at 758 nm as well as 772 nm in Disamar, whereas it is only specified at 758 nm in the feature vector of NN. In general there is a greater scope to add detailed information in Disamar. However, Disamar has historically incorporated many simplifications in order to reduce computational time. The current NN model is developed with the aim to mimic Disamar as much as possible, without including additional state vector elements into the retrieval, such as chlorophyll fluorescence, aerosol optical properties, cloud properties, and so on.

4.3.3 Training the neural networks

Since the NN forward model is specifically designed for TROPOMI, the solar-satellite geometry is selected to represent TROPOMI orbits for the training data. Meteorological parameters for the locations associated with these solar-satellite geometries are derived from the 2017 60-layer ERA-Interim Reanalysis data [9], and aerosol and surface parameters are randomly generated within their physical boundaries. This training data generation strategy spans the entire set of TROPOMI solar and viewing angles as well as meteorological parameters.

Generally, the required training data size increases with increasing non-linearity between input and output layers in a neural network — there is no specific method to accurately determine the required sample size before training. The number of spectra generated for the training set was determined by training different models with different number of spectra in the training set ranging from 1,000 to 600,000. In general it was observed that incorporating more data resulted in a better neural network model. In order to test the trained neural network model, a choice of 500,000 spectra were selected. Finding the most optimal neural network configuration requires testing the trained neural network model. To that extent, the training data set was split into a training-testing split, where the model was trained on a majority of the training data set and tested on the remaining

Table 4.2: Scene-dependent input model parameters for the NN model. See also Figure 4.2 for a histogram of the input parameters. The solar-satellite geometry parameters are generated in combinations conforming to the ones encountered by TROPOMI's orbits.

Parameter class	Model Parameters	Remarks	limits
Geometry	Solar zenith angle (θ_0)	in feature vector	8.20° - 80.0°
	Viewing zenith angle (θ)	in feature vector	0.0° - 66.60°
	Solar azimuth angle (ϕ_0)	in feature vector	-180.0° - 180.0°
	Viewing azimuth angle (ϕ)	in feature vector	-180.0° - 180.0°
Aerosol parameters	Aerosol pixel fraction	fixed	1.0
	Single scattering albedo (ω)	fixed	0.95
	Aerosol optical thickness (τ)	in feature vector	0.05 - 5.0
	Aerosol layer height (z_{aer})	in feature vector	75 hPa - 1000.0 hPa
	Aerosol layer thickness (p_{thick})	varied but excluded from feature vector	50 hPa - 200 hPa
	Scattering phase function	fixed	Henyey-Greenstein
	asymmetry factor (g)	fixed	0.7
	Angstrom exponent (Å)	fixed	0.0
Meteorological parameters	Temperature	in feature vector	temperature at z_{aer}
Surface parameters	Surface pressure (p_s)	in feature vector	520 hPa - 1048.50 hPa
	Surface reflectance model	LER	
	Surface albedo (A_s)	in feature vector	2.08E-7 - 0.70

minority. Once trained, the model was tested again on a test data set with 100,000 scenes outside of the training data set. These spectra were generated using Disamar with model parameter ranges described in Table 4.2. Figure 4.2 plots the distribution of the input parameters necessary for training the neural network. The neural network model accepts solar azimuth and viewing azimuth angles separately, however they are plotted together as relative azimuth angle in Figure 4.2 to save space. The generation of this training data set is by far the most time consuming step since each Disamar run requires between 50-60 seconds to generate the synthetic spectra. Once the data has been generated, it is prepared for training the neural network models in NN. This is done by data normalisation, achieved by subtracting the mean of each of the training input and output parameters and dividing the difference by its standard deviation, which makes the learning process quicker by reducing the search space for the optimizer. The offset and scaling parameters are important, as the neural network computes outputs within this scaled range, which needs to be re-scaled back to physical values. This training requires a few hours on an Intel(R) Xeon(R) CPU E3-1275 v5 at a clock speed of 3.60 GHz.

The most optimal configurations for each of the three NN models are determined by the number of hidden layers, the number of nodes on each layer and the chosen activation function for which the discrepancy between the modeled output for specific inputs and the truth (derived from Disamar) is minimal. The difference between the outputs calculated by Disamar and NN for these three models provide insight on their performance.

In order to test the most optimal number of layers, the most optimal number of nodes per each layer and the activation function, several neural network configurations were trained for 250,000 iterations and their summed losses (defined as $\Delta \times n_\lambda$) were compared to find out which was the best configuration. Figure 4.3 plots the summed losses as a function of training iteration for different configurations.

To begin, with 50 nodes per each hidden layer, three neural networks for each of the three models were trained — one-layered, two-layered and three-layered. The neural network models performed best with at least two hidden layers (Figure 4.3a). For all three models, their two-layered versions show a similar summed loss to their three-layered alternatives, with the summed loss for the two-layered $\mathrm{NN}_{\mathrm{disamar}}(\mathrm{K}_\tau)$ showing more stability with training epoch. Therefore, a simpler two-layered architecture is chosen for all three models. Continuing on, three other architectures for each of the three models were chosen with 50, 100, and 200 nodes for each of the two hidden layers. The results that with more training steps, the choice of 100 nodes for each of the two layers has a compromise between summed training loss and simplicity (Figure 4.3b), especially for $\mathrm{NN}_{\mathrm{disamar}}(\mathrm{K}_\tau)$. Finally, going ahead with a two-layered and 100 nodes for each layer configuration, three activation functions namely the sigmoid function, the hyperbolic tangent function (tanh) and the rectified linear unit (relu) function were tested for each of the neural network models (Figure 4.3c). In this case, while all functions converge to similar summed loss values by 250,000 iterations, the sigmoid function has a good compromise between training loss and stability. Figure 4.4 gives a graphic representation of the neural network model.

The finalised configurations were then trained for one million iterations after which they were applied to the test data set to study prediction errors. Figure 4.5 plots the performance of each of the neural networks trained on the testing data set. An error analysis revealed that the trained neural networks were capable of calculating Disamar outputs with low

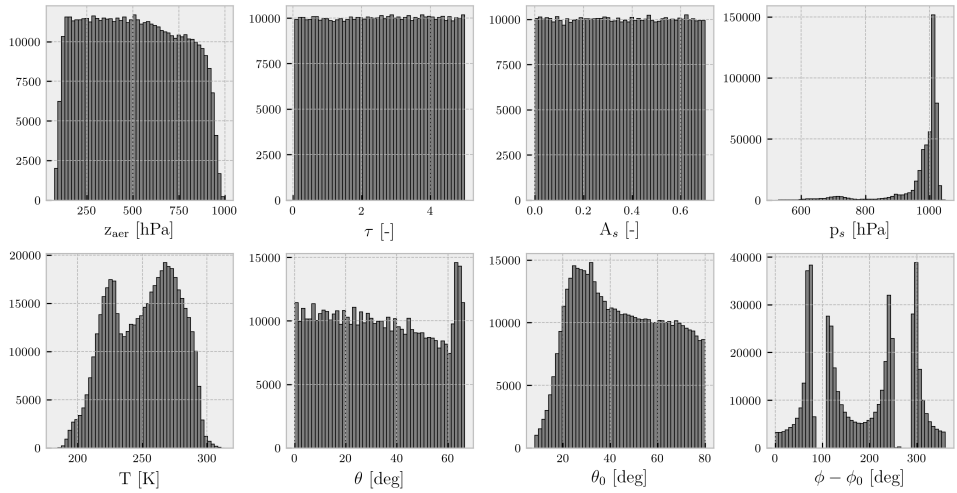

Figure 4.2: Histograms of the various input parameters for each of the neural network models in NN. Minimum and maximum values for each of the parameters are shown in Table 4.2.

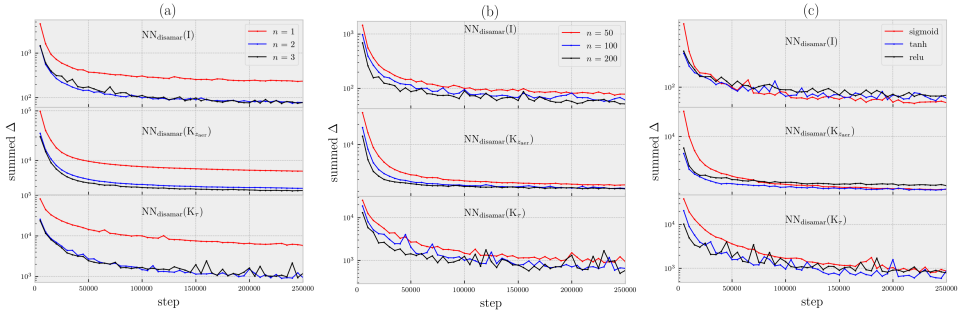

Figure 4.3: Summed loss as a function of training step for different neural network model configurations. **(a)** The neural network models have 50 nodes per each layer with a sigmoid activation function. **(b)** The neural network models have two hidden layers with each node activated by the sigmoid function. **(c)** The neural network models have two hidden layers with a 100 nodes for each layer.

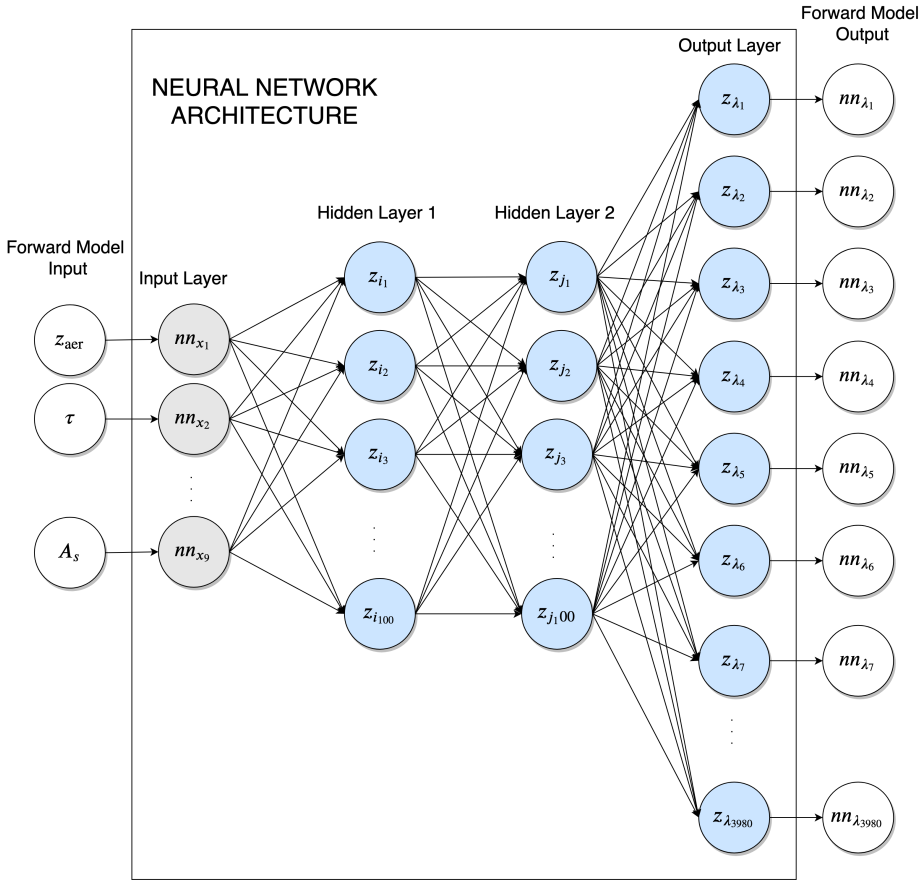

Figure 4.4: Schematic of each of the three neural networks in NN. There are two hidden layers, each containing 100 nodes. z represents inputs for each of the nodes, whereas nn represents the inputs and outputs of the neural network.

errors, generally within 1-3% of Disamar calculations. Averaged convolved errors of the neural network model for the sun normalised radiance (NN_I) did not exceed 1%. The neural network model for the derivative of the reflectance with respect to τ and z_{aer} perform well in general for parts of the spectrum with large oxygen absorption cross sections, where the value of the derivatives are high (indicating a higher amount of information content from those specific wavelength regions). Errors in the deepest part of the R-branch between 759 nm and 762 nm and the P-branch between 752.50 nm and 765 nm, do not exceed 3% for $NN_{K_{zaer}}$. The same can be said for NN_{K_τ}, which displays errors in the range of 1% in the same wavelength region. For wavelengths outside of the deepest parts of the R and P-branch, the relative errors are large, and exceed 10% easily. However, the relative errors are calculated as the absolute value of the difference between the true spectrum and the neural network calculated spectrum, divided by the true spectrum. These values can be very large when the value of the true spectrum is very small, which is the case for the derivatives outside the deepest part of the R and P branches. The consequence of these errors in a retrieval scenario from synthetic and real spectra are discussed in the following section.

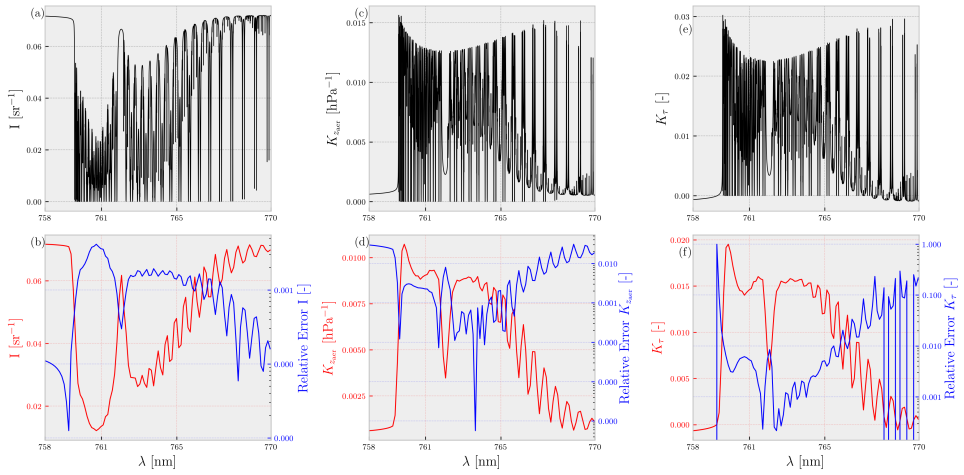

Figure 4.5: Performance of the finalised neural network. The top row represents the averaged output of each of the neural networks for surface albedo less than 0.4. The bottom row represents the convolved version of the top row (plotted as the red line with the left-handed y-axis) and the convolved relative error (plotted in log scale) with the truth (plotted in blue with the right-handed y-axis). The relative errors are computed as the absolute value of the difference (post-convolution) between the averaged true and averaged predicted spectra, divided by the averaged true spectra. (a,b) represent the neural network computed sun-normalised radiances, (c,d) represent the same for the derivative of reflectance with respect to aerosol layer height, and (e,f) the same with respect to aerosol optical thickness.

4.4 Comparison between Disamar and NN aerosol layer height retrieval algorithms

To test the NN augmented retrieval algorithm, we apply the generated NN models to synthetic test data and real data from TROPOMI, and compare its retrieval capabilities to those of Disamar. The synthetic data were produced using the Disamar radiative transfer model because of which we expect the online radiative transfer retrievals to be generally better than the NN-based retrievals. The aerosol model used in the retrieval is as in Section 4.2.1, using fixed parameters for aerosol single scattering albedo, aerosol layer thickness and aerosol scattering phase function.

4.4.1 Performance of NN versus Disamar in retrieving aerosol layer height in the presence of model errors

A comparison of biases (in the presence of model errors) in the final retrieved solution is indicative of the efficacy of NN in replacing Disamar to retrieve ALH. To directly compare z_{aer} retrieval capabilities of Disamar and NN, radiance and irradiance spectra convolved with a TROPOMI slit function were generated to replicate TROPOMI-measured spectra. Bias is defined as the difference between retrieved and true aerosol layer height (i.e., retrieved - true). A total of 2000 scenes for four synthetic experiments were generated from the test data set containing TROPOMI geometries, with randomly varied model errors in aerosol single scattering albedo, Henyey-Greenstein phase function asymmetery parameter, and surface albedo (described in Table 4.3). Figure 4.6 compares the retrieved z_{aer} from line-by-line and neural network approaches for each of the synthetic experiments. A histogram of these differences is plotted in Figure 4.7.

The retrieved aerosol layer heights from Disamar and NN in the presence of model errors in aerosol layer thickness were found to be almost similar (Figure 4.6a), with a Pearson correlation coefficient close to 1.0. Introducing model errors in other aerosol properties such as single scattering albedo (Figure 4.6b) and scattering phase function (Figure 4.6c) also resulted in a similar agreement between Disamar and NN retrieved aerosol layer heights. Furthermore, both methods retrieved similar aerosol layer heights in the presence of model errors in surface albedo as well (Figure 4.6d).

A total of 5558 retrievals out of the 8000 difference cases converged to a final solution. On average, z_{aer} retrieved using NN differed by approximately 5.0 hPa from the same using Disamar (Figure 4.7), with a median of approximately 2.0 hPa. The spread of the retrieval differences were minimal, with a majority of the retrievals differing by less than 13.0 hPa. Differences close to and above 100.0 hPa did exist, but such retrievals were very uncommon.

Out of the 8000 scenes within the synthetic experiment, NN retrieved aerosol layer heights for 546 scenes where Disamar did not. Contrariwise, 586 scenes converged for Disamar and not for NN. A comparison of the biases from these odd retrieval results is plotted in Figure 4.8, which indicates that retrievals from NN in cases where Disamar fails are realistic as the distribution of the biases is very similar to those cases when Disamar succeeds and NN does not (Figure 4.8). Retrievals using the NN forward model on average required three more iterations to reach a solution when compared to the same by Disamar. Similarly, retrievals from Disamar had a significantly lower minimised cost function (less

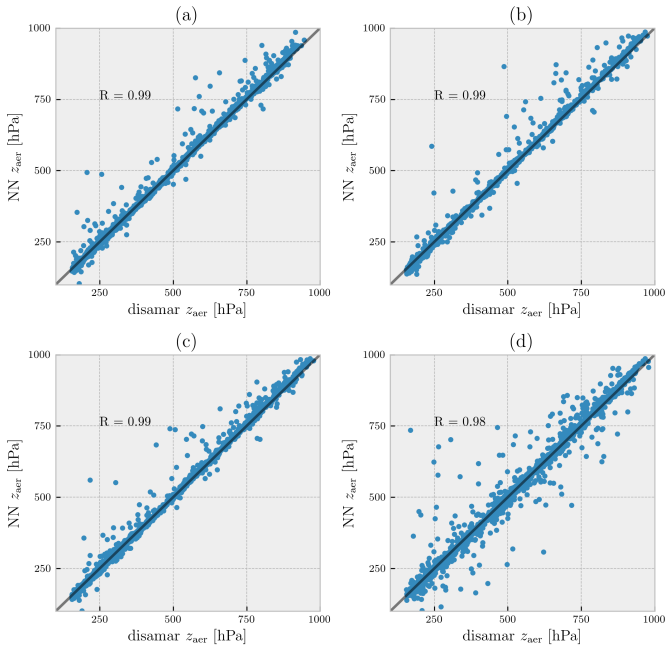

Figure 4.6: Retrieved layer heights compared between Disamar and NN for 2000 synthetic spectra in the presence of model errors. The dots represent converged scenes only, with the x axis representing retrievals from Disamar and the y-axis representing the same from NN. The model errors represented in this figure are (a) aerosol layer pressure thickness, (b) aerosol single scattering albedo, (c) aerosol scattering phase function asymmetry factor, and (d) surface albedo. These results as well as the introduced model errors are summarised in Table 4.3. The Pearson correlation coefficient (R) between the retrieved z_{aer} from different methods is mentioned in each of the plots.

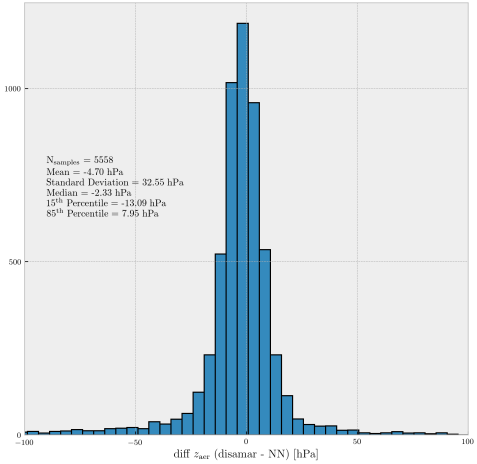

Figure 4.7: Histogram of differences between the retrieved z_{aer} values using Disamar and NN retrieval methods for synthetic spectra generated by Disamar. Total number of cases is 8000, whereas the plot contains 5558 retrieved samples for both Disamar and NN; non-converged cases are not included. A map of these differences are plotted in Figure 4.10c.

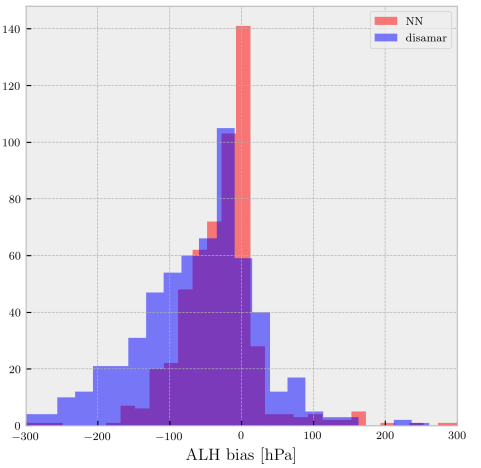

Figure 4.8: Histogram of biases (retrieved - true) for scenes in the synthetic experiment for which either NN converges to a solution (red bar plot) and Disamar does not, or Disamar converges to a solution (blue bar plot) whereas NN does not.

by four orders of magnitude on average) at the end of the retrieval when compared to NN. This is within expectation as NN cannot truly replicate Disamar. Having tested the NN augmented retrieval algorithm in a synthetic environment, the retrieval algorithm was installed into the operational TROPOMI processor for testing with real data.

4.4.2 Application to December 2017 Californian forest fires observed by TROPOMI

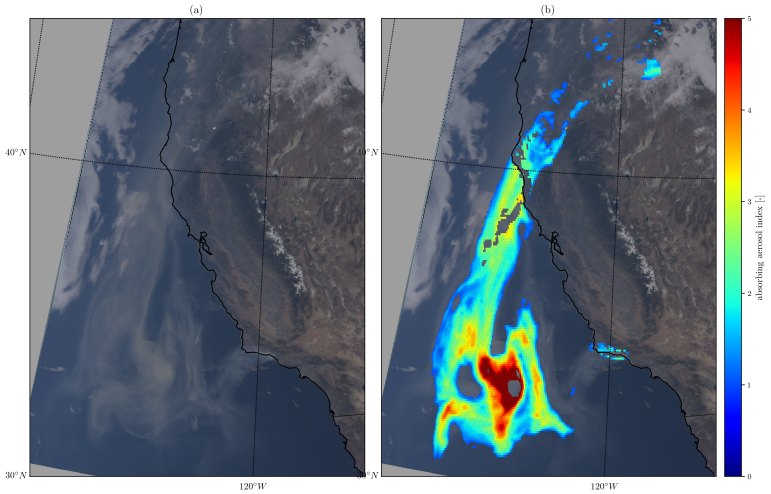

Figure 4.9: (a) MODIS Terra image of the December 12, 2017 Southern Californian wildfire plume, extending from land to ocean. (b) Calculated aerosol absorbing index from the TROPOMI level-2 processor. Missing pixels are flagged by a cloud mask or land-sea mask, or have an AAI less than 1.0.

The December 2017 Southern California wildfires have been attributed to very low

humidity levels, following delayed autumn precipitation and severe multi-annual drought [25]. Particularly on December 12, the region of the fires was cloud-free, owing to high-pressure conditions. A MODIS Terra image of the plume and the retrieved AAI from TROPOMI is plotted in Figure 4.9. The biomass burning plume extended well beyond the coastline and over the ocean (Figure 4.9a), which provides a roughly cloud-free and low surface brightness test case for implementing the aerosol layer height retrieval algorithm. The AAI values were above 5.0 in the bulk of the plume (Figure 4.9b), indicating a very high concentration of elevated absorbing aerosols. Pixels with an AAI value less than 1.0 were excluded from the retrieval experiment. Cloud-contaminated pixels were removed from the data selected for processing using the FRESCO cloud mask product from TROPOMI (maximum cloud fraction of 0.2), but parts of the biomass burning plume that did not contain any clouds were also removed as the cloud fraction values for these pixels were higher than the threshold. This is because FRESCO-based cloud fraction values over cloud-free scenes containing aerosols (biomass burning aerosols in this case) are generally expected to be positively biased. The retrieval algorithms did not process pixels in the coastline, where the surface albedo retrieval is likely to be wrong.

Figure 4.10 compares the retrieved z_{aer} over the plume using the line-by-line and neural network based forward models, respectively. The number of the converged retrievals is 7418 for the line-by-line algorithm, but 7370 for the neural network algorithm. The differences between z_{aer} (disamar) and z_{aer} (NN) go up to as much as 0.5 km (Figure 4.10c). A majority of the negative differences are for the part of the plume extending from the coast between 47°N and 40°N. Figure 4.11 provides plots for further comparison between the two retrieval techniques. The neural network augmented processor retrieved aerosol layer heights which were (on average) less than 50.0 meters apart from the same by the line-by-line counterpart (Figure 4.11b). The standard deviation of the differences are approximately 160 meters, which indicates the presence of outliers. However, a majority of the differences in the two retrievals are less than 100 meters; this is indicated by the 15^{th} and the 85^{th} percentile of these differences of -115.0 meters and 40.0 meters respectively. Although the retrieval algorithms have good agreement, they primarily differed for the lower aerosol loading scenes (Table 4.4). The majority of the pixels where the neural network algorithm differed from the line-by-line counterpart by more than 200 meters were for AAI values less than 2.0 (Figure 4.11c). Most of these biases were caused by an over-estimation of the retrieved aerosol layer height using the neural network algorithm, in comparison to the same from disamar. Pixels with AAI values larger than 5.0 also showed a consistent bias of 60 meters with a standard deviation of 30 meters. This bias is not well understood.

The time required by the line-by-line operational processor was 184.01±0.50 seconds per pixel, whereas the same for the neural network processor was 0.167± 0.0003 seconds per pixel. The neural network algorithm shows an improvement in the computational speed by three orders of magnitude over the line-by-line retrieval algorithm. The computational speed gained from implementing NN enables retrieval of aerosol layer heights from all potential scenes in the entire orbit within the stipulated operational processing time slot.

Table 4.3: A count of converged and non-converged results from synthetic experiments comparing retrieved aerosol layer heights between Disamar and NN.

	experiment		Converged (Disamar)		Converged (NN)	
model parameter	sim	ret	yes	no	yes	no converged
p_{thick}	200 hPa	50 ha	1641	359	1550	450
ω	[0.93, 0.96]	0.95	1396	604	1412	588
g	[0.67, 0.73]	0.7	1571	429	1567	433
A_s	$[0.95A_s, 1.05A_s]$	A_s	1536	464	1575	425

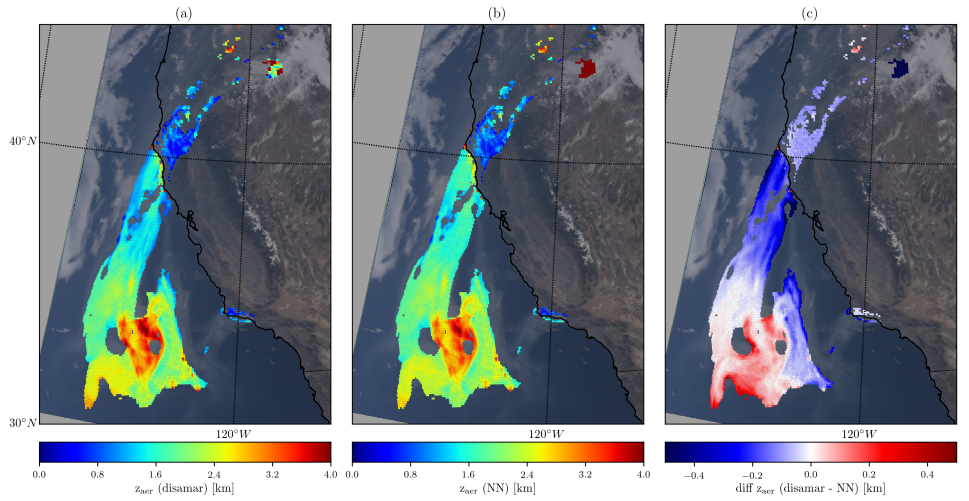

Figure 4.10: (a) Aerosol layer height retrieved using Disamar as the forward model. (b) The same, but with NN replacing Disamar in the operational processor. (c) difference between Disamar and NN retrieved aerosol layer heights.

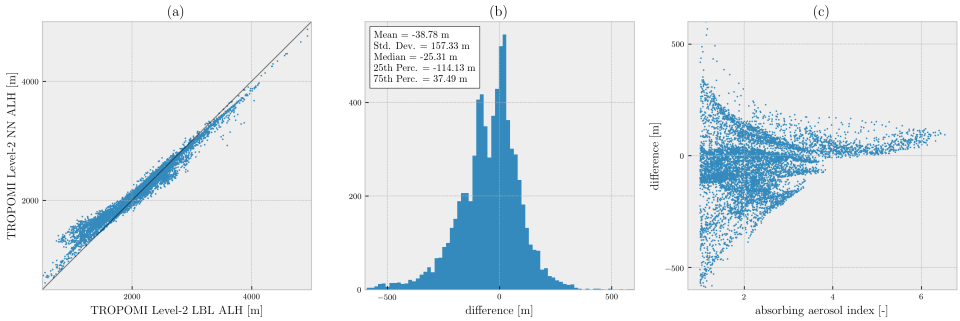

Figure 4.11: Comparison of retrieved aerosol layer heights from TROPOMI-measured spectra (orbit number 858) for the 12th December, 2017 Southern California fires using Disamar and NN. (a) Retrieved aerosol layer heights from the two methods; (b) Histogram of the difference between retrieved heights from Disamar and NN. The difference is defined as z_{aer}(Disamar) - z_{aer}(NN). (c) Differences compared to TROPOMI's operational AAI product (x axis).

Table 4.4: Statistics of difference between retrieved z_{aer} from Disamar and NN from Figure 4.10c.

AAI [-]	number of samples	mean [m]	median [m]	std [m]	15^{th} percentile [m]	85^{th} percentile [m]
<2.0	3227	-50.74	-62.10	206.44	-228.65	108.31
2.0 - 3.0	2723	-54.96	-43.20	110.75	-184.85	67.10
3.0 - 5.0	1167	10.32	19.42	63.65	-61.63	65.26
>5.0	253	61.35	61.00	30.954	26.56	95.22

4.5 Conclusion

Of the algorithms that currently retrieve TROPOMI's suite of level-2 products, the aerosol layer height processor is an example of one that requires online radiative transfer calculations. These online calculations have traditionally been tackled with KNMI's radiative transfer code disamar, which calculates (among other parameters) sun-normalised radiances in the oxygen A-band. There are, in total, 3980 line-by-line calculations per iteration in the optimal estimation scheme, requiring several minutes to retrieve aerosol layer height estimates from a single scene. This limits the yield of the aerosol layer height processor significantly.

The bottleneck is identified to be the number of calculations Disamar needs to do at every iteration of the Gauss-Newton scheme of the estimation process. As a replacement, this chapter proposes using artificial neural networks in the forward model step. Three neural networks are trained, for the sun-normalised radiance and the derivative of the reflectance with respect to aerosol layer height and aerosol optical thickness, the two state vector elements. As the goal is to replicate and replace Disamar, line-by-line forward model calculations from Disamar were used to train these neural networks. A total of 500,000 spectra were generated using Disamar, and each of the neural network models was trained for a total of 1 million iterations with the mean squared error between the training data output and the neural network output being the cost function to be minimised in the

optimisation process.

Over a test data set with 100,000 different scenes unique from the training data set, the neural network models performed well, with errors not exceeding 1-3% in general in the predicted spectra and derivatives. Having tested the neural network models for prediction errors in the forward model output spectra, they were implemented into the aerosol layer height breadboard algorithm and further tested for retrieval accuracy. In order to do so, experiments with synthetic as well as real data were conducted. The synthetic scenes included 2000 spectra with different model errors in aerosol and surface properties. In these cases, the neural network algorithm showed very good compatibility with the aerosol layer height algorithm, since it was able to replicate the biases satisfactorily.

We evaluate aerosol layer heights retrieved from TROPOMI measurements over Southern California on 12 December, 2017, when the fire plume extensively floats from land to ocean over a dry and almost cloudless scene. Operational retrievals using both Disamar and the neural network forward models showed very similar results, with a few outliers around 500 meters for pixels containing low aerosol loads. These biases were outweighed by the upgrade in the computational speed of the retrieval algorithm, as the neural network augmented processor observed a speedup of three orders of magnitude, making the aerosol layer height processor operationally feasible.

In this chapter, the previous method of retrieval was directly augmented with the neural network method. With the boost in the computational speed of top-of-atmosphere reflectances in the oxygen A-band, a host of assumptions that were once necessary for a line-by-line RTM are now antiquated. The neural network radiative transfer method allows for possibilities to improve upon the previous ways of retrieving aerosol layer height from the oxygen A-band, including removing the several simplifications mentioned in Section 4.2.1. However, before starting a project on improving the ALH retrieval algorithm, a benchmark of the current state-of-the-art must be established. The following chapter (Chapter 5) presents a first evaluation of TROPOMI's operational Level-2 processor for the aerosol layer height retrieval algorithm.

References

[1] Abadi, M., Agarwal, A., Barham, P., Brevdo, E., Chen, Z., Citro, C., Corrado, G. S., Davis, A., Dean, J., Devin, M., Ghemawat, S., Goodfellow, I., Harp, A., Irving, G., Isard, M., Jia, Y., Jozefowicz, R., Kaiser, L., Kudlur, M., Levenberg, J., Mané, D., Monga, R., Moore, S., Murray, D., Olah, C., Schuster, M., Shlens, J., Steiner, B., Sutskever, I., Talwar, K., Tucker, P., Vanhoucke, V., Vasudevan, V., Viégas, F., Vinyals, O., Warden, P., Wattenberg, M., Wicke, M., Yu, Y., and Zheng, X. (2015). TensorFlow: Large-scale machine learning on heterogeneous systems. Software available from tensorflow.org.

[2] Chance, K. and Kurucz, R. (2010). An improved high-resolution solar reference spectrum for earth's atmosphere measurements in the ultraviolet, visible, and near infrared. *Journal of Quantitative Spectroscopy and Radiative Transfer*, 111(9):1289–1295.

[3] Chimot, J., Veefkind, J. P., Vlemmix, T., de Haan, J. F., Amiridis, V., Proestakis, E., Marinou, E., and Levelt, P. F. (2017). An exploratory study on the aerosol height retrieval from OMI measurements of the 477 nm O2O2 spectral band using a neural network approach. *Atmos. Meas. Tech.*, 10(3):783–809.

[4] Chimot, J., Veefkind, J. P., Vlemmix, T., and Levelt, P. F. (2018). Spatial distribution analysis of the OMI aerosol layer height: a pixel-by-pixel comparison to CALIOP observations. *Atmos. Meas. Tech.*, 11(4):2257–2277.

[5] Colosimo, S. F., Natraj, V., Sander, S. P., and Stutz, J. (2016). A sensitivity study on the retrieval of aerosol vertical profiles using the oxygen a-band. *Atmospheric Measurement Techniques*, 9(4):1889–1905.

[6] Corradini, S. and Cervino, M. (2006). Aerosol extinction coefficient profile retrieval in the oxygen A-band considering multiple scattering atmosphere. Test case: SCIAMACHY nadir simulated measurements. *Journal of Quantitative Spectroscopy and Radiative Transfer*, 97(3):354–380.

[7] Davis, A. B., Kalashnikova, O. V., and Diner, D. J. (2017). Aerosol layer height over water from o2 a-band: Mono-angle hyperspectral and/or bi-spectral multi-angle observations.

[8] de Haan, J. F., Bosma, P. B., and Hovenier, J. W. (1987). The adding method for multiple scattering calculations of polarized light. *Astronomy and Astrophysics*, 183.

[9] Dee, D. P., Uppala, S. M., Simmons, A. J., Berrisford, P., Poli, P., Kobayashi, S., Andrae, U., Balmaseda, M. A., Balsamo, G., Bauer, P., Bechtold, P., Beljaars, A. C. M., van de Berg, L., Bidlot, J., Bormann, N., Delsol, C., Dragani, R., Fuentes, M., Geer, A. J., Haimberger, L., Healy, S. B., Hersbach, H., Hólm, E. V., Isaksen, L., Kållberg, P., Köhler, M., Matricardi, M., McNally, A. P., Monge-Sanz, B. M., Morcrette, J.-J., Park, B.-K., Peubey, C., de Rosnay, P., Tavolato, C., Thépaut, J.-N., and Vitart, F. (2011). The ERA-Interim reanalysis: configuration and performance of the data assimilation system. *Quarterly Journal of the Royal Meteorological Society*, 137(656):553–597.

[10] Dubuisson, P., Frouin, R., Dessailly, D., Duforêt, L., Léon, J.-F., Voss, K., and Antoine, D. (2009). Estimating the altitude of aerosol plumes over the ocean from reflectance ratio measurements in the O2 A-band. *Remote Sensing of Environment*, 113(9):1899–1911.

[11] Frankenberg, C., Hasekamp, O., O'Dell, C., Sanghavi, S., Butz, A., and Worden, J. (2012). Aerosol information content analysis of multi-angle high spectral resolution measurements and its benefit for high accuracy greenhouse gas retrievals. *Atmos. Meas. Tech.*, 5(7):1809–1821.

[12] Gabella, M., Kisselev, V., and Perona, G. (1999). Retrieval of aerosol profile variations from reflected radiation in the oxygen absorption A band. *Applied Optics*, 38(15):3190–3195.

[13] Geddes, A. and Bösch, H. (2015). Tropospheric aerosol profile information from high-resolution oxygen a-band measurements from space. *Atmospheric Measurement Techniques*, 8(2):859–874.

[14] Hasekamp, O. P. and Butz, A. (2008). Efficient calculation of intensity and polarization spectra in vertically inhomogeneous scattering and absorbing atmospheres. *Journal of Geophysical Research: Atmospheres*, 113(D20):D20309.

[15] Henyey, L. C. and Greenstein, J. L. (1941). Diffuse radiation in the Galaxy. *The Astrophysical Journal*, 93:70.

[16] Hollstein, A. and Fischer, J. (2014). Retrieving aerosol height from the oxygen A band: a fast forward operator and sensitivity study concerning spectral resolution, instrumental noise, and surface inhomogeneity. *Atmospheric Measurement Techniques*, 7(5):1429–1441.

[17] Kingma, D. P. and Ba, J. (2014). Adam: A Method for Stochastic Optimization. *arXiv:1412.6980 [cs]*. arXiv: 1412.6980.

[18] Kirkpatrick, J., Pascanu, R., Rabinowitz, N., Veness, J., Desjardins, G., Rusu, A. A., Milan, K., Quan, J., Ramalho, T., Grabska-Barwinska, A., Hassabis, D., Clopath, C., Kumaran, D., and Hadsell, R. (2016). Overcoming catastrophic forgetting in neural networks. *arXiv:1612.00796 [cs, stat]*. arXiv: 1612.00796.

[19] Levelt, P. F., Oord, G. H. J. v. d., Dobber, M. R., Malkki, A., Visser, H., Vries, J. d., Stammes, P., Lundell, J. O. V., and Saari, H. (2006). The ozone monitoring instrument. *IEEE Transactions on Geoscience and Remote Sensing*, 44(5):1093–1101.

[20] Loyola, D. G., Gimeno García, S., Lutz, R., Argyrouli, A., Romahn, F., Spurr, R. J. D., Pedergnana, M., Doicu, A., Molina García, V., and Schüssler, O. (2018). The operational cloud retrieval algorithms from tropomi on board sentinel-5 precursor. *Atmospheric Measurement Techniques*, 11(1):409–427.

[21] Loyola, D. G. R. (2004). Automatic cloud analysis from polar-orbiting satellites using neural network and data fusion techniques. In *IGARSS 2004. 2004 IEEE International Geoscience and Remote Sensing Symposium*, volume 4, pages 2530–2533 vol.4.

[22] McCulloch, W. S. and Pitts, W. (1943). A logical calculus of the ideas immanent in nervous activity. *The bulletin of mathematical biophysics*, 5(4):115–133.

[23] Nanda, S., de Graaf, M., Sneep, M., de Haan, J. F., Stammes, P., Sanders, A. F. J., Tuinder, O., Veefkind, J. P., and Levelt, P. F. (2018a). Error sources in the retrieval of aerosol information over bright surfaces from satellite measurements in the oxygen A band. *Atmos. Meas. Tech.*, 11(1):161–175.

[24] Nanda, S., Veefkind, J. P., de Graaf, M., Sneep, M., Stammes, P., de Haan, J. F., Sanders, A. F. J., Apituley, A., Tuinder, O., and Levelt, P. F. (2018b). A weighted least squares approach to retrieve aerosol layer height over bright surfaces applied to GOME-2 measurements of the oxygen A band for forest fire cases over Europe. *Atmos. Meas. Tech.*, 11(6):3263–3280.

[25] Nauslar, N. J., Abatzoglou, J. T., and Marsh, P. T. (2018). The 2017 North Bay and Southern California Fires: A Case Study. *Fire*, 1(1):18.

[26] Pelletier, B., Frouin, R., and Dubuisson, P. (2008). Retrieval of the aerosol vertical distribution from atmospheric radiance. volume 7150, page 71501R. International Society for Optics and Photonics.

[27] Rodgers, C. D. (2000). *Inverse methods for atmospheric sounding: theory and practice*, volume 2. World Scientific.

[28] Sanders, A. F. J. and de Haan, J. F. (2013). Retrieval of aerosol parameters from the oxygen A band in the presence of chlorophyll fluorescence. *Atmospheric Measurement Techniques*, 6(10):2725–2740.

[29] Sanders, A. F. J. and de Haan, J. F. (2016). TROPOMI ATBD of the Aerosol Layer Height product.

[30] Sanders, A. F. J., de Haan, J. F., Sneep, M., Apituley, A., Stammes, P., Vieitez, M. O., Tilstra, L. G., Tuinder, O. N. E., Koning, C. E., and Veefkind, J. P. (2015). Evaluation of the operational Aerosol Layer Height retrieval algorithm for Sentinel-5 Precursor: application to Oxygen A band observations from GOME-2A. *Atmospheric Measurement Techniques*, 8(11):4947–4977.

[31] Sanghavi, S., Martonchik, J. V., Landgraf, J., and Platt, U. (2012). Retrieval of the optical depth and vertical distribution of particulate scatterers in the atmosphere using O_2 A- and B-band SCIAMACHY observations over Kanpur: a case study. *Atmospheric Measurement Techniques*, 5(5):1099–1119.

[32] Shaw, G. L. (1986). Donald Hebb: The Organization of Behavior. In Palm, G. and Aertsen, A., editors, *Brain Theory*, pages 231–233, Berlin, Heidelberg. Springer.

[33] Sioris, C. E. and Evans, W. F. J. (2000). Impact of rotational Raman scattering in the O2A band. *Geophysical Research Letters*, 27(24):4085–4088.

[34] Tilstra, L. G., Tuinder, O. N. E., Wang, P., and Stammes, P. (2017). Surface reflectivity climatologies from UV to NIR determined from Earth observations by GOME-2 and SCIAMACHY: GOME-2 and SCIAMACHY surface reflectivity climatologies. *Journal of Geophysical Research: Atmospheres*.

[35] Timofeyev, Y., Vasilyev, A., and Rozanov, V. (1995). Information content of the spectral measurements of the 0.76 m o2 outgoing radiation with respect to the vertical aerosol optical properties. *Advances in Space Research*, 16:91–94.

[36] Vasilkov, A., Joiner, J., and Spurr, R. (2013). Note on rotational-Raman scattering in the O_2 A- and B-bands. *Atmospheric Measurement Techniques*, 6(4):981–990.

[37] Veefkind, J. P., Aben, I., McMullan, K., Förster, H., de Vries, J., Otter, G., Claas, J., Eskes, H. J., de Haan, J. F., Kleipool, Q., van Weele, M., Hasekamp, O., Hoogeveen, R., Landgraf, J., Snel, R., Tol, P., Ingmann, P., Voors, R., Kruizinga, B., Vink, R., Visser, H., and Levelt, P. F. (2012). TROPOMI on the ESA Sentinel-5 Precursor: A GMES mission for global observations of the atmospheric composition for climate, air quality and ozone layer applications. *Remote Sensing of Environment*, 120:70–83.

[38] Wang, P., Stammes, P., van der A, R., Pinardi, G., and van Roozendael, M. (2008). FRESCO+: an improved O2 A-band cloud retrieval algorithm for tropospheric trace gas retrievals. *Atmos. Chem. Phys.*, 8(21):6565–6576.

[39] Wang, P., Tuinder, O. N. E., Tilstra, L. G., de Graaf, M., and Stammes, P. (2012). Interpretation of FRESCO cloud retrievals in case of absorbing aerosol events. *Atmospheric Chemistry and Physics*, 12(19):9057–9077.

[40] Wen, S. and Itti, L. (2018). Overcoming catastrophic forgetting problem by weight consolidation and long-term memory. *arXiv:1805.07441 [cs, stat]*. arXiv: 1805.07441.

[41] Wengert, R. E. (1964). A Simple Automatic Derivative Evaluation Program. *Commun. ACM*, 7(8):463–464.

[42] Widrow, B. and Hoff, M. E. (1962). Associative Storage and Retrieval of Digital Information in Networks of Adaptive "Neurons". In Bernard, E. E. and Kare, M. R., editors, *Biological Prototypes and Synthetic Systems: Volume 1 Proceedings of the Second Annual Bionics Symposium sponsored by Cornell University and the General Electric Company, Advanced Electronics Center, held at Cornell University, August 30–September 1, 1961*, pages 160–160. Springer US, Boston, MA.

[43] Xu, X., Wang, J., Wang, Y., Zeng, J., Torres, O., Yang, Y., Marshak, A., Reid, J., and Miller, S. (2017). Passive remote sensing of altitude and optical depth of dust plumes using the oxygen A and B bands: First results from EPIC/DSCOVR at Lagrange-1 point. *Geophysical Research Letters*, 44(14):2017GL073939.

[44] Zeng, Z.-C., Natraj, V., Xu, F., J. Pongetti, T., Shia, R.-L., A. Kort, E., C. Toon, G., P. Sander, S., and L. Yung, Y. (2018). Constraining aerosol vertical profile in the boundary layer using hyperspectral measurements of oxygen absorption. *Geophysical Research Letters*.

5

A first evaluation of retrieved aerosol heights from the TROPOMI ALH algorithm

With the neural network algorithm implemented to the operational TROPOMI level-2 processor, the quality of the ALH retrieval algorithm can now be tested. This is an important step in the development of the algorithm — a first validation of the retrieved product acts as a benchmark from which the product needs to be improved upon.

An appropriate choice of data for comparing the quality of the retrieved ALHs from measured TROPOMI spectra are lidars, either atmospheric or ground based. In this chapter, the data from the CALIOP instrument on board the CALIPSO mission is used for any TROPOMI-CALIOP colocation (spatially and temporally) all throughout the globe. While the chapter presents colocated data for the entire globe, a few well-understood cases are chosen as a subject of deeper comparison between TROPOMI and CALIOP retrieved aerosol height. The research goal of this chapter is,

Provide a first benchmark of the ALH retrieval algorithm by comparing TROPOMI operational level-2 ALHs to other data sources.[1]

[1]This chapter is published in https://doi.org/10.5194/amt-13-3043-2020, 2020.

5.1 Introduction

In the fourth quarter of 2019, an operational data stream of retrieved ALHs derived from measured oxygen A-band spectra by TROPOMI has been made available to the general public; the TROPOMI operational UVAI product augmented by the TROPOMI ALH product has the potential to further the operational monitoring of aerosol properties globally. This chapter discusses some key features of the product and its limitations by comparing it with co-located CALIOP profiles, and paints a future outlook of the evolution of the TROPOMI ALH algorithm. The chapter looks into more than two million colocations between TROPOMI ground pixels and CALIOP profiles over an extended period of time covering several months from May 2018 till March 2019, in order to draw conclusions on the accuracy of the TROPOMI ALH retrievals. Further on, the chapter also discusses four selected cases in and around West Africa for a deeper analysis of the comparison with CALIOP data; the choice of using the Africa as a study area arises from the fact that a significant majority of colocations between TROPOMI and CALIOP are concentrated around the West African region.

In Section 5.2 of this chapter, we discuss the data and methods used in this chapter; section 5.2.1 describes the retrieval algorithm and highlights different diagnostic parameters available for assessing the product's quality. Following this, the comparison between CALIOP and TROPOMI estimates of aerosol heights are presented in 5.3 — Section 5.3.1 presents an overall analysis of a large number of TROPOMI-CALIOP colocations, followed by Section 5.3.2 which discusses selected cases for a deeper dive into the TROPOMI product. The chapter concludes with section 5.4, highlighting important areas of potential improvement in the current TROPOMI ALH product.

5.2 Data and Methods

5.2.1 TROPOMI ALH

The TROPOMI ALH product is derived from measurements of the oxygen A-band in the near infrared region between 758 nm and 770 nm. Within this spectral range, TROPOMI measures top of atmosphere radiances and solar irradiances with a spectral resolution between 0.34 nm and 0.35 nm and a spectral sampling of 0.126 nm. The retrieval algorithm exploits the absorption characteristics of molecular oxygen, which varies with the photon path length — the photon path length for an aerosol layer closer to the surface is longer, which appears as deeper oxygen absorption lines in the measured spectrum (see Figure 1.9).

The reported ALH is the height of a single aerosol layer for the entire atmospheric column within the scene measured by TROPOMI; in reality however, there can be several cases where distinctly separated elevated and boundary layer aerosols are present in the same scene. In such cases, the retrieval algorithm is expected to retrieve an optical centroid pressure or height of the two (or more) aerosol layers, depending on the atmospheric level of the aerosol layer from which most of the photons are scattered back. For instance, if the elevated aerosol layer contributes significantly more than the boundary layer aerosols to the top of atmosphere measured spectra, the ALH retrieval algorithm is expected to retrieve values closer to the elevated layer.

The technique for retrieving ALH is based on optimal estimation [10], where an RTM

that calculates the top of atmosphere oxygen A-band spectra is fitted to TROPOMI measured oxygen A-band spectra. The cost function that is minimised in this estimation step, χ^2, is defined as

$$\chi^2 = [\boldsymbol{y} - \boldsymbol{F}(\boldsymbol{x}, \boldsymbol{b})]^T \mathrm{S}_\epsilon{}^{-1} [\boldsymbol{y} - \boldsymbol{F}(\boldsymbol{x}, \boldsymbol{b})] + (\boldsymbol{x} - \boldsymbol{x_a})^T \mathrm{S_a}{}^{-1} (\boldsymbol{x} - \boldsymbol{x_a}), \tag{5.1}$$

where, $\boldsymbol{y}$ is the reflectance spectra calculated from measured radiances and irradiances for the oxygen A-band, $\boldsymbol{F}(\boldsymbol{x}, \boldsymbol{b})$ is the modeled reflectance for input parameters $\boldsymbol{b}$, of which the state vector $\boldsymbol{x}$ containing ALH z_{aer} and aerosol optical thickness τ is a part, $\boldsymbol{x_a}$ is the a priori state vector and $\mathrm{S}_\epsilon{}^{-1}$ and $\mathrm{S_a}{}^{-1}$ are the measurement error covariance and the a priori error covariance matrices. Optimal estimation is an iterative process, requiring several iterations to minimise the cost function described in Equation 5.1. The approach is Gauss-Newton, with a maximum number of iterations set at 10. If the optimal estimation does not converge within these iterations, the ALH field in the final level-2 product is filled with a fill value. For a given measurement, optimal estimation is said to have converged to a final solution if the update to the state vector for the next iteration is less than the expected precision.

The χ^2 is a measure of how close the modelled sun-normalised radiances are to the observations, with smaller values representing a better fit. The consequence of the many assumptions in the model (described in Section 4.2.1) result in a large χ^2 (to the order of 1E4-1E7), with larger χ^2 representing a larger departure between the model and the observation. There are several reasons for these departures, the more important ones being the presence of undetected clouds in the scene, incorrect surface reflectance information, and multiple aerosol layers. These attributes are not parameterised into the RTM, and can be source of discrepancies between the measured and the modeled reflectances. The RTM in this case is a neural network model that has learned parts of a full physics RTM derived from de Haan et al. [1], described in Nanda et al. [7] (Section 3), which is three orders of magnitude faster than DISAMAR. In short, the atmosphere is simplified by DISAMAR in order to reduce computational burden, and the neural network forward model is implemented for a further performance boost in an operational environment; for instance, DISAMAR ignores rotational raman scattering even though literature has shown that the oxygen A-band ring effects are sensitive to ALH [14, 15]. These decisions have been made in order to speed up line-by-line calculations of DISAMAR, which are the basis of the training data for its neural network counterpart. This decision is motivated by preliminary sensitivity analyses conducted by Sanders and de Haan [11] which conclude that the effect of ignoring RRS is not significant enough to venture in its implementation into the forward model.

The surface reflectance model used in the algorithm is derived from Tilstra et al. [13], which is a Lambertian equivalent reflectance (LER) database with a spatial resolution of $0.25^\circ \times 0.25^\circ$. In contrast to TROPOMI's ALH product which is reported at 7.2 km × 3.6 km till August 6, 2019, and 5.6 km × 3.6 km thereafter, the LER database is much coarser spatially. This can lead to several artefacts in the final product, discussed further on in this chapter in Section 5.3.2. Another issue to note is in the influence of bright surfaces on the retrieval. The oxygen A-band lies beyond the red edge, a wavelength region in which vegetation has high reflectance values. This poses several challenges; a significant portion of the measured signal over land might be contributions from the surface reflectance (see Figure 2.1). If the aerosol optical thickness of the measured scene is low, the contribution of the

surface to the top of atmosphere radiance dominates over the contribution from scattering by aerosols — there are more photons that get scattered back from the surface than the aerosol layer. In such cases, the retrieval algorithm will tend to retrieve an aerosol layer closer to the surface. Generally we find that, if the contribution to the top of atmosphere reflectance from aerosols is significantly larger than the same from the surface (i.e. the aerosol layer appears brighter than the surface), the retrieval algorithm will tend to retrieve a height closer to the aerosol layer (Section 5.2 and Figure 10 from Nanda et al. [8] discuss this observation explicitly).

The forward model parameterises aerosols with a Henyey-Greenstein scattering phase function [4] with an asymmetry factor of 0.7, a single scattering albedo of 0.95, and a fixed aerosol optical thickness for an aerosol layer parameterised by a single atmospheric layer with a 50 hPa thickness. These assumptions have to be made since very little a priori information about aerosols in a scene is known. While more complex scattering models exist, the Henyey-Greenstein model has been used for retrieving ALH when the forward model was of line-by-line nature as the number of calculations it requires is far less than a scattering model such as the Mie model. Sensitivity analyses have shown that this assumption has few ramifications [12]. Fixing the single scattering albedo is a much bigger concern; while retrievals over the ocean do not suffer for a priori errors in the single scattering albedo, retrievals over land do have large errors and non-convergences which reduce as the the viewing zenith angle increases [6]. The choice of using 0.95 as a fixed value arises from average values derived by Dubovik et al. [2] from long-term observations using the aerosol robotic network (AERONET). The algorithm assumes a single aerosol layer for the entire atmosphere, within which aerosols are uniformly distributed and the aerosol volume extinction coefficient is constant. This is an important simplification to note when comparing with CALIOP profiles, since these lidar profiles have the capability to detect multiple aerosol layers. The simplicity in the aerosol profile parameterisation arises from the fact that it is impossible to know, without prior information, whether the scene consists of a single or multiple aerosol layers. While fitting of the aerosol layer pressure thickness along with the aerosol layer mid pressure does not result in large errors in the retrieved ALH, the precision of the retrieved aerosol layer mid pressure significantly deteriorates with increasing errors in the surface albedo [12]. More research has to be done before more information on the aerosol profile is retrieved from the oxygen A-band alone.

Finally, the ALH retrieval algorithm implements a pixel selection scheme before committing to retrieving ALH estimates. This pixel selection scheme involves auxiliary data products from TROPOMI such as the UVAI and cloud fraction estimates from the TROPOMI Fast Retrieval Scheme for Clouds from Oxygen absorption bands (FRESCO) algorithm [16], and the cirrus reflectances derived from the Visible Infrared Imaging Radiometer Suite (VIIRS) on the Suomi National Polar-Orbiting Partnership (Suomi NPP) satellite.

1. The maximum solar zenith angle allowed is 75°. If the pixel does not meet this criterion, it is removed from the processing and a flag is raised.

2. If the pixel over water lies in the sun-glint region (a maximum sun-glint angle of 18 °), it is processed but a sun glint warning flag is recorded in the level-2 product.

3. If the standard deviation of the surface elevation within the pixel is beyond 1000 m,

the pixel is not processed and a flag is raised. If it is beyond 300 m, a warning flag is raised and the pixel is processed.

4. If the surface covered by the pixel comprises of both land and water, a warning indicating mixed surface type is raised and the pixel is processed regardless.

5. If the pixel contains snow or ice, the pixel is not processed and a flag is raised.

6. If the TROPOMI level-2 UV Absorbing Index product reports a value below 0.0, the pixel is not processed and a flag is raised. If the value is less than 1.0, a low UVAI flag is raised.

7. If the reported cloud fraction values from the TROPOMI FRESCO product for the pixel is beyond 0.6, the pixel is not processed and a flag is raised.

8. If the VIIRS average cirrus reflectance for the pixel is beyond 0.4, the pixel is not processed and a flag is raised. If it is beyond 0.01, a warning for possible cirrus clouds is indicated.

9. If the difference between the scene albedo (calculated using a look up table) from the Level-2 UVAI product and the surface albedo from the Tilstra et al. [13] database at 380 nm is beyond 0.4, the pixel is removed from the processing pool and a flag is raised for possible cloud contamination. If this is value is beyond 0.2, a warning flag is raised.

10. The nominal TROPOMI pixels also contain radiances at a sub-pixel level, which are called small pixel radiances. If the standard deviation of the small pixel radiances is larger than 1E-7, the scene is deemed to be non-homogeneous (possibly containing clouds) and it is removed from the processing pool.

These relevant flags are reported in Table 5.1 and are available in the level-2 data products; the values for each of these flags can be accessed with bitwise-and operations for each pixel with the value of each processing quality flag. For cloud filtering, the cloud_warning flag is the preferred flag for removing possibly cloudy pixels. This flag is a combination of FRESCO cloud fraction retrievals, VIIRS cirrus reflectance retrievals and the difference between the surface albedo and the scene albedo at 380 nm. An example of applying the cloud_warning flags to filter out possibly cloudy pixels is provided in Figure 5.1.

5.2.2 CALIOP weighted extinction height

The Cloud-Aerosol Lidar with Orthogonal Polarisation (CALIOP) instrument is a part of the payload for the Cloud-Aerosol Lidar and Infrared Pathfinder Satellite Observation (CALIPSO) mission [17], which orbits the Earth in a sun-synchronous orbit. The CALIOP instrument has three backscatter receiver channel, two channels for the orthogonal measurement of received backscatter signal at 532 nm and one channel for backscatter at 1064 nm. Lidar profiles from the CALIPSO mission are a good source of data for validating retrieved ALHs from TROPOMI, because of their ability to map the vertical structure of the atmosphere. The data from the CALIOP instrument relevant for validating TROPOMI

Table 5.1: Processing Quality Flags relevant for diagnosing S5P ALH product quality. The descriptions are derived from the S5P IODD.

name	value	description
CONVERGED		
success	0	successful retrieval; warnings still possible.
sun_glint_warning	2048	pixel is in sun-glint region
cloud_warning	32768	combination of different cloud detection methods
UVAI_warning	65536	UVAI is lower than 1.0
snow_ice_warning	16384	scene contains snow/ice
NON-CONVERGED or MISSING		
convergence_error	19	optimal estimation did not converge
sza_range_error	7	Solar zenith ≥ 75°
max_iteration_convergence_error	21	no convergence; retrieval exceeds maximum iterations
aot_lower_boundary_error	22	no convergence; AOT ≤ 0.0 twice in succession
other_boundary_convergence_error	23	no convergence; state vector element crosses boundary conditions twice
solar_eclipse_filter	64	pixel not processed because of solar eclipse
cloud_filter	65	pixel skipped; FRESCO cloud fraction greater than 0.6
altitude_roughness_filter	67	pixel skipped; STD of DEM in pixel > 1000.0 m
snow_ice_filter	70	pixel skipped; pixel contains snow/ice
UVAI_filter	71	pixel skipped; UVAI < 0.0
cloud_fraction_fresco_filter	72	pixel skipped; cloud fraction > 0.6
cirrus_reflectance_viirs_filter	76	pixel skipped; VIIRS cirrus reflectance > 0.4

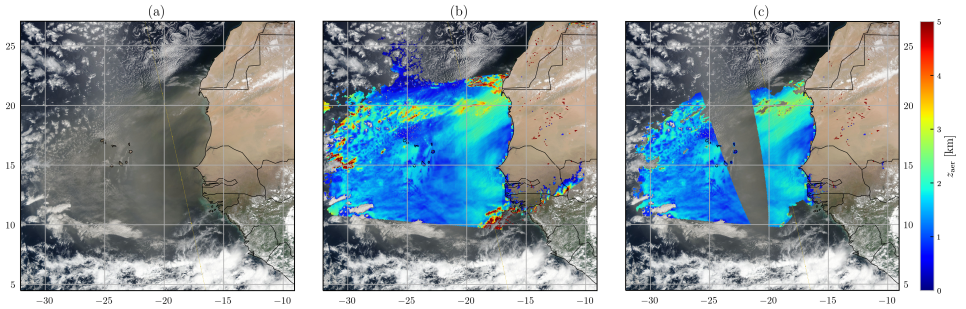

Figure 5.1: **(a)** A VIIRS corrected reflectance image over the West African coast on the 8th of June, 2018. **(b)** All successful TROPOMI retrievals within a certain bounding box. **(c)** Same as **(b)** but with all pixels that possibly fall within the sun glint region or are cloud contaminated are removed (using cloud_warning flag and sun_glint_warning from Table 5.1).

ALH are the level-1 backscatter profiles and the level-2 aerosol extinction profiles, which are used at the same time.

In this chapter, the level-1 total backscatter profiles from the 532 nm channel are used as curtain plots to visualise the vertical structure of the atmosphere. Level-2 aerosol extinction profiles from the 532 nm channel are then used to compute an aerosol weighted extinction height $\mathrm{ALH_{ext}}$, following the definition provided by Equation 1 in Koffi et al. [5],

$$\mathrm{ALH_{ext}} = \frac{\sum_{i=1}^{n} \beta_{ext,i} Z_i}{\sum_{i=1}^{n} \beta_{ext,i}}, \tag{5.2}$$

where Z_i is the height from sea level in the i^{th} lidar vertical level i (in km), and $\beta_{ext,i}$ is the aerosol extinction coefficient (in km^{-1}) at the same level. The Level-2 aerosol extinction profile product from CALIOP only includes atmospheric levels where aerosols are detected. In the case when aerosols are present over clouds, $\mathrm{ALH_{ext}}$ will be situated to the center of the aerosol layer, with any possibly undetected aerosol layers below the cloud layer not included in the calculations due to attenuation of the signal beyond the cloud layer. This is an important detail as the TROPOMI ALH algorithm cannot separate cloud and aerosol signals from the measured radiances, and cloud contamination will affect the retrieved product. In this chapter, the CALIOP 532 nm channel observations are chosen for analysis as the conclusions from the analysis of the results do not change when the 1064 nm channel observations are used instead. The CALIOP aerosol product might be cloud contaminated as well, but this is difficult to ascertain. Plotting $\mathrm{ALH_{ext}}$ over curtain plots of level-1 total backscatter profiles can be used to visually discern possibly cloud-contaminated CALIOP level-2 aerosol product.

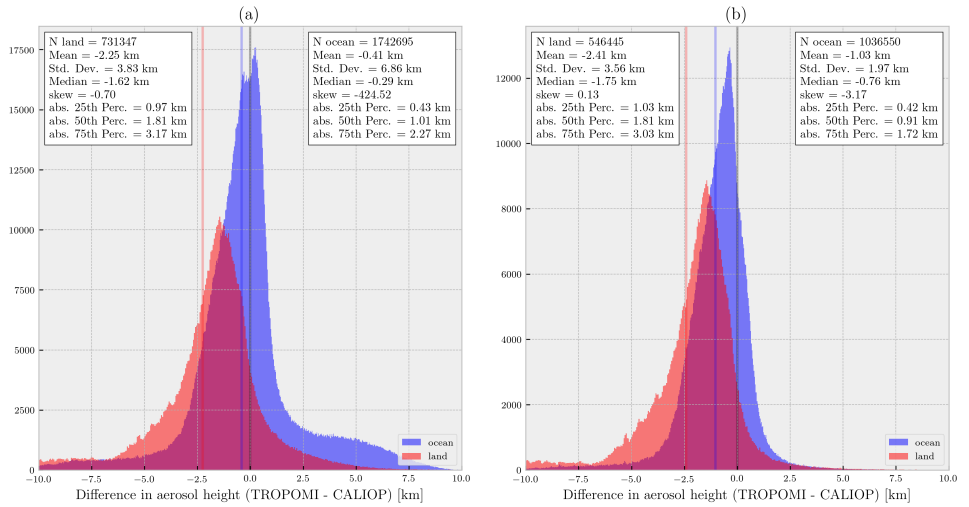

Figure 5.2: Histogram of differences between CALIOP ALH_{ext} (Equation 5.2) and TROPOMI ALH from colocated data between May 1, 2018 and February 28, 2019. Blue histogram represents TROPOMI pixels over the ocean whereas the red histogram is for TROPOMI pixels over land. The blue line represents the mean difference between TROPOMI ALH and CALIOP ALH_{ext} for TROPOMI pixels over the ocean, whereas the red line represents the same for TROPOMI pixels over land. The black line at 0.0 km difference on the x-axis is plotted to aid the reader in their interpretation of this figure. **(a)** All colocations except TROPOMI pixels falling in the sun glint region. TROPOMI pixels with retrievd AOT greater than 5.0 are discarded. For pixels over land, if the GOME-2 surface albedo is less than 0.1 or greater than 0.4, they are discarded. Similarly, over the ocean all TROPOMI pixels that have a GOME-2 surface albedo greater than 0.05 are discarded. **(b)** Same, except only TROPOMI ALH retrievals that are cloud-screened using cloud_warning flag from Table 5.1 are included.

5.3 Results

5.3.1 Comparison of TROPOMI ALH and CALIOP ALH_{ext}

TROPOMI-CALIOP colocations between 1st of May 2018 to the 28th of February 2019 are selected. Two sets of overall comparisons are done between CALIOP ALH_{ext} and TROPOMI ALH, one with all colocations (Figure 5.2a) that aren't cloud filtered and the other with a smaller subset of the dataset constrained by the cloud_warning flag from Table 5.1 (Figure 5.2b). The contrast between retrievals over land and ocean is apparent in Figure 5.4 (cloudy scenes filtered out using the cloud_warning flag), with a majority of the negative differences with values lower than -2 km occurring over land.

From Figure 5.2a , what is immediately clear is that the CALIOP ALH_{ext} are higher than the TROPOMI ALH. With an average difference of -2.25 km, median difference of -1.62 km and a standard deviation of 3.83 km, the retrieved ALH from TROPOMI over land is reported to be systematically closer to the surface than CALIOP ALH_{ext} than in comparison with retrievals over the ocean, which has a mean difference of -0.41 km, a median difference of -0.29 km and a very high standard deviation of 6.86 km. There are several cases over the ocean where TROPOMI ALH is significantly higher than the CALIOP ALH_{ext}, which could be due to cloud contamination. The comparison of the cloud-screened retrievals (Figure 5.2b) reveals that the retrieved ALH from TROPOMI over the ocean differs from CALIOP ALH_{ext} by -1.03 km on average, a median difference of -0.76 km and a standard

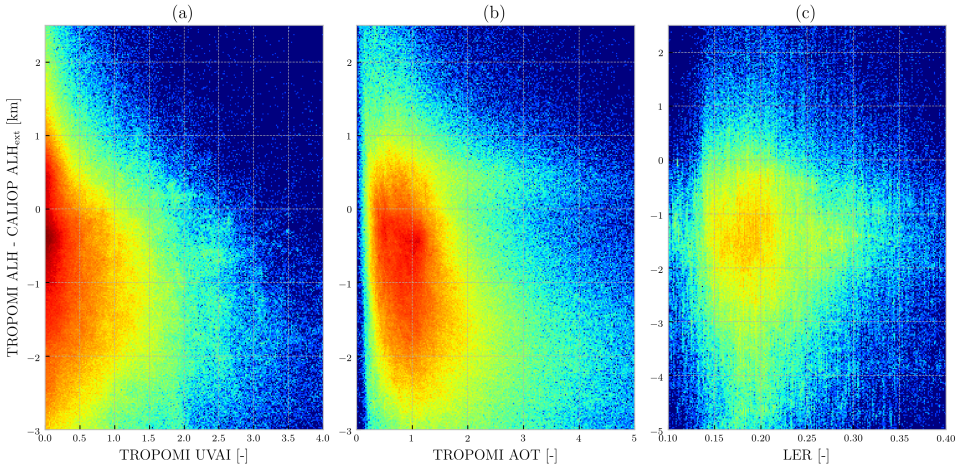

Figure 5.3: Scatter density plots of the difference between TROPOMI ALH and CALIOP ALH_{ext} as a function of **(a)** TROPOMI UVAI, **(b)** TROPOMI AOT and **(c)** GOME-2 LER for the oxygen A-band used for the TROPOMI retrievals for cases over land (with a minimum surface albedo of 0.1). The colors represent density of plots. The y axis is optimised for each plot. The data is filtered in the same fashion as in Figure 5.2, with data over the ocean and land combined for plots **(a)** and **(b)**, and data only over land for plot **(c)**.

deviation of 1.97 km. More than 50% of the TROPOMI ALH retrievals over the ocean have an absolute difference with ALH_{ext} less than 1.0 km. Retrievals over land are have a larger difference, with -2.41 km on average and a median of -1.75 km. The results are very skewed over land, with very large negative values dictating the average — this is indicated by the very large standard deviation of 3.56 km. 50% of the selected colocations over land have an absolute difference with ALH_{ext} less than approximately 1.8 km.

The distribution of the differences between TROPOMI ALH and CALIOP ALH_{ext} as a function of the retrieved UVAI (Figure 5.3a) shows that for most cases, the UVAI is below 2.0. The spread of the differences in this UVAI regime is large, which reduces as the UVAI increases. The differences seem to be less often positive as the UVAI increases; if compared with the behaviour observed between Figure 5.2a and Figure 5.2b where a majority of the positive differences vanish once the data is cloud screened, such a behaviour could be related to clouds. The distribution of the differences as a function of retrieved AOT in Figure 5.3b show that the majority of the colocations have AOT values between 0 and 2. Finally, the distribution of these differences as a function of the GOME-2 LER values used for the retrievals for cases over land show that the retrievals tend to have a lower difference as the LER value increases — this could be a consequence of the fact that so few retrievals converge in high LER regimes that, unless the aerosol layer has a significant contribution to the measured top of atmosphere radiance in comparison to the surface, the retrievals tend to fail.

Retrieved ALH over land (if successful) can be closer to the surface than where the aerosol layer actually is situated vertically. The TROPOMI ALH product, unlike the CALIOP ALH_{ext} which only considers aerosol signatures in the recorded backscatter profile, is also influenced by the presence of undetected clouds. These are some of the several possible

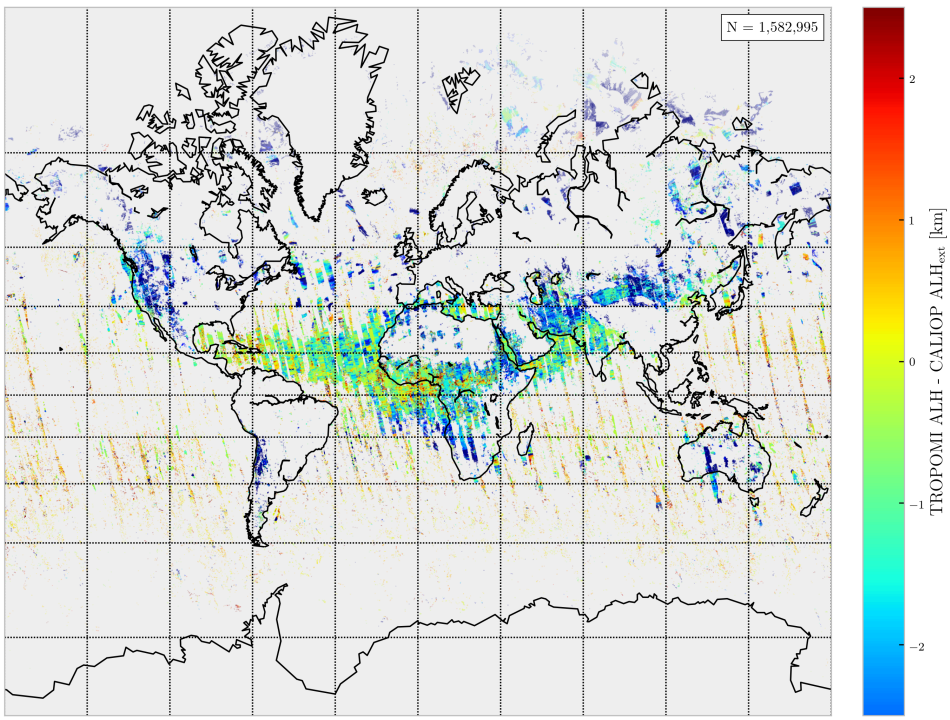

Figure 5.4: A map of cloud filtered and sun glint filtered differences between colocated TROPOMI ALH and CALIOP ALH_{ext} considered for Figure 5.2b.

sources of departures between the observations of CALIOP and TROPOMI over the same scene. In the next section, the comparison between TROPOMI ALH and CALIOP ALH_{ext} is extended for a few selected scenes.

5.3.2 Analysis of selected cases

Selected cases

The analysis presented in the previous section alone is insufficient to fully quantify the quality of the retrieved TROPOMI ALHs, due to the manner in which clouds are handled by both aerosol heights; TROPOMI pixels are affected by the presence of undetected clouds whereas CALIOP aerosol extinction profiles do not consider clouds. Another significant source of departure between TROPOMI and CALIOP is their differing sensing principles. Making conclusions on the quality of the current TROPOMI ALH product requires case-by-case studies of selected scenes. In line with this, four cases are selected to represent a very good mix of scenes containing elevated aerosol layers as well as aerosol layers close to the surface, high and low UV absorbing index, clear and cloudy scenes, clouds over and below aerosol layers, multiple aerosol layers, and retrievals over land and the ocean.

The cases selected are Saharan desert dust and biomass burning events, three off the west coast of Sahara (desert dust) in June 2018 and one off the South Saharan coast (biomass burning) in December 2018. All four cases have very good colocations between TROPOMI and CALIOP, with the CALIOP ground track over the aerosol plumes (plotted with a yellow line over the VIIRS images in Figure 5.5 (1^{st} column). The operational ALH level-2 algorithm operates on pixels falling within the sun-glint regime, however they are excluded from the analyses presented in this chapter. The retrieved UV absorbing index (UVAI) from the operational level-2 UVAI product gives an idea about the shape of the aerosol plumes in all these cases (Figure 5.5 (2^{nd} column)). The UVAI is influenced by many factors including the height of the aerosol layer, with lower UVAI values for aerosol layers closer to the surface. Cases a and b contain several pixels with UVAI values greater than 3.0, whereas a majority of the TROPOMI pixels in cases c and d have TROPOMI UVAI values between 0.0 and 2.0. A significant majority of successful the retrievals in these selected scenes are over a dark surface, owing to the bright surface albedo of the Saharan desert. The reader is pointed to Griffin et al. [3] for comparison of the TROPOMI ALH retrievals over land for biomass burning aerosol plumes with the same from several other instruments including CALIOP.

It is important to note that spaceborne lidars, while having the advantage of being able to map more than one vertical layer in the atmosphere, suffer from attenuation of the signal in the presence of strongly backscattering species such as clouds or aerosols with a large optical depth. In the presence of a primary strongly backscattering aerosol layer, the attenuation of the signal may lead to undetected secondary aerosol layers beneath the primary layer. These layers, not apparent in the CALIOP curtain plots of the measured attenuated backscatter profiles, may be detected by the level 2 aerosol extinction profile product from the CALIOP mission, using the formula described in Equation 5.2. Some of these discussed situations are observed in the CALIOP curtain plots of the selected cases in Figure 5.6, especially for cases a and b, where the attenuated signal does not detect possibly lower aerosol or cloud layers, and in case d where the attenuation of the signal due to a thick aerosol plume can hide the surface from the received backscatter signal. TROPOMI, on the other hand, will tend to report an ALH between these two layers as it

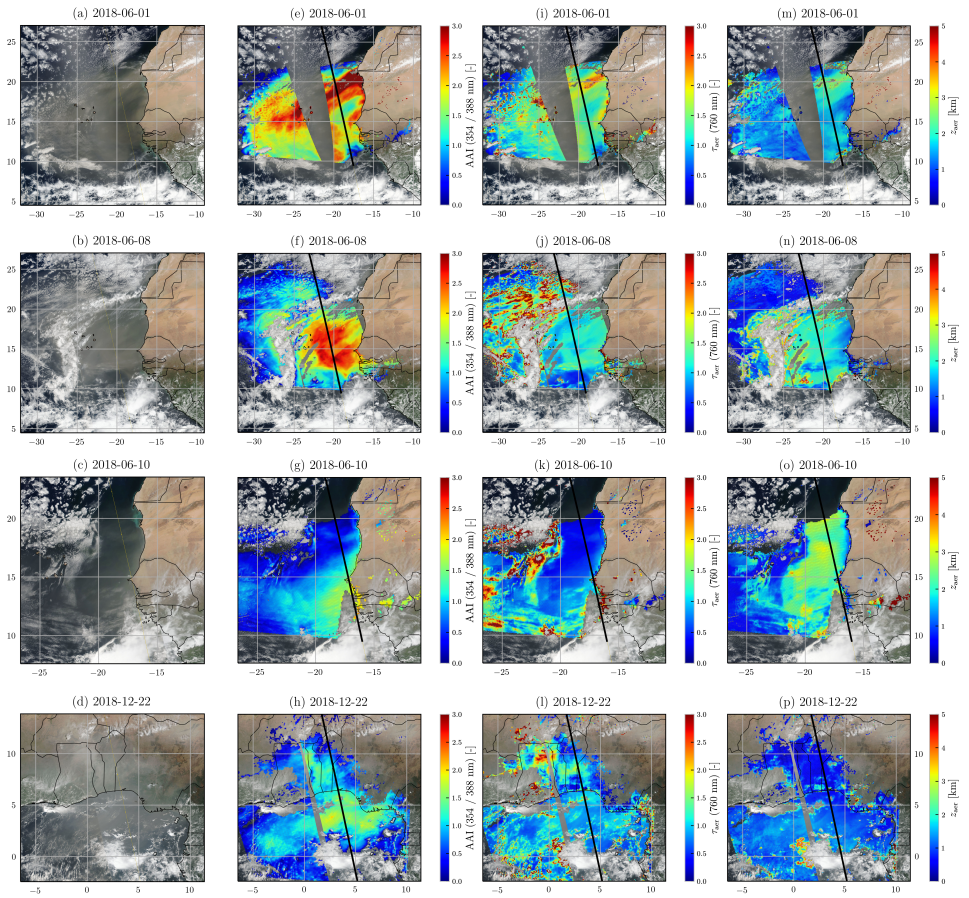

Figure 5.5: **1st column:** Corrected reflectance for the four selected cases as measured by the Suomi NPP/VIIRS imager. The yellow line represents the CALIOP ground track. **2nd column:** The TROPOMI level-2 UV Absorbing Index product. The black line passing through the TROPOMI level-2 retrievals on this plot represents the ground track of the CALIPSO mission. **3rd column:** Retrieved aerosol optical thickness from TROPOMI. **4th column:** Operational TROPOMI ALH.

will be influenced by photons scattered back from both layers.

Analysis

The retrieved TROPOMI ALH in Figure 5.5 (4^{th} column) represent successful retrievals for each of the selected cases. Beyond the sun glint warning, the cloud_warning flag in Table 5.1 is applied to remove possibly cloud contaminated data. The retrieved aerosol optical thickness (AOT), which is a part of the state vector, for each of the scenes are plotted over the VIIRS image of the scene in Figure 5.5 (3^{rd} column). The retrieved AOT (τ_{aer}) can act as a diagnostic tool to indicate the influence of the surface (over bright surfaces) or the presence of undetected clouds (both over bright and dark surfaces) — in these cases, the retrieved AOT of the scene can be uncharacteristically high with values much greater than 3.0. All retrieved TROPOMI AOT values beyond 5.0 are discarded as the neural network forward models are trained with AOT values less than or equal to 5.0.

A visual inspection of the figures in Figure 5.5 shows that the retrieved UVAI, AOT and ALH need not be spatially correlated, as they are separate properties of the observed aerosol plumes — for instance, if the retrieved UVAI and AOT are low (case c), the retrieved ALH need not necessarily be low. An inspection of the plots of the retrieved AOT for cases c (between latitudes 10° and 15° and longitude -20°) and d reveal square structures, both over the ocean and land. These square shaped spatial artefacts are the surface albedo grids derived from the database provided by Tilstra et al. [13], which is the current source for surface reflectance in the ALH retrieval algorithm. In cases such as case c, the retrieved AOT contains surface information influenced by the assumed albedo in the database. These spatial features are not as apparent in cases a and b (Figure 5.5, 1^{st} and 2^{nd} rows) as a majority of the signal in the measured top of atmosphere radiances come from aerosols and the minority from the surface. Another major observation is the lack of retrievals over the desert. This is within expectation, as measurements of the top of atmosphere radiances over a cloud-free desert scene tend to contain more photons scattered back from the surface than the aerosol layer. As a result, retrievals over bright scenes are sensitive to the assumed errors in the surface albedo, thereby reducing sensitivity to the assumed ALH (Sanders et al. [12], Section 2, Figure 2).

While scenes not contaminated with clouds show a smooth spatial distribution of the retrieved ALH, the presence of clouds may or may not add spatial variability in the ALH product. For instance, the the presence of low clouds are clear in case b (Figure 5.5b) beyond latitude 21.0°, but the retrieved ALH is spatially homogeneous with values less than 1.0 km. For each of the selected cases, colocated CALIOP profiles in Figure 5.6 give additional information about the scene. The CALIOP curtain plot for case b reveals the influence of low clouds as well as high clouds on the cloud-screened ALH. An example of cloud-contaminated heterogeneous vertical distribution of TROPOMI ALH in Figure 5.6a can be observed between latitudes 9.5° and 11.0°. The cloud filtering following the cloud_warning flag in Table 5.1 does not detect these low clouds (for instance above latitude 21.50°, see Figure 5.6 a, b). These are manually for comparison further on.

From Figure 5.2b, TROPOMI retrievals of ALH over bright surfaces are expected to differ from CALIOP ALH_{ext}, wherein the TROPOMI ALH product may report ALH estimates closer to the surface than CALIOP will. This is observed in case d (Figure 5.5, bottom row), wherein the CALIOP curtain plot for (Figure 5.6d) indicates that the plume is close to

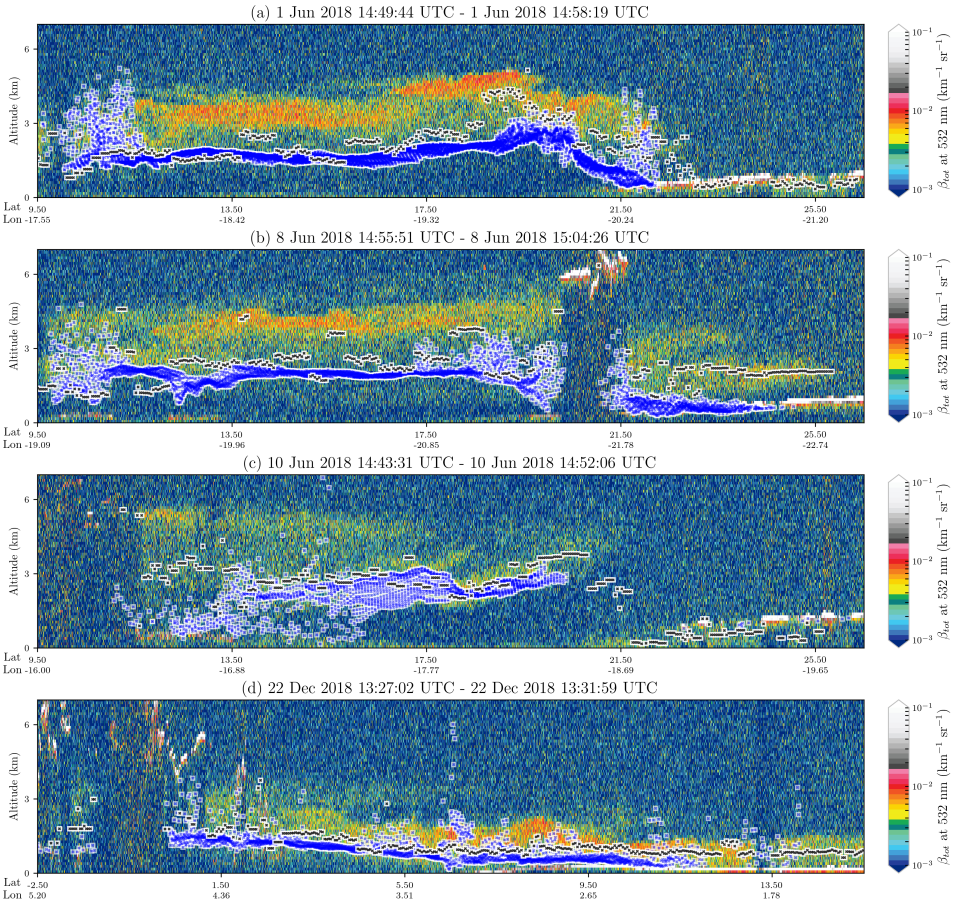

Figure 5.6: CALIOP level-1 backscatter curtain plots for measurements in the 532 nm channel for the four selected cases in Figure 5.5. The blue markers (crosses over a white box) represent co-located TROPOMI ALH retrievals within 100 km of each CALIOP profile present in this plot. The black markers (crosses over a white box) represent the CALIOP weight aerosol heights as computed using Equation 5.2. TROPOMI data that are either in sun-glint region or cloud contaminated are removed (cloud detection is done using the cloud_warning flag from Table 5.1).

the surface, with a maximum height less than 3 km; TROPOMI ALH for biomass burning aerosol plume that extends from land to the ocean is slightly closer to the surface in the case of land when compared to CALIOP ALH_{ext}, whereas over the ocean both height estimates more or less are in agreement.

For cases a and b, retrieved TROPOMI ALH does not seem to coincide with large values of the received backscatter signal in the level-1 data, whereas it does for case c, and to a certain extent for case d (over land it tends to be closer to the surface). Parts of the CALIOP curtain plots for cases a, b and c suggest that a possible second layer beneath the layer that is visually obvious, or that the desert dust layer extends deeper to the surface and the CALIOP signal is simply too attenuated to detect it.

A direct comparison of the CALIOP ALH_{ext} and TROPOMI ALH for these four selected cases are presented in Figure 5.7. For this comparison, every cloud-filtered and sun-glint-filtered TROPOMI pixel with ALH information colocated to a specific CALIOP level-2 aerosol extinction profile in Figure 5.6 is averaged and a standard deviation is also computed. These averaged TROPOMI ALH are then compared to the CALIOP ALH_{ext}, and show that TROPOMI ALH differ from CALIOP ALH_{ext} by 0.53 km, with a pearson correlation coefficient of 0.64 and a slope of 1.0; CALIOP ALH_{ext} are systematically higher than TROPOMI ALH (indicated by a y-intercept of the fit at 0.53 km). The CALIOP ALH_{ext} is also higher than TROPOMI ALH almost consistently in most cases. This could possibly be due to CALIOP possibly underestimating the aerosol layer thickness due to strong attenuation of the lidar signal at the top of the aerosol layer Rajapakshe et al. [9], whereas TROPOMI ALH product does not suffer from such attenuation.

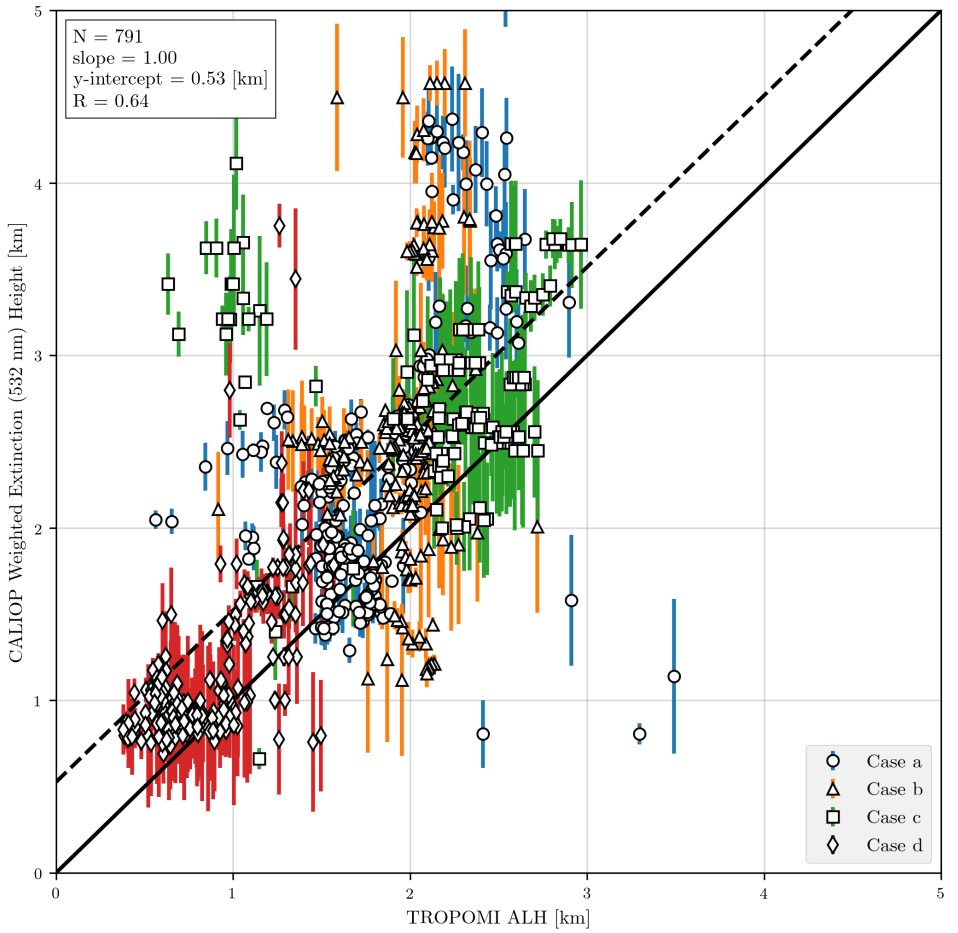

Figure 5.7: Comparison between the CALIOP weighted extinction heights (y-axis) calculated using Equation 5.2 and plotted in Figure 5.6, against averaged TROPOMI ALH (x-axis). The blue lines represent the standard deviation of the TROPOMI heights in the averaging pool, and the markers represent the mean TROPOMI ALH for each CALIOP ALH_{ext}. The dashed black line marks the fit between CALIOP ALH_{ext} and TROPOMI ALH. The solid black line is a neutral line between the x and the y axes. The legend in the bottom right corner describes the different markers used for the different cases.

5.4 Discussion and conclusion

This chapter discusses the quality of the soon to be released TROPOMI ALH product by comparing it with CALIOP data of colocated measurements of scenes containing aerosols between the two instruments. In order to do so, CALIOP weighted extinction heights from the 532 nm channel were calculated following Equation 5.2, and then directly compared to TROPOMI ALH. Further on, four individual cases of Saharan desert dust and biomass burning aerosol events in 2018 were selected for a deeper analysis of the product's quality.

From the analysis presented in this chapter, TROPOMI's neural network ALH retrieval algorithm retrieves ALH values that compare well with CALIOP weighted extinction heights in cloud-screened cases following the cloud screening strategy using the TROPOMI ALH level-2 processing quality flags discussed in Table 5.1. For more than 1 million colocations between CALIOP and TROPOMI over the ocean, the TROPOMI ALH differs from CALIOP ALH_{ext} on average by approximately -1 km and -0.76 km median, with the TROPOMI ALH values being lower than the CALIOP ALH_{ext}. Over land, the same values are -2.41 km on average and -1.75 km as the median. To get a better understanding of the differences between TROPOMI and CALIOP retrieved aerosol heights, this chapter compared the ALH for selected cases among the more 1 million colocations that were better understood. The four selected scenes were chosen around the West Saharan region, where a majority of the TROPOMI-CALIOP colocations were found. For the selected cases, largely over the ocean within a portion of the data over land, the averaged retrieved ALH from TROPOMI differed from CALIOP ALH_{ext} by 0.53 km, with CALIOP ALH_{ext} being higher than TROPOMI ALH. These numbers are indicative that TROPOMI ALH performs well, especially considering the many simplifications made by the retrieval algorithm in order to optimise on the computational speed; future improvements to the forward model may only improve the product further on.

There is a clear distinction between TROPOMI ALH retrievals over land and the ocean as photons scattering back from bright surfaces tend to influence ALH estimates closer towards the surface than an elevated aerosol layer. Retrieved ALH over land, if successful, can to be closer to the surface if measured signal in the top of atmosphere contains more photons scattered back from the deepest atmospheric layer which is the surface, in comparison to elevated aerosol layers which are higher up in the atmosphere. This, however can change depending on the amount of aerosol information available in the spectrum compared to same from the surface. Any attempt in retrieving ALH over the desert generally fail, with very few exceptions. There are several challenges, that will need further development.

The TROPOMI level-2 UVAI product is currently an ingredient in selecting pixels containing aerosols for retrieving ALH. While this choice works quite well for cloud free scenarios, it does not do a great job when a scene that contains both aerosols and clouds. These cloudy scenes seem to not be detected by the current cloud filtering schematic in the level-2 algorithm, and will require a significant update in deciding whether a pixel is cloudy or not. For cases scenes with a low aerosol load, square shaped artefacts resulting from a surface albedo database with a resolution significantly lower than TROPOMI exist. Currently, the GOME-2 surface LER product derived from Tilstra et al. [13] is used operationally, and will eventually need to be updated with a higher resolution version possibly derived from TROPOMI itself. To that extent, owing to the boost in the computational speed

of the radiative transfer calculations, the algorithm can now incorporate more complex aerosol property and profile parameterizations. Such a step will benefit the TROPOMI ALH retrieval accuracy significantly.

Finally, space based lidars such as the CALIOP instrument on board the CALIPSO mission are a very good source of aerosol vertical information to validate the TROPOMI ALH product. While the CALIOP level-1 backscatter profiles may be attenuated in cases of very strong signals from the top of the aerosol layer, the weighted extinction heights in conjunction with the backscatter profiles are sufficient for validation activities. These CALIOP profiles will be very important in assessing the impact of future development activities of the TROPOMI ALH product.

References

[1] de Haan, J. F., Bosma, P. B., and Hovenier, J. W. (1987). The adding method for multiple scattering calculations of polarized light. *Astronomy and Astrophysics*, 183.

[2] Dubovik, O., Holben, B., Eck, T. F., Smirnov, A., Kaufman, Y. J., King, M. D., Tanré, D., and Slutsker, I. (2002). Variability of Absorption and Optical Properties of Key Aerosol Types Observed in Worldwide Locations. *Journal of the Atmospheric Sciences*, 59(3):590–608.

[3] Griffin, D., Sioris, C., Chen, J., Dickson, N., Kovachik, A., Graaf, M. d., Nanda, S., Veefkind, P., Dammers, E., McLinden, C. A., Makar, P., and Akingunola, A. (2019). The 2018 fire season in North America as seen by TROPOMI: aerosol layer height validation and evaluation of model-derived plume heights. *Atmospheric Measurement Techniques Discussions*, pages 1–30.

[4] Henyey, L. C. and Greenstein, J. L. (1941). Diffuse radiation in the Galaxy. *The Astrophysical Journal*, 93:70.

[5] Koffi, B., Schulz, M., Bréon, F.-M., Griesfeller, J., Winker, D., Balkanski, Y., Bauer, S., Berntsen, T., Chin, M., Collins, W. D., Dentener, F., Diehl, T., Easter, R., Ghan, S., Ginoux, P., Gong, S., Horowitz, L. W., Iversen, T., Kirkevåg, A., Koch, D., Krol, M., Myhre, G., Stier, P., and Takemura, T. (2012). Application of the CALIOP layer product to evaluate the vertical distribution of aerosols estimated by global models: AeroCom phase I results. *Journal of Geophysical Research: Atmospheres*, 117(D10).

[6] Nanda, S., de Graaf, M., Sneep, M., de Haan, J. F., Stammes, P., Sanders, A. F. J., Tuinder, O., Veefkind, J. P., and Levelt, P. F. (2018a). Error sources in the retrieval of aerosol information over bright surfaces from satellite measurements in the oxygen A band. *Atmos. Meas. Tech.*, 11(1):161–175.

[7] Nanda, S., Graaf, M. d., Veefkind, J. P., Linden, M. t., Sneep, M., Haan, J. d., and Levelt, P. F. (2019). A neural network radiative transfer model approach applied to TROPOMI's aerosol height algorithm. *Atmospheric Measurement Techniques Discussions*, pages 1–24.

[8] Nanda, S., Veefkind, J. P., de Graaf, M., Sneep, M., Stammes, P., de Haan, J. F., Sanders, A. F. J., Apituley, A., Tuinder, O., and Levelt, P. F. (2018b). A weighted least squares approach

to retrieve aerosol layer height over bright surfaces applied to GOME-2 measurements of the oxygen A band for forest fire cases over Europe. *Atmos. Meas. Tech.*, 11(6):3263–3280.

[9] Rajapakshe, C., Zhang, Z., Yorks, J. E., Yu, H., Tan, Q., Meyer, K., Platnick, S., and Winker, D. M. (2017). Seasonally transported aerosol layers over southeast Atlantic are closer to underlying clouds than previously reported. *Geophysical Research Letters*, 44(11):5818–5825.

[10] Rodgers, C. D. (2000). *Inverse methods for atmospheric sounding: theory and practice*, volume 2. World Scientific.

[11] Sanders, A. F. J. and de Haan, J. F. (2016). TROPOMI ATBD of the Aerosol Layer Height product.

[12] Sanders, A. F. J., de Haan, J. F., Sneep, M., Apituley, A., Stammes, P., Vieitez, M. O., Tilstra, L. G., Tuinder, O. N. E., Koning, C. E., and Veefkind, J. P. (2015). Evaluation of the operational Aerosol Layer Height retrieval algorithm for Sentinel-5 Precursor: application to Oxygen A band observations from GOME-2A. *Atmospheric Measurement Techniques*, 8(11):4947–4977.

[13] Tilstra, L. G., Tuinder, O. N. E., Wang, P., and Stammes, P. (2017). Surface reflectivity climatologies from UV to NIR determined from Earth observations by GOME-2 and SCIAMACHY: GOME-2 and SCIAMACHY surface reflectivity climatologies. *Journal of Geophysical Research: Atmospheres*.

[14] Vasilkov, A., Joiner, J., and Spurr, R. (2013). Note on rotational-Raman scattering in the O_2 A- and B-bands. *Atmospheric Measurement Techniques*, 6(4):981–990.

[15] Wagner, T., Beirle, S., Deutschmann, T., and Penning de Vries, M. (2010). A sensitivity analysis of Ring effect to aerosol properties and comparison to satellite observations. *Atmospheric Measurement Techniques*, 3(6):1723–1751.

[16] Wang, P., Stammes, P., van der A, R., Pinardi, G., and van Roozendael, M. (2008). FRESCO+: an improved O2 A-band cloud retrieval algorithm for tropospheric trace gas retrievals. *Atmos. Chem. Phys.*, 8(21):6565–6576.

[17] Winker, D. M., Vaughan, M. A., Omar, A., Hu, Y., Powell, K. A., Liu, Z., Hunt, W. H., and Young, S. A. (2009). Overview of the CALIPSO Mission and CALIOP Data Processing Algorithms. *Journal of Atmospheric and Oceanic Technology*, 26(11):2310–2323.

6

Conclusions and outlook

This dissertation presents the algorithmic improvements implemented in the KNMI aerosol layer height retrieval algorithm, which now allow it to be operationally feasible for the current Sentinel-5 Precursor satellite mission and future Sentinel-4 and Sentinel-5 missions. The suggested improvements are focused on the identified challenges for retrieving aerosol layer height from measurements of the top of atmosphere reflectance in the oxygen A-band using satellite sensors, namely

- The retrieval of aerosols over land is challenging, as the aerosols generally have a significantly lower contribution to the top of atmosphere reflectance in the oxygen A-band in comparison to the land, and
- Due to the density of oxygen absorption lines in the A-band, computing the top of atmosphere reflectance in the A-band requires calculations for many wavelengths, which slows down the retrieval of aerosol properties if done using line-by-line radiative transfer models.

The options presented in this study were tested with both synthetic (Sentinel-5 Precursor and Sentinel 4) and real (GOME-2 and Sentinel-5 Precursor) satellite data. The key findings and take-home messages from this study are summarised in the following section.

6.1 Summary

Photons scattering from bright surfaces reduce the available information on aerosols in the top of atmosphere reflectance measured by satellite instruments; this one of the primary causes of errors in retrieved aerosol properties from oxygen A-band measurements over land. There is an anti-correlative behavior between the surface and aerosol contributions in the top of atmosphere reflectance in the oxygen A-band. Over optically dark surfaces such as the ocean, aerosols are relatively bright, and therefore dominate the top-of-atmosphere signal for cloud free scenes. As the surface gets brighter, the relative contribution of the aerosols decreases. For bright surfaces, such as

deserts, the surface contribution dominates the signal. There are several implications of this phenomenon:

- With an increase in surface contribution to the top of atmosphere reflectance, the gradient of the cost function becomes increasingly shallow. The reduction in cost function 'steepness' can be seen in cases when the viewing angle is zero (nadir viewing), since the surface contribution will be larger as the photon path length is the smallest (less scattering of photons in this geometry).
- With increasing viewing zenith angle and increasing aerosol optical thickness over bright surfaces, sensitivity studies show the presence of multiple minima in the cost function. This is not present over darker surfaces such as the ocean.
- As the surface contribution increases, parts of the oxygen A-band that contain a significant portion of the aerosol vertical information start to lose sensitivity to aerosol layer height. This results in larger uncertainties in the retrieved aerosol vertical information.
- The increase in surface contribution increases the sensitivity of the model to errors in the assumed model parameters. Variables which did not affect the retrieved aerosol layer height over darker scenes now cause larger errors over optically bright surfaces. Errors in the assumed surface albedo are more apparent in the retrieved product. In general, for high surface albedo, the retrieved aerosol layer height is biased closer to the surface, if the retrieval converges at all.

Although not explicitly mentioned in Chapter 2 of this dissertation, the consequence of an incorrectly assumed surface albedo can be observed even over dark surfaces such as the ocean. For instance in Chapter 5 Figure 5.5, square shaped artefacts with pixel sizes the same as the surface albedo database used in the radiative transfer calculations can be observed over the ocean for areas with little aerosols. These surface albedo database artefacts disappear as the aerosol contributions in the scene increase, which is one way to highlight the fact that the surface contributions are relevant when the aerosol contributions are low.

The errors due to surface contributions can be reduced to a certain extent by scaling the signal to noise ratio of the measured signal in the retrieval process. This is done by exploiting the mechanism of the measurement error covariance matrix, which ranks spectral points with the highest signal to noise ratio (SNR) higher than the ones with lower signal to noise ratios. In the oxygen A-band, parts of the spectrum that have a lower oxygen absorption cross section have more surface contribution: which is low as the albedo is low, and high when the surface brightness increases. However, the measurements with a high surface albedo contribution, are also the parts of the oxygen A-band spectrum with lesser information on aerosol layer height. To retrieve aerosol layer height over bright surfaces, the SNR is scaled dynamically using the derivatives of the top of atmospheric reflectance spectra with respect to aerosol optical thickness, aerosol layer height and the surface albedo. This scaling changes with different aerosol optical thickness and surface brightness, and assigns a higher noise value to parts of the spectrum with photons that are

less absorbed by the oxygen molecule. This scaling of the SNR results in an improvement in the retrieved aerosol product, with a significant improvement in the biases in the retrieved aerosol layer height over bright surfaces in comparison to the original non-scaling approach. In 2000 synthetic case studies, the dynamic scaling method showed an increase in converged retrievals from 89% to 92%, and a reduction in biases for 86% of the cases. The method applied to real retrievals also shows an increase in the number of convergences in comparison to the original method.

Neural networks learn and replicate the line-by-line radiative transfer calculations of the top of atmosphere reflectance as well as its derivatives with respect to aerosol optical thickness and aerosol layer height within acceptable error margins, and improve computational speeds by more than three orders of magnitude. Neural networks are known to be universal function approximators, which is an excellent use case for replacing line-by-line calculations in the operational processors of satellite missions. In this case, neural networks trained on 500,000 spectra generated by line-by-line radiative transfer calculations were shown to retrieve aerosol layer heights well within 50 m (or, 50 hPa) compared to retrievals with the line-by-line radiative transfer model on the same spectra, both using an optimal estimation setup. This ensures that the retrieved product has error estimates that can be used by assimilation models. The neural network model improves feasibility of the aerosol layer height retrieval algorithm in an operational environment, which previously was hindered by the slow nature of line-by-line calculations. Applied to real retrievals, the neural network radiative transfer model compared well with the line-by-line counterpart, with average differences below 40 m and a standard deviation of approximately 150 m. The retrievals from both methods were the most different for low AAI values (less than 2.0) with large differences up to 500 meters, reducing significantly as the AAI increased.

The neural network model was later incorporated into the Sentinel-5 Precursor's operational level-2 processor, and now processes a significant amount of data on a daily basis. The study presented in Chapters 4 and 5 have shown that trained neural networks can be used as a good proxy for a full physics radiative transfer model such as DISAMAR. The TROPOMI retrieved aerosol layer heights compared with aerosol extinction heights derived from the CALIOP instrument for selected cases using 800 colocations do show good agreement: a difference of 530 m on average, signalling that the TROPOMI level-2 operational processor is performing well on aerosol retrieval within the limitations of the measurement technique. But at the same time there are several challenges that these colocation studies have also identified. For instance, for more than 1.5 million colocations between CALIOP and TROPOMI, the TROPOMI aerosol layer height product is, in general, lower than the aerosol extinction heights from CALIOP — this could very well be due to the differing sensing principles of CALIOP and TROPOMI. The two instruments also using different wavelengths of light, which has different sensitivities to aerosols. The differences were on average approximately 1 km (0.7 km median) for pixels over the ocean, and more than 2 km (1.75 km median) for pixels over land, clearly indicating that retrieval sensitivities over land and ocean differ. The processor currently does not include the proposed dynamic scaling method. When it is introduced in the operational processor in the future, it will help in reducing the error caused by surface contributions significantly.

6.2 Outlook

The operational aerosol layer height algorithm developed in the period of this dissertation has the potential for further improvements. The various avenues of improvement are highlighted as follows.

Retrieving aerosol information over land from the oxygen B-band. Retrieving aerosol properties over land from the oxygen A-band is challenging because of its position beyond the red edge. Land is significantly brighter in this wavelength range as the amount of photosynthetically active radiation reduces drastically from 700 nm and up (red edge), and vegetation becomes increasingly brighter. In wavelengths beyond this edge, retrievals with acceptable accuracy are only possible when there is sufficient aerosol information in the top of atmosphere reflectance spectra. An alternative, or a complimentary, is the oxygen B-band which lies before the red edge.

In the B-band, land appears dark: almost as dark as the ocean (except for deserts and snow/ice). Although the absorption lines are not as deep as the A-band, there is sufficient aerosol vertical information for retrieval algorithms [3]. Work by Xu et al. [4] has shown this to be feasible. Combining the two seems to be the way forward, as Chen et al. [1] suggest. They have retrieved aerosol heights using both A and B bands together, and report a significant improvement over retrieved aerosol heights using the oxygen A-band alone. This can be operationalised into the TROPOMI level-2 processor to replace the existing oxygen A-band aerosol layer height retrieval algorithm. This, however, is only limited to TROPOMI thus far, and will need more work to improve retrieval results for Sentinel-4.

Incorporating more parameters into the forward model. Having established that neural networks can be trained to learn the calculations of a radiative transfer model, there are more avenues of research to determine the extent of its capabilities. The goal of the neural network study in this dissertation was to replicate a forward model that was limited by operational constraints of computational time — several parameters in the model were simplified or assumed in order to reduce the number of calculations. Now, the DISAMAR forward model could potentially be expanded to include more complex model parameters such as a the Mie aerosol scattering model or a surface reflectance model. The calculation times required by DISAMAR are irrelevant, as it is the neural network model that will be running the calculations operationally and not the forward model.

Moving from a simplistic aerosol profile to a one that is more representative of reality. One of the model parameters that will eventually need an update is the aerosol vertical representation. The current aerosol model is unrealistic — aerosols are not always 50 hPa thick, or are uniformly distributed into a single layer. Expanding DISAMAR to include an aerosol vertical profile will one day be necessary to retrieve aerosol profiles from oxygen absorption bands. This may involve more calculations by DISAMAR, which can slow down the retrieval algorithm even more. Here, neural network implementation presented in this thesis can help learn the new and improved radiative transfer model with aerosol profiles.

Cloud filtering using machine learning techniques Clouds are the most important disturbance for aerosol information retrieval as well as the aerosol layer height algorithm

described in this dissertation or any other aerosol retrieval algorithm. The most commonly used strategy is to use data from multiple sensors in order to remove cloudy pixels, and only apply the aerosol retrieval algorithm on cloud-free pixels. In the case of solar backscatter instrumentation like TROPOMI this can lead to false positive classifications, and result in removing pixels with very thick aerosol plumes. Here, machine learning algorithms can play an important role in cloud-screening. There are two ways to do this — train learning algorithms that either identify if a pixel contains clouds (using input data of cloudy scenes), or train models that identify whether the pixel contains cloud-free scenes (using input data of cloud-free scenes). In the former, we filter out detected pixels and in the latter we only process detected pixels. Research on this topic will lead to a more reliable level-2 aerosol layer height product from Earth Observation missions.

Exploiting multiple viewing geometries from the hourly Sentinel-4 observations. The Sentinel-4 mission is geostationary, which allows multiple measurements of a single scene over the course of a day. In the case of Sentinel-4, an hourly granularity in the measured signal can be expected. One of the disadvantages is the changing solar-satellite geometry, which will need a surface reflectance model (such as a bidirectional reflectance distribution function) that calculates surface reflectance as a function of the geometries. Multiple geometries can provide multiple observations of the same scene, provided the aerosols in the scene are spatio-temporally stable. These multiple observations may be used to infer more aerosol properties and/or improve the accuracy as compared to a single measurement. Such methods already have a heritage in existing satellite missions such as MISR [2], which could be a starting point for Sentinel-4.

References

[1] Chen, X., Jun, W., Xu, X., Zhou, M., Zhang, H., Lorena, C. G., Peter, R. C., Scott, J. J., John, Y., Matthew, M., Jeffrey, S. R., Martin, d. G., and Shobha, K. (2021). First retrieval of absorbing aerosol height over dark target using TROPOMI Oxygen B band: algorithm development and application for surface particulate matter estimates. *Remote Sensing of Environment*, submitted(under review).

[2] Griffin, D., Sioris, C., Chen, J., Dickson, N., Kovachik, A., Graaf, M. d., Nanda, S., Veefkind, P., Dammers, E., McLinden, C. A., Makar, P., and Akingunola, A. (2019). The 2018 fire season in North America as seen by TROPOMI: aerosol layer height validation and evaluation of model-derived plume heights. *Atmospheric Measurement Techniques Discussions*, pages 1–30.

[3] Sanghavi, S., Martonchik, J. V., Landgraf, J., and Platt, U. (2012). Retrieval of the optical depth and vertical distribution of particulate scatterers in the atmosphere using O_2 A- and B-band SCIAMACHY observations over Kanpur: a case study. *Atmospheric Measurement Techniques*, 5(5):1099–1119.

[4] Xu, X., Wang, J., Wang, Y., Zeng, J., Torres, O., Reid, J. S., Miller, S. D., Martins, J. V., and Remer, L. A. (2019). Detecting layer height of smoke aerosols over vegetated land and water surfaces via oxygen absorption bands: hourly results from EPIC/DSCOVR in deep space. *Atmospheric Measurement Techniques*, 12(6):3269–3288.

Curriculum Vitæ

Swadhin Nanda

16-03-1992 Born in Doranda, Ranchi, India.

Education

2013 B.Tech Civil Engineering
KIIT University,
Bhubaneswar, Odisha, India

2015 M.Sc. Applied Earth Sciences
Civil Engineering and Geosciences, Delft University of Technology,
Delft, The Netherlands

2020 PhD. Atmospheric Remote Sensing
Civil Engineering and Geosciences, Delft University of Technology,
Delft, The Netherlands *Thesis:*
Promotor: Prof. dr. P. F. Levelt

List of Publications

1. **Nanda, S.**, de Graaf, M., Veefkind, J. P., Sneep, M., ter Linden, M., Sun, J., and Levelt, P. F.: A first comparison of TROPOMI aerosol layer height (ALH) to CALIOP data, Atmos. Meas. Tech., 13, 3043–3059, https://doi.org/10.5194/amt-13-3043-2020, 2020.

2. Griffin, D., Sioris, C., Chen, J., Dickson, N., Kovachik, A., de Graaf, M., **Nanda, S.**, Veefkind, P., Dammers, E., McLinden, C. A., Makar, P., and Akingunola, A.: The 2018 fire season in North America as seen by TROPOMI: aerosol layer height intercomparisons and evaluation of model-derived plume heights, Atmos. Meas. Tech., 13, 1427–1445, https://doi.org/10.5194/amt-13-1427-2020, 2020.

3. **Nanda, S.**, de Graaf, M., Veefkind, J. P., ter Linden, M., Sneep, M., de Haan, J., and Levelt, P. F.: A neural network radiative transfer model approach applied to the Tropospheric Monitoring Instrument aerosol height algorithm, Atmos. Meas. Tech., 12, 6619–6634, https://doi.org/10.5194/amt-12-6619-2019, 2019.

4. Sun, J., Veefkind, P., **Nanda, S.**, van Velthoven, P., and Levelt, P.: The role of aerosol layer height in quantifying aerosol absorption from ultraviolet satellite observations, Atmos. Meas. Tech., 12, 6319–6340, https://doi.org/10.5194/amt-12-6319-2019, 2019.

5. **Nanda, S.**, Veefkind, J. P., de Graaf, M., Sneep, M., Stammes, P., de Haan, J. F., Sanders, A. F. J., Apituley, A., Tuinder, O., and Levelt, P. F.: A weighted least squares approach to retrieve aerosol layer height over bright surfaces applied to GOME-2 measurements of the oxygen A band for forest fire cases over Europe, Atmos. Meas. Tech., 11, 3263–3280, https://doi.org/10.5194/amt-11-3263-2018, 2018.

6. **Nanda, S.**, de Graaf, M., Sneep, M., de Haan, J. F., Stammes, P., Sanders, A. F. J., Tuinder, O., Veefkind, J. P., and Levelt, P. F.: Error sources in the retrieval of aerosol information over bright surfaces from satellite measurements in the oxygen A band, Atmos. Meas. Tech., 11, 161–175, https://doi.org/10.5194/amt-11-161-2018, 2018.